

Dissertation

**submitted to the
Combined Faculties of the Natural Sciences and Mathematics
of the Ruperto-Carola-University of Heidelberg, Germany
for the degree of
Doctor of Natural Sciences**

**Put forward by
Dipl.-Phys. Philipp Nils Raith
born in: Heilbronn**

Oral examination: 06.11.2012

**Few-Cycle Multidimensional
Laser Control of Attosecond Pulse Generation**

**Referees: Dr. Thomas Pfeifer
Prof. Dr. Selim Jochim**

Multidimensionale Laserkontrolle der Erzeugung von Attosekundenpulsen—In dieser Arbeit wird die kohärente Kontrolle von Attosekundenpulsen und -pulszügen durch die Erzeugung Hoher Harmonischer (engl. "high-harmonic generation", HHG) sowohl experimentell als auch numerisch untersucht. Zu diesem Zweck werden intensive Femtosekundenlaserpulse mit einer Dauer von nur wenigen Zyklen und mit stabilisierter Trägerzu-Einhüllenden-Phase (engl. "carrier-envelope phase", CEP) in Argon fokussiert. Nach ersten hier durchgeführten Studien zur Auswirkung dieser CEP für sich allein wird das Kontrollschema durch einen zeitlichen Versatz entweder zwischen zwei variablen Abschnitten des Laserspektrums oder zu einem zusätzlichen Laserfeld mit doppelter Frequenz erweitert. Wir führen das Konzept der gleichzeitigen, unabhängigen Kontrolle mehrerer Eigenschaften der Attosekundenpulse durch eine gleich große Zahl von Steuergrößen ein. Mit diesem multidimensionalen Ansatz lässt sich die HHG effizient, vielseitig und auf einfachen physikalischen Prinzipien basierend kontrollieren. Die experimentelle Realisierung der Kontrollmethode mit einem geteilten Laserspektrum ermöglichte die Steuerung etlicher spektraler Eigenschaften der Hohen Harmonischen. Die Auswirkungen der einzelnen Steuergrößen können ebenso wie die spezifischen Wirkungsmechanismen ermittelt und durch numerische Simulationen bestätigt werden. Zur Beschreibung des Prozesses reicht hierbei die Betrachtung eines einzelnen Atoms aus. Insbesondere wird festgestellt, dass eine Modulation der instantanen Frequenz am Maximum der Laserpulse in einer quantitativ festgelegten Weise die Energie der Harmonischen verändert. Zudem ermöglicht die Interferenz der beiden Teilfelder die Bildung zweier zeitlicher Maxima des Laserfeldes. Die spektrale Interferenz der zwei an diesen Maxima produzierten Attosekundenpulszüge resultiert in Kämmen von gebrochenzahligen Hohen Harmonischen, die in der Zukunft bei der hochaufgelösten spektralen Interferometrie im extremen Ultravioletten angewendet werden können.

Few-Cycle Multidimensional Laser Control of Attosecond Pulse Generation—In this work, the coherent control of attosecond pulse and pulse train production by high-order harmonic generation (HHG) is investigated both experimentally and numerically. For this purpose, intense, few-cycle femtosecond laser pulses with a stable carrier-envelope phase (CEP) are focused into argon. After the examination of pure CEP effects, the controllability of HHG is qualitatively enhanced by the addition of a time delay either between two variable spectral sections or with respect to a second driver field at the doubled frequency. The concept of independent control of several properties of the produced attosecond pulse at once by an equally large number of control variables is introduced as an efficient multidimensional (multi-parameter) scheme to control HHG both comprehensively and based on fundamental physics principles. The experimental realization of the split-spectrum time-delay method leads to control over manifold spectral properties of the produced high harmonics. The effects of the individual control variables are separated and the control mechanisms are uncovered on the single-atom level and confirmed by numerical simulations. In particular, it is found that a time-delay dependent change of the instantaneous frequency at the intensity maximum of the driver pulse causes a quantitatively determined modulation of the harmonic energies. Moreover, the interference of the two subfields enables the creation of two driver intensity maxima. The spectral interference of the two time-delayed attosecond pulse trains, produced at these intensity maxima, results in the controlled generation of fractional high-harmonic combs. These combs can, in future, be applied to high-precision spectral interferometry in the extreme ultraviolet.

List of Publications

Parts of this work have been published in the following references:

P. Raith, C. Ott, and T. Pfeifer.

Attosecond twin-pulse control by generalized kinetic heterodyne mixing.

Opt. Lett. **36**, 283–285 (2011).

P. Raith, C. Ott, C. P. Anderson, A. Kaldun, K. Meyer, M. Laux, Y. Zhang, and T. Pfeifer.
Fractional high-order harmonic combs and energy tuning by attosecond-precision split-spectrum pulse control.

Appl. Phys. Lett. **100**, 121104 (2012).

C. Ott, M. Schönwald, P. Raith, A. Kaldun, M. Krüger, G. Sansone, P. Hommelhoff, Y. Zhang, K. Meyer, and T. Pfeifer.

Two-Dimensional Spectral Interferometry using the Carrier-Envelope Phase.

submitted to Phys. Rev. Lett. (2012).

P. Raith, C. Ott, C. P. Anderson, A. Kaldun, K. Meyer, M. Laux, Y. Zhang, and T. Pfeifer.
Fractional high-harmonic combs by attosecond-precision split-spectrum pulse control.

Eur. Phys. J. Conferences: Ultrafast Phenomena. *accepted* (2012).

P. Raith, C. Ott, C. P. Anderson, A. Kaldun, K. Meyer, M. Laux, Y. Zhang, and T. Pfeifer.
Fractional high-order harmonic combs and energy tuning by split-spectrum field synthesis.

in CLEO: QELS-Fundamental Science, OSA Technical Digest (Optical Society of America, 2012), paper QTu2H.4.

P. Raith, C. Ott, K. Meyer, A. Kaldun, C. P. Anderson, M. Laux, M. Ceci, and T. Pfeifer.
CEP-Control and Spectral Interferometry of Fractional High-harmonic Combs.

in preparation.

P. Raith, C. Ott, A. Kaldun, K. Meyer, M. Laux, and T. Pfeifer.

Interferometrically enhanced sensitivity of carrier-envelope phase control in synthesized laser fields.

in preparation.

Further publications with author contributions:

C. Ott, P. Raith, and T. Pfeifer.

Sub-cycle strong-field interferometry.

Opt. Express **18** 24307–24315 (2010).

M. C. Kohler, C. Ott, P. Raith, R. Heck, I. Schlegel, C. H. Keitel, and T. Pfeifer.

High Harmonic Generation Via Continuum Wave-Packet Interference.

Phys. Rev. Lett. **105**, 203902 (2010).

K. Meyer, C. Ott, P. Raith, A. Kaldun, Y. Jiang, A. Senftleben, M. Kurka, R. Moshhammer, J. Ullrich, and T. Pfeifer.

Noisy Optical Pulses Enhance the Temporal Resolution of Pump–Probe Spectroscopy.

Phys. Rev. Lett. **108**, 098302 (2012).

C. Ott, A. Kaldun, P. Raith, K. Meyer, Y. Zhang, M. Laux, S. Hagstotz, T. Ding, R. Heck, and T. Pfeifer.

Quantum Interferometry and Correlated Two-Electron Wave-Packet Observation in Helium.

submitted to Nature (2012).

K. Meyer, C. Ott, P. Raith, A. Kaldun, Y. Jiang, A. Senftleben, M. Kurka, R. Moshhammer, J. Ullrich, and T. Pfeifer.

Enhancing temporal resolution in pump-probe experiments with noisy pulses.

Eur. Phys. J. Conferences: Ultrafast Phenomena. *accepted* (2012).

C. Ott, A. Kaldun, P. Raith, K. Meyer, Y. Zhang, M. Laux, S. Hagstotz, T. Ding, R. Heck, and T. Pfeifer.

Quantum Interferometry of Doubly-Excited States in Helium.

Eur. Phys. J. Conferences: Ultrafast Phenomena. *accepted* (2012).

Contributed talks (only as first author):

P. Raith, C. Ott, M. Schönwald, and T. Pfeifer.

Control of attosecond pulse generation using kinetic heterodyne mixing.

DPG-Frühjahrstagung 2010, Hannover.

P. Raith, C. Ott, and T. Pfeifer.

Attosecond Twin-Pulse Control by Generalized Kinetic Heterodyne Mixing.

DPG-Frühjahrstagung 2011, Dresden.

P. Raith, C. Ott, C. P. Anderson, A. Kaldun, K. Meyer, M. Laux, Y. Zhang, and T. Pfeifer.
Fractional High-order Harmonic Combs and Energy Tuning by Split-spectrum Field Synthesis.

DPG-Frühjahrstagung 2012, Stuttgart.

P. Raith, C. Ott, C. P. Anderson, A. Kaldun, K. Meyer, M. Laux, Y. Zhang, and T. Pfeifer.
Fractional high-harmonic combs by attosecond-precision split-spectrum pulse control.
XVIIIth International Conference on Ultrafast Phenomena, Lausanne, 2012.

P. Raith, C. Ott, C. P. Anderson, A. Kaldun, K. Meyer, M. Laux, Y. Zhang, and T. Pfeifer.
Fractional high-order harmonic combs and energy tuning by split-spectrum field synthesis.
Conference on Lasers and Electro-Optics, San Jose, 2012.

Selected poster presentations (only as first author):

P. Raith, C. Ott, M. Schönwald, and T. Pfeifer.
Control of attosecond pulse generation using kinetic heterodyne mixing
6th International Workshop on Optimal Control of Quantum Dynamics: Theory and Experiment; Schloß Ringberg, 2010.

P. Raith, C. Ott, M. Schönwald, M. Laux, and T. Pfeifer.
Control of attosecond pulse generation using kinetic heterodyne mixing.
International Summer School in Ultrafast Nonlinear Optics, Edinburgh, 2010.

P. Raith, C. Ott, C. P. Anderson, A. Kaldun, K. Meyer, M. Laux, Y. Zhang, and T. Pfeifer.
Attosecond Twin-Pulse Control by Kinetic Heterodyne Mixing.
XXVII International Conference on Photonic, Electronic and Atomic Collisions, Belfast, 2011.

P. Raith, C. Ott, C. P. Anderson, A. Kaldun, K. Meyer, M. Laux, Y. Zhang, and T. Pfeifer.
Fractional High-order Harmonic Combs by Pulse-Shape Control.
Gordon Research Conference: Quantum Control of Light & Matter, South Hadley, USA, 2011.

Contents

Abstract	i
List of Publications	iii
1 Introduction	1
2 Fundamentals	5
2.1 Ultrashort Laser Pulses	5
2.2 Strong Field Effects	7
2.3 High-order Harmonic Generation	8
2.3.1 Ionization	9
2.3.2 Propagation	12
2.3.3 Recombination	13
2.4 Coherent Control of High-order Harmonic Generation	15
2.5 Macroscopic Effects in High-order Harmonic Generation	17
2.5.1 Phase Matching	17
2.5.2 Temporal Gating Techniques	21
2.6 The Laser System	22
2.6.1 Oscillator, Amplifier and Compressor	22
2.6.2 Hollow-core Fiber	23
2.6.3 Dispersion Compensation	25
2.6.4 Phase Stabilization	27
2.6.5 Laser Pulse Measurement	29
2.7 The Attosecond Beamline	31
3 Control of High Harmonic Generation by the CEP	35
3.1 Carrier-envelope Phase Control of HHG	35
3.2 CEP-Control of Electron Dynamics	38
3.3 Carrier-Envelope Phase Spectral Interferometry	40
3.3.1 Method and Numerical Results	40
3.3.2 Experimental Results	41
3.4 Conclusion	43

4	Independent Control of Attosecond Pulse Generation	45
4.1	Principle	46
4.1.1	Definition of Independent Control	46
4.1.2	Two-Color Control of High-Harmonic Generation	47
4.1.3	Field Synthesis	48
4.1.4	Kinetic-Heterodyne Mixing of Laser Fields	49
4.2	Numerical Model	51
4.3	Control with the Second Harmonic	52
4.4	Control by the Split-Spectrum Time-Delay Method	54
4.5	Conclusion	56
5	Fractional High-order Harmonic Combs	59
5.1	Noninteger High-order Harmonic Generation	60
5.2	Design and Set-up of the Split-Spectrum Pulse Shaper	61
5.3	Numerical Model	63
5.4	CEP-averaged Results	64
5.4.1	Experimental Details	64
5.4.2	Beating of the Harmonic Intensity	64
5.4.3	Energy Tuning of the High Harmonics	66
5.4.4	Fractional High-order Harmonic Combs	68
5.4.5	Comparison to Simulations	71
5.4.6	Time-delay Asymmetries and Spectral Broadening	75
5.4.7	Effects of the Generalized Kinetic-Heterodyne Mixing of Laser Subfields	77
5.5	CEP-stable Results	82
5.5.1	Time-delay Dependence	82
5.5.2	CEP Dependence	83
5.5.3	Influence of Temporal Chirps	84
5.5.4	Fractional-Harmonic Comb Optimization	85
5.5.5	CEP Spectral Interferometry of the Fractional-Harmonic Combs	90
5.5.6	Subcycle Precision, Stability and Coherence	94
5.5.7	Influence and Independent Way of Action of the Individual Control Parameters	95
5.6	Applications	96
5.7	Conclusion	97
6	Conclusion	99
A	Adaptive Control of High-order Harmonic Generation	101
A.1	Method	101
A.2	Numerical Results	104
B	Atomic Units	107

List of Figures	109
Bibliography	119
Acknowledgements	135

Chapter 1

Introduction

In our macroscopic everyday world we are used to act and manufacture by applying mechanical forces to our surrounding things and we are able to observe these processes with our eyes or with cameras. In the microscopic world of atoms, molecules, clusters, etc. things behave differently, not only due to the dominance of quantum-mechanical effects. Above all, the processes in the microscopic world take place on a much faster ("ultrafast") time scale. The time scale on which electron dynamics evolves scales inversely to the energy difference between the involved quantum states. Especially the dynamics of electrons are of large scientific interest because pairs of electrons form the chemical bonds, and the electronic structures determine manifold properties of virtually any known materials. While the vibration, rotation and dissociation of molecules happen within several femtoseconds to nanoseconds ($1 \text{ fs} = 1 \text{ femtosecond} = 10^{-15} \text{ s}$), the dynamics of bound electrons in atoms occurs even faster, on the attosecond ($1 \text{ attosecond} = 1 \text{ as} = 10^{-18} \text{ s}$) time scale. To measure such ultrafast processes one needs probes of comparable duration, which reach into the attosecond regime for atomic electron dynamics. Ultrashort laser systems nowadays deliver coherent, pulsed light in the visible and infrared spectral range with pulse durations down to the low femtosecond time scale and have enabled tremendous insights into physics, chemistry and biology [1]. Yet these laser pulses themselves are not short enough to resolve the versatile electron dynamics evolving on the attosecond time scale.

Thus a process termed high-order harmonic generation (HHG) is commonly applied which converts parts of infrared or visible laser light into subfemtosecond flashes of coherent light in the extreme ultraviolet or soft x-ray spectral region. The light intensity of the driving optical field must be so high for this process that electrons bound within the atoms leave the atoms, are accelerated by the electric field of the laser and finally emit attosecond light pulses for the short instance when they—under certain conditions—recombine with their parent atom. In sophisticated experiments attosecond pulses of light allow to measure electron dynamics for example in atoms, molecules and clusters. In such experiments one does not only want to investigate randomly ongoing electron dynamics. Instead, the electromagnetic wave nature of the light enables us to act with considerable electric forces on the electrons given the light intensity is sufficiently high for such so called strong-field effects. This opens the door to manipulate quantum states, to steer electronic or molecular processes, to break chemical bonds, to trigger ionization processes

of atoms, or in more general words to *control* and measure quantum dynamics under well-defined conditions and with a temporal resolution which is in most cases roughly given by the pulse duration. Up to now HHG is the only available fully-coherent source of attosecond pulsed light. The application of attosecond pulses as precise tools for various experiments to exploit, trigger and especially to control attosecond electron dynamics makes it desirable to control the generation of attosecond pulses or to even tailor them in their temporal or spectral shape. This gives a strong motivation for the exploration of effective and comprehensive control mechanisms for high-order harmonic generation.

In this thesis, coherent control of high-order harmonic generation is experimentally and numerically performed at first purely by the variation of the so-called carrier-envelope phase (CEP) of the electric field of the driving few-cycle laser pulses. Secondly the combination of CEP and time-delay control between two spectral sections of the broadband laser spectrum is found to enhance the controllability especially when several spectral or temporal properties of the produced attosecond pulses or pulse trains have to be controlled at once. The spectral and temporal characteristics of the attosecond pulses are hereby mathematically connected by Fourier transform. As one main result, the multidimensional (multi-parameter) control scheme supports the controlled interference of two attosecond pulse trains, which leads to the observation of fractional high-harmonic combs. It is investigated how the relative phase between both, pairs of attosecond pulses and pairs of attosecond pulse trains, can be freely set with in each case adjustable relative intensities. Such precisely prepared pairs of fully coherent attosecond pulses or pulse trains are perfectly suited for spectral interferometry experiments in the extreme ultraviolet.

The work creates the fundamental building blocks to efficiently control HHG by a limited number of control variables with maximal impact on the spectral response and physical understandability with particular emphasis on the individual physical control mechanisms at work. We show how a number of pronounced spectral effects result from few distinct interventions into the spectral phase of the driving laser field and how these control options are either connected or independent. It is demonstrated that the relative phase of an already tiny portion of the driver spectrum can have a remarkably large impact on HHG. The origin of the observed effects can be identified in purely the modulated pulse shape of the few-cycle driver pulses, which in turn controls the single-atom response during HHG. The measured high-harmonic spectra are compared to numerical simulations based on the single-atom response to confirm this microscopic nature of the observed control effects.

This thesis is structured as follows: In chapter 2 the fundamental aspects of ultrashort laser pulses, strong-field effects and the process of high-order harmonic generation are explained. An introduction to the control of high-harmonic generation is given and macroscopic effects in HHG as well as different techniques to produce isolated attosecond pulses are reviewed. Further a description of the employed laser system and the attosecond beamline is given. Chapter 3 introduces the CEP of the driving laser field as a single variable to control HHG on the single-atom level. A spectral interferometry method is presented which allows to extract information on the time structure of the produced attosecond pulses only by observing their coherent spectral intensity response. In chapter 4 the CEP control of HHG is extended by the introduction of a time delay between either an additional laser field or between two spectral sections of the now segmented driver field itself. It is numerically studied to what extent these two control variables alone al-

low to independently set several temporal properties of the produced attosecond pulses at the same time. This independent multidimensional control approach would realize the most efficient control configuration. The control scheme is experimentally implemented and discussed in chapter 5. The modified driving laser field causes a number of distinct temporal and spectral effects for the recorded high harmonics, which are investigated individually and supported by numerical simulations. The respective HHG-control mechanisms are extracted which give a complete picture of the processes in the time domain. In particular the time-delay driven tuning of the high-harmonic energies is explained quantitatively by a modulation of the instantaneous frequencies of the driver pulses. Several applications of the generated fractional-harmonic combs are discussed before finally the results of this thesis are summarized in chapter 6.

Chapter 2

Fundamentals

In this chapter, the fundamental principles and techniques on which the further work is based are discussed. First a mathematical description of ultrashort laser pulses is given, before the interaction of light and matter as well as the fundamentals of nonlinear optics are discussed. The production of attosecond pulses by a highly nonlinear process termed high-order harmonic generation (HHG) and, finally, the technical aspects of the generation of ultrashort laser pulses are explained. The basic equations in this chapter can also be found in the literature (e.g. in Refs. [2, 3, 4]).

2.1 Ultrashort Laser Pulses

As light is an electromagnetic wave it is a suitable way to describe ultrashort laser pulses at a given spatial position by their time-dependent electric field. The real part of this electric field acts on charged particles and can be expressed in case of a linear polarization of the laser field by

$$E(t) = \mathcal{E}(t)\cos[\phi(t)]. \quad (2.1)$$

$\mathcal{E}(t)$ is the positive-valued pulse envelope function, which defines the temporal structure of the pulse and thus also the pulse duration. $\phi(t)$ is the temporal phase of the pulse. In calculations a Gaussian pulse shape $\mathcal{E}_G(t)$ is widely used, which can be defined by

$$\mathcal{E}_G(t) = \mathcal{E}_0 \exp \left[- \left(\frac{t}{t_G} \right)^2 \right]. \quad (2.2)$$

The temporal intensity, measured in W/cm^2 , is proportional to the square of the pulse envelope function of the electric field:

$$I(t) \propto \mathcal{E}^2(t). \quad (2.3)$$

The pulse duration is then usually defined as the full width at half maximum (FWHM) value t_{FWHM} of the pulse intensity profile $I(t)$, which yields for Gaussian shaped pulses:

$$t_G = \frac{t_{FWHM}}{\sqrt{2\ln 2}} \approx 0.849 t_{FWHM}. \quad (2.4)$$

As we will see later in this work, the temporal phase of a laser pulse plays an important role. It can be expressed by

$$\phi(t) = \phi_0 + \omega_c t + \varphi(t), \quad (2.5)$$

with a constant offset ϕ_0 , the central laser frequency ω_c and a residual phase $\varphi(t)$, which contains the higher orders (≥ 2) in time. ϕ_0 is called the carrier-envelope phase (CEP), since it defines the offset between the oscillating electric field carrier and its envelope $\mathcal{E}(t)$. $\phi_0 = 0$ means that both peak at the same time (see also Fig. 3.1).

The instantaneous laser frequency is the derivative of the temporal phase. It changes in time, if the nonlinear orders of the temporal phase are nonzero:

$$\omega(t) = \frac{d}{dt}\phi(t) = \omega_c + \frac{d}{dt}\varphi(t) \quad (2.6)$$

A continuous increase (decrease) of the instantaneous laser frequency with time is called up- (down) chirp. The expression "chirp" originates from the equivalent acoustic waves, which are found in the chirping of birds.

Due to the importance of the phases it is convenient to express the electric field as a complex field

$$\tilde{E}(t) = \mathcal{E}(t)\exp[i\phi(t)], \quad (2.7)$$

while only the real part is the measurable physical observable. Fourier transformation then obtains the field in the spectral domain

$$\tilde{\tilde{E}}(\omega) = \mathcal{F}[\tilde{E}(t)] = \int_{-\infty}^{\infty} dt \tilde{E}(t) e^{-i\omega t}, \quad (2.8)$$

and vice versa the time-dependent electric field is given by the inverse Fourier transform of the complex spectral field $\tilde{\tilde{E}}(\omega)$:

$$\tilde{E}(t) = \mathcal{F}^{-1}[\tilde{\tilde{E}}(\omega)] = \frac{1}{2\pi} \int_{-\infty}^{\infty} d\omega \tilde{\tilde{E}}(\omega) e^{i\omega t}. \quad (2.9)$$

This mathematical connection between the time and the spectral domain has important physical implications. Knowing (e.g. measuring) both amplitude *and* phase in one domain, we can calculate the field (again both amplitude and phase) in the other domain. Moreover, in terms of control, we can in principle generate any given laser pulse $\tilde{E}(t)$ by exploiting the spectral amplitude and spectral phase, encoded in $\tilde{\tilde{E}}(\omega)$. In the spectral domain the complex electric field can be written as

$$\tilde{\tilde{E}}(\omega) = \bar{\mathcal{E}}(\omega)\exp[i\phi(\omega)], \quad (2.10)$$

with the spectral envelope function $\bar{\mathcal{E}}(\omega)$ and the spectral phase $\phi(\omega)$. $\bar{\mathcal{E}}(\omega) = A(\omega)$ is positive valued, thus equals the spectral amplitude for $\omega \geq 0$. The spectral intensity, which is measurable with a spectrometer and is meant by the laser spectrum, is then given by

$$\bar{I}(\omega) \propto |\tilde{\tilde{E}}(\omega)|^2. \quad (2.11)$$

The spectral phase can be expanded by the Taylor series:

$$\phi(\omega) = \sum_{k=0}^{\infty} \frac{1}{k!} \frac{\partial^k \phi(\omega)}{\partial \omega^k} \cdot \omega^k = \phi_0 + \tau_0 \cdot \omega + \varphi(\omega), \quad (2.12)$$

where the linear phase in the spectral domain $\tau_0 \cdot \omega$ corresponds to an offset (τ_0) in the time domain. In the same manner, a linear phase in time $\omega_c \cdot t$ is a constant offset ω_c in the spectral domain. These offsets can be interpreted as mean-time and -frequency, around which the pulses are centered, while in the time domain the time zero is not defined and thus the offset $-\tau_0$ is arbitrary. The pulse does not need to contain a contribution at the center frequency ω_0 or the center time $-\tau_0$, these numbers are rather the center of mass values. Besides ϕ_0 , which is again the CEP, the important information is contained in the residual phase $\varphi(\omega)$, which includes the higher orders. The negative derivative of the spectral phase corresponds to a time delay $\tau(\omega)$ of the individual spectral frequencies, also called the group delay:

$$\tau(\omega) = -\frac{d}{d\omega} \phi(\omega) = -\tau_0 - \frac{d}{d\omega} \varphi(\omega). \quad (2.13)$$

In order to gain control over the laser pulses in time, we hereby have derived that we need to have control both over the laser spectrum $\bar{I}(\omega)$ and especially over the relative time delays between the spectral frequencies. Some basic technical aspects of this control will be discussed in section 2.6.

2.2 Strong Field Effects

For more than the last 50 years since the invention of the laser by Maiman [5, 6] a lot of effort has been made to generate shorter and shorter and thus also more intense laser pulses, where *Laser* is the acronym for "light amplification by stimulated emission of radiation"[7]. Already very early the invention of Q-switching [8] delivered laser pulses with durations below 100 ns realized by dye lasers, which was then further reduced by the invention of the mode-locked Ti:sapphire oscillator [2]. The technique of chirped pulse amplification (CPA) delivered routinely laser pulses with a pulse duration of sub-100 fs [9, 10] in the 1990s. The available pulse duration was further continuously decreased until the limit of a few laser cycles (for 750 nm light the laser cycle lasts 2.5 fs) was reached around 1999 [11]. The process of high-order harmonic generation (see section 2.3) then enabled to break the 1-fs barrier to now routinely produce attosecond pulses [12, 13, 14]. Parallel to this development the available pulse peak intensity was increased. This drastic increase of the available laser peak intensity is a requirement to reach still shorter pulses and was noticed and postulated over 18 orders of magnitude [15]. Today large laser facilities can deliver sub-ps pulses with peak powers in the petawatt range (1 PW=10¹⁵ W) [16]. The motivation to develop shorter coherent light sources that deliver higher intensities and pulse energies is manifold. The availability of ultrashort laser pulses enables the measurement, understanding, and control of processes which evolve on time scales which are longer or about as long as the ultrashort pulses. For example electron dynamics within a quantum mechanical system (e.g. atoms, biomolecules, solids)

can be studied and controlled, where the relevant time scale is given by the inverse of the energy spacing of involved quantum states.

By increasing the pulse intensities one can study different physical regimes. In the linear regime only one photon is absorbed at a time. Thus the process is proportional to the intensity and the refractive index is intensity-independent. In contrast, in the regime of nonlinear optics [17, 18] several photons can be absorbed at the same time and the refractive index becomes a function of the intensity. There are a number of low-order nonlinear processes known which lead to a conversion of light frequencies [19]. Among them are:

Second-harmonic generation (SHG):	$\omega_{SH} = 2\omega_1$	Frequency-doubled light at ω_{SH} is generated.
Sum-frequency generation (SFG):	$\omega_s = \omega_1 + \omega_2$	The addition of the frequencies ω_1 and ω_2 generates the frequency ω_s .
Difference-frequency generation (DFG):	$\omega_s = \omega_1 - \omega_2$	The subtraction of the frequency ω_2 from ω_1 obtains the frequency ω_s .
Third-harmonic generation (THG):	$\omega_{TH} = 3\omega_1$	Three photons at the frequency ω_1 produce the tripled frequency ω_{TH} .
Optical parametric generation (OPG):	$\omega_s = \omega_p - \omega_i$	The signal at ω_s is amplified by the pump field at ω_p leaving the idler at ω_i .

In the highly-nonlinear regime with intensities near 10^{14} W/cm² the strong electric field of the light acts with a time-dependent force $\vec{F}(t) = -e\vec{E}(t)$ on the bound electrons in atoms, molecules and solids, which is on the order of the Coulombic binding force. The interaction, which leads to the generation of high-order harmonics, will be studied in the next section in more detail. At even higher intensities (10^{18} W/cm²) the relativistic regime is reached, where electrons are accelerated by the light to energies which are close to or even multiples of their rest mass. As known from physics with conventional particle accelerators the creation of spontaneous electron-positron pairs out of the vacuum can be observed. The planned Extreme Light Infrastructure (ELI) project could finally reach peak intensities of 10^{23} W/cm² and produce even pions, muons and neutrinos from light-accelerated ultrarelativistic electrons [16].

2.3 High-order Harmonic Generation

In the perturbative regime, which we have discussed in the last section, light of the frequency ω and the intensity I can be converted to a frequency $n\omega$ with an efficiency, which

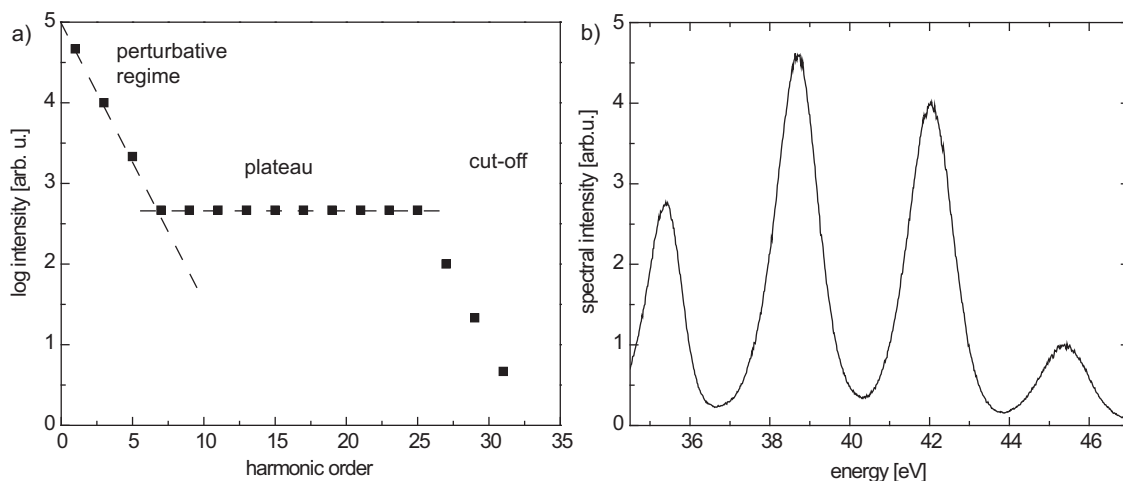


Figure 2.1: a) Schematic high-order harmonic spectrum consisting of discrete lines at odd multiples of the fundamental laser energy. After the perturbative decrease of the harmonic intensity as a function of the harmonic order n proportional I^{-n} , a plateau is observed, where the harmonic intensity is about constant. Finally the harmonic intensity drops again and a cut-off is reached beyond which the harmonics vanish. b) Typical measured spectrum of high-order harmonics in our experiment using argon as the conversion medium.

decreases exponentially with I^{-n} . Yet, it was found again and again when focusing an intense laser pulse into a noble-gas medium that for higher orders there is a huge anomaly. A plateau was found in the emission spectrum where the intensity of the harmonics, which were then called high-order harmonics, was roughly constant over a remarkable number of orders, before the harmonic intensity finally dropped again and a cut-off energy was found, above which no harmonics were created [20, 21]. It was also noticed that only the odd orders of the high harmonics were generated. Fig. 2.1a) shows for illustration schematically the harmonic intensity as a function of the harmonic order n , while in b) a high-order harmonic spectrum as typically measured is depicted. In 1993, Corkum and Kulander published a theory that was capable to explain the findings [22, 23]. In the following, the mechanism, which leads to the generation of the high-order harmonics and the above-mentioned findings are discussed at first from the quasi-classical point of view, as introduced by Corkum and Kulander, and then quantum-mechanically. Reviews of HHG and "attosecond physics" in general are given in the Refs. [24, 25, 26, 27, 28, 29].

2.3.1 Ionization

Corkum and Kulander explained the generation of high harmonics by a three-step model. HHG is divided into three sequential steps, whereby the first step is the ionization of the atom or molecule. The model studies the response of a single atom to an intense laser field. As will be described in section 2.5.1, HHG is the collective response of many atoms and thus is also influenced by macroscopic properties of the conversion medium, but by the restriction to one atom the basic mechanism of HHG can be understood and already a good agreement to the experimental findings is achieved.

We consider a single hydrogen atom, which is exposed to an electromagnetic light wave

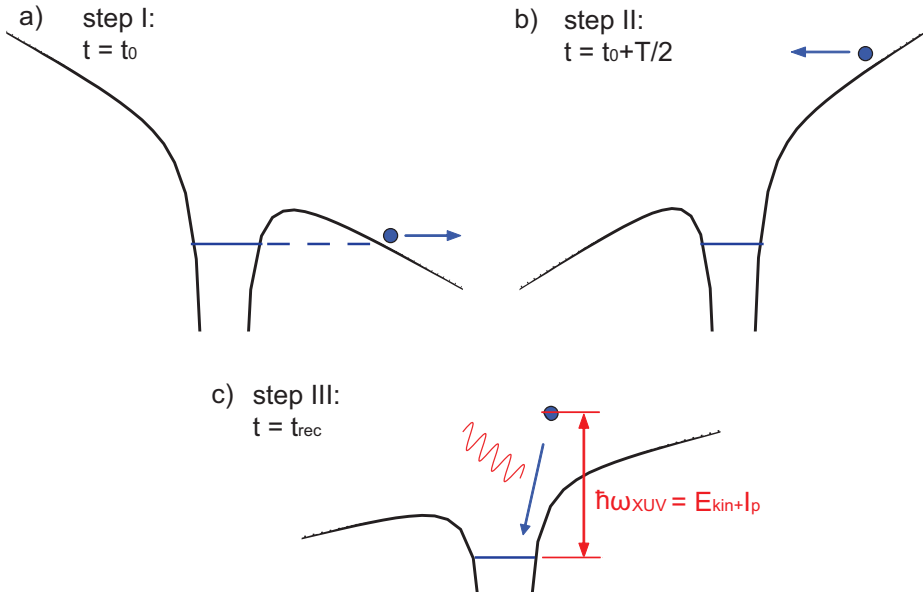


Figure 2.2: Three-step model of high-harmonic generation. A strong electric field interacts with a single atom and bends the Coulomb potential. a) As the first step a valence electron tunnels out into the continuum, where it is accelerated by the electric field. b) In the second stage a half-cycle later the electric field changes its sign and accelerates the electron back to its parent ion. c) In the third step, the electron recombines into its initial state, producing an extreme ultraviolet (XUV) photon, which carries the kinetic energy gained in the electric field plus the ionization potential of the atom.

$\vec{E}(t) = \vec{E}_0 \cos(\omega t)$. If the intensity is increased more and more, the electric field of the light becomes so strong that the Coulomb potential of the atom is significantly modified by $\vec{E}(t)$ and the electron thus feels the alternating external electric field. The Coulomb potential is bent by $\vec{E}(t)$ as illustrated in Fig. 2.2 and now reads

$$V(\vec{r}, t) = -\frac{e^2}{4\pi\epsilon_0 r} + e\vec{E}(t)\vec{r}. \quad (2.14)$$

If the electric field is strong enough, the electron is separated only by a small barrier on one side of the atom from the continuum (see Fig. 2.2). It can overcome this barrier by tunneling out. Once it is in the continuum it is considered to be free. Keldysh formulated a theory on this tunnel ionization induced by an electric field and calculated an electron tunneling rate, which can be expressed as

$$w_k = \frac{\sqrt{6\pi}I_p}{4\hbar} \left(\frac{eE\hbar}{m_e^{1/2}I_p^{3/2}} \right)^{1/2} \exp \left[-\frac{4\sqrt{2m_e}I_p^{3/2}}{e\hbar E} \left(1 - \frac{m_e\omega^2 I_p}{5e^2 E^2} \right) \right]. \quad (2.15)$$

Here, I_p is the ionization potential of the atom, E the temporal electric field strength, m_e and e the electron mass and electron charge unit, respectively.

Later, Ammosov, Delone and Krainov generalized Keldysh's ionization theory and made it suitable to arbitrary atoms and initial electronic states [30, 4]. Their ionization rate, which shows good agreement with experimental results, is often referred to as ADK-rate

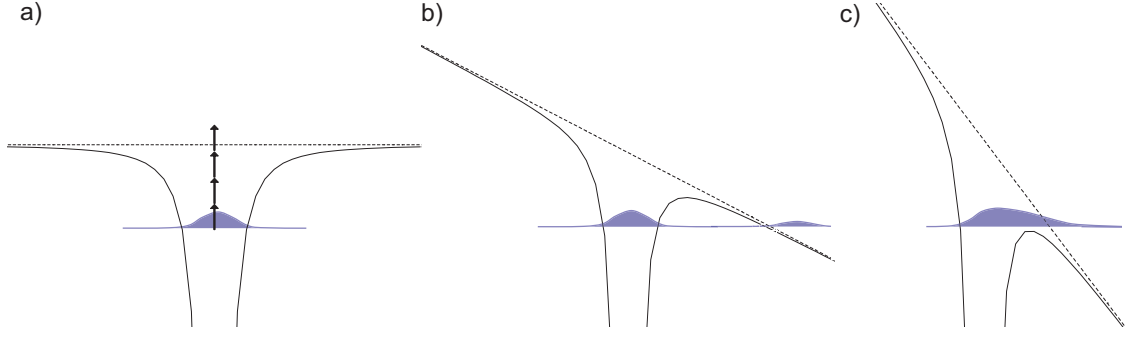


Figure 2.3: Different regimes of ionization in a laser field. a) Multi-photon ionization. b) Tunnel ionization. c) Over-barrier ionization.

and reads using atomic units ($\hbar=m=e=1$):

$$w_{ADK} = \sqrt{\frac{3E}{\pi(2I_p)^{3/2}}} |C_{n^*l^*}|^2 f(l, m) I_p \left(\frac{2(2I_p)^{3/2}}{E} \right)^{\left(\frac{2Z}{\sqrt{2}I_p} - |m| - 1 \right)} \exp\left(-\frac{2(2I_p)^{3/2}}{3E} \right), \quad (2.16)$$

with the factor $f(l, m)$ given by

$$f(l, m) = \frac{(2l+1)(l+|m|)!}{2^{|m|}(|m|)!(l-|m|)!}, \quad (2.17)$$

and the constant $|C_{n^*l^*}|^2$ by

$$|C_{n^*l^*}|^2 = \frac{2^{2n^*}}{n^* \Gamma(n^* + l^* + 1) \Gamma(n^* - l^*)}. \quad (2.18)$$

m and l are the angular momentum and magnetic quantum number respectively and Z is the ion charge after the ionization. The effective principal and angular momentum quantum numbers are written as $n^* = Z(2I_p)^{-1/2}$ and $l^* = n^* - 1$ respectively. For a review on Keldysh theory see Ref. [31].

Being dependent on the ionization potential I_p and the ponderomotive potential U_p (defined in Eq. 2.22) the ionization takes place in three different regimes. These regimes are characterized by the Keldysh parameter

$$\gamma = \sqrt{\frac{I_p}{2U_p}}, \quad (2.19)$$

and illustrated by Fig. 2.3:

- The multi-photon ionization regime ($\gamma \gg 1$): The Coulomb potential is hardly influenced by the external electric field so that multiple photons need to be absorbed to ionize the atom [32].
- The tunnel ionization regime: The Coulomb potential is bent so strongly that the electron can tunnel out with the tunneling rate given by the ADK-rate. For $\gamma \approx 1$ both multi-photon ionization and tunnel ionization are present.

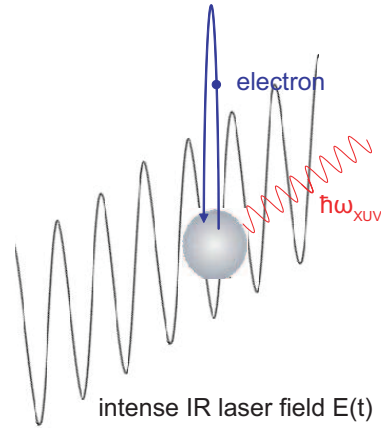


Figure 2.4: Atomic conversion of intense infrared (IR) laser light into coherent attosecond pulses of extreme ultraviolet light by high-order harmonic generation.

- Above-barrier ionization: The Coulomb potential is bent so much that the electric field barrier is suppressed even below the ionization potential. As a consequence the electron wave-packet can evolve freely above the barrier into the continuum.

2.3.2 Propagation

Once ionized, the electron is no longer bound to the atom and is accelerated in the laser field. We consider now a linearly polarized electric field that has the phase φ at the ionization time zero: $E(t) = E_0 \cos(\omega t + \varphi)$. We can classically calculate the electron velocity as a function of the time:

$$v(t) = v_0 + \int_0^t -\frac{e}{m_e} E(t') dt' = -\frac{eE_0}{m_e\omega} [\sin(\omega t + \varphi) - \sin(\varphi)]. \quad (2.20)$$

For $v_0 = 0$ the trace of the field-driven electron is then given by

$$x(t) = \int_0^t v(t') dt' = \frac{eE_0}{m_e\omega^2} [\cos(\omega t + \varphi) - \cos(\varphi)] + \sin(\varphi)t, \quad (2.21)$$

where $x = 0$ is the position of the remaining ion nucleus. The acceleration of the ion in the electric field can be neglected due to the much higher mass of the ion compared to m_e . Since the electric field changes its sign, the electron is driven back to the ion one half-cycle after the ionization. Given a linear polarization of the laser field, the returning electron can hit the ion. In reality, most electrons miss the ion due to the quantum dynamical spread (dispersion of a free-electron wavepacket) of the electron wave packet, which increases with the time spent in the continuum.

During its propagation in the electric field the electron is accelerated and gains kinetic energy. For an electron being at rest before the laser pulse the temporal average of the gained kinetic energy is given by

$$U_p = \frac{e^2 E_0^2}{4m_e\omega^2}, \quad (2.22)$$

and denoted as the ponderomotive potential.

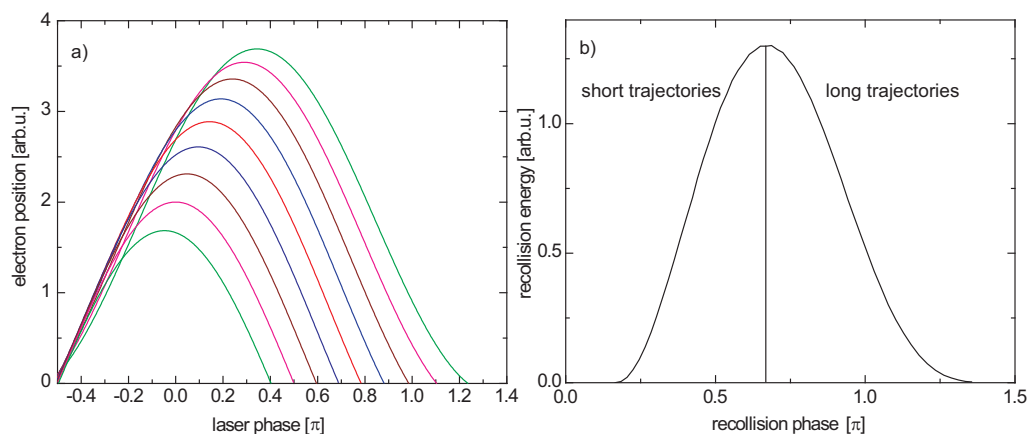


Figure 2.5: a) Classically calculated electron trajectories in a cosine-like electric laser field. b) Kinetic energy of the electrons gained in the electric field as a function of the laser phase at recollision. Every energy is obtained by two trajectories spending different times in the field, which gives their denotation as short and long trajectory.

2.3.3 Recombination

When the electron returns to its parent ion it can recombine to its original bound state, emitting a high-energy photon, whose energy is given as the sum of the kinetic energy of the electron and the ionization potential I_p :

$$\hbar\omega_n = E_{kin} + I_p. \quad (2.23)$$

The kinetic energy which the electron has gained in the electric field depends here on the phase φ of the electric field at the ionization time. The maximum kinetic energy the electron can obtain by a variation of φ is limited to $\approx 3.17 U_p$. This obtains the before-mentioned cut-off energy, above which no harmonics are produced:

$$\hbar\omega_{cut\ off} = 3.17U_p + I_p. \quad (2.24)$$

Fig. 2.5a) illustrates a number of electron trajectories starting at different laser phases, while in b) the recollision energy of the electrons is plotted as a function of the recollision time. We see that always two trajectories lead to the same recollision energy (except for the one leading to the cut-off energy). The ones spending a shorter time in the continuum are called short trajectories, the other ones are the long trajectories. The time-dependent recollision energy of the electrons leads to a corresponding intrinsic temporal variation of the energy/frequency contributions within the generated attosecond pulse, which is termed "attochirp" [33, 34]. The short trajectories produce positively chirped attosecond pulses while the pulses resulting from the long trajectories are negatively chirped. A method to create attochirp-free high harmonics is proposed in Ref. [35].

In order to extend the harmonic cut-off energy, it is most appropriate to increase U_p . We therefore reexamine Eq. 2.22 and see that there are two options to enlarge U_p . The first one is increasing the laser intensity and consequently the peak electric field strength E_0 , while the second option is the application of longer laser wavelengths since U_p scales with λ^2 .

While usually wavelengths around 800 nm are used, commonly produced by Ti:Sapphire laser systems, HHG has meanwhile also been performed utilizing mid-infrared driver wavelengths [36, 37, 38].

In the quantum-mechanical treatment the electron is described by its wave function $\Psi(\vec{r}, t)$. The high-harmonic radiation results from the nonlinear dipole response of the atom. Thus $\Psi(\vec{r}, t)$ has to fulfill the time-dependent Schrödinger equation, which in this case reads

$$i\frac{\partial}{\partial t}|\Psi(\vec{r}, t)\rangle = \left(-\frac{1}{2}\nabla^2 + V(\vec{r}) + \vec{r}\vec{E}\cos(\omega t)\right)|\Psi(\vec{r}, t)\rangle. \quad (2.25)$$

We consider only a single electron, which is known as the single-active electron approximation [32]. At the time of ionization a part of the wave function is removed from the atom, evolves freely in the electric driver field during the propagation and spreads in space along the way. At the time of recollision the wave function interferes with the remaining main part of the wave function, leading to a fast nonlinear dipole oscillation. As a consequence upconverted light is emitted for a duration of typically a few hundreds of attoseconds, forming an attosecond pulse in the extreme-ultraviolet spectral range.

In the strong-field approximation the time-dependent dipole moment $\vec{\mu}(t) = \langle\Psi(\vec{r}, t)|-\vec{r}|\Psi(\vec{r}, t)\rangle$ is given by [28]

$$\begin{aligned} \vec{\mu}(t) = & i \int_0^t dt' \int d^3\vec{p}_{can} E \cos(\omega t') \cdot \vec{d}(\vec{p}_{can} + \vec{A}(t')) \cdot \\ & \exp(-iS(\vec{p}, t, t')) \cdot \vec{d}^*(\vec{p}_{can} + \vec{A}(t')) + c.c. \end{aligned} \quad (2.26)$$

Here $\vec{A}(t)$ is the vector potential of the laser field, \vec{p}_{can} denotes the canonical momentum

$$\vec{p}_{can} = \vec{v} - \vec{A}(t), \quad (2.27)$$

and $S(\vec{p}, t, t')$ the so-called quasi-classical action

$$S(\vec{p}, t, t') = \int_{t'}^{t''} \left(\frac{(\vec{p}_{can} + \vec{A}(t''))^2}{2} + I_p \right) dt''. \quad (2.28)$$

The dipole moment in Eq. 2.26 contains the three-step model, since $\vec{d}(\vec{p}_{can} + \vec{A}(t'))$ corresponds to the ionization at time t' , $\exp(-iS(\vec{p}, t, t'))$ to the propagation in the electric field and $\vec{d}^*(\vec{p}_{can} + \vec{A}(t'))$ to the recombination to the ground state at time t . This quantum mechanical description of the three-step model was formulated by Lewenstein *et al.* [39]. For its solution the principle of the stationary action

$$\vec{\nabla}_p S(\vec{p}, t, t') = 0 \quad (2.29)$$

can be applied. Employing Feynman's path-integral approach one finds that very few electron trajectories (so-called "quantum orbits") have to be considered to reproduce the experimental findings [40].

In a joint side project of this thesis HHG was theoretically studied in a more general view [41]. It was discovered that high-order harmonics can not only be produced when the part of the electron wave function in the continuum interferes with the bound wave function, as described by the recombination step of the three-step model. In addition the interference of two separately ionized wave packets of the same electron in the presence of the Coulomb potential leads to a strong oscillation of the dipole moment and to the generation of high-order harmonics as well. While usually the contribution of this continuum-continuum HHG is negligible with respect to the well-known continuum-bound HHG, it can exceed the latter contribution, when the ground state is depleted by a strong laser field, and can be isolated from the continuum-bound harmonics by phase matching [41, 42].

Given a sufficient field strength, ionization (the first step in the three-step model) occurs every half-cycle of the laser field. This leads to the production of a train of attosecond pulses with the individual attosecond pulses being spaced in time by a half cycle, respectively [43, 44]. The temporal structure of the attosecond pulses and the spectrum of the high-order harmonics are mutually dependent, as the spectral amplitude $\tilde{E}(\omega)$ of the high-order harmonics is given by the Fourier transform of the time-dependent electric field of the attosecond pulses:

$$\tilde{E}(\omega) = \mathcal{F}[\tilde{E}(t)] = \int_{-\infty}^{\infty} dt \tilde{E}(t) e^{-i\omega t}. \quad (2.30)$$

The half-cycle spacing of the attosecond pulses in time results by Fourier transform in a spectral distance of twice the fundamental energy $\hbar\omega_0$ of the driver laser field—with the consequence that only the odd high-order harmonics are produced.

Since the process of HHG is governed by electron dynamics the harmonic spectrum already provides manifold information about the involved quantum states of the parent ions with an attosecond resolution [45]. This information can be retrieved by the so-called high-harmonic spectroscopy [46, 47]. Being now familiar with the process of HHG, fundamental aspects of coherent control with a focus on coherent control of HHG shall be discussed in the following section.

2.4 Coherent Control of High-order Harmonic Generation

The control of ultrafast processes, for example quantum control in femtochemistry [48, 49], is of interest to a large scientific community. A review of quantum control can be found in Refs. [50, 51]. Control means that one or several measurable quantities of a physical system can be influenced by one or several other quantities, which are termed control parameters or control variables. Thus, studying the controllability reveals the connections between physical quantities of the studied system, for instance the controlled quantity is a function of the control parameters. By revealing such connections we can learn something about the physics of the system that is controlled. Besides this aspect of understanding there is the more technical aspect that control means that we can steer a

physical property of the controlled system. The control might even be iteratively applied. This means that a controlled quantity itself serves as control variable for the control of further quantities. This way the access to and control of physical properties can be enhanced to an in principle unlimited number of physical quantities or properties of an increasingly complex setup. In particular, it is the "long-standing dream" of coherent quantum control to selectively form and break chemical bonds, to steer molecular dynamics or to manipulate electronic structures and dynamics in various quantum systems ranging from atoms to clusters, solids and complex biomolecules [52]. One important application in this context is optimization, for which control is a prerequisite. Another application is the preparation of well-defined initial states and conditions of physical systems. In this thesis the dispersion and more precisely the spectral phase of few-cycle laser pulses is controlled to shape these ultrashort pulses in time. Such well-controlled optical waveforms are then applied for high-order harmonic generation. Here, by steering the electron trajectories in the shaped electric field of the ultrashort pulses, the generation of attosecond pulses is controlled in both spectral and temporal properties. Such controlled attosecond pulses could then be further utilized to measure or control electron dynamics in atoms or molecules [53]. Especially attosecond pulse trains are suitable to control strong field processes by predominantly selecting a single quantum path [54]. The process of high-order harmonic generation provides access to both the natural time scale of electron dynamics even for core electrons and the high spatial resolution defined by wavelengths of down to ~ 10 nm in the extreme ultraviolet (XUV) or soft x-ray spectral region [28].

The most important property of the control with ultrashort optical pulses as utilized in this thesis is its coherence. Coherence means that not only the amplitudes but also the relative spectral phases of the pulses are well defined. For the ultrashort pulses in our setup as well as for the generated attosecond pulses, the spectral phase are always precisely given except for an offset ϕ_0 which fluctuates from laser shot to laser shot. These well-defined relative phases lead to pronounced interference patterns both in the time and the spectral domain, which are in huge contrast to the pure superpositions which are expected in the incoherent case. While it is possible to cancel out intensity (or probability) by the coherent addition of a second laser field (or quantum wave function) at a certain energy, time or location due to destructive interference, this is not possible by the incoherent intensity superpositions. High-order harmonic generation was found to be a coherent process [55, 56]. This enables us to coherently control both the spectral amplitudes and phases of the produced attosecond pulses by the coherent control of the applied driver field. In this thesis the control of the ultrafast driver pulses and then subsequent control of the high harmonics is performed by manipulating purely the relative spectral phase of the driver pulses that are utilized for HHG. The work thus demonstrates the power of these phases for HHG control.

There are different ways to control HHG, on a macroscopic and a microscopic scale. Macroscopic control utilizes properties of the generation medium as well as the geometric conditions to influence the production and above all the propagation of attosecond pulses. Several gating techniques can be applied to reduce the number of generated attosecond pulses to a few, or to produce an isolated attosecond pulse. After describing the macroscopic aspects of HHG in the next section we will return to the microscopic control of HHG, which is realized by manipulating the driver field by the carrier-envelope phase

in chapter 3 and additionally by means of a second laser field in chapter 4.

Another approach for control of HHG applicable when molecules are used for the generation is based on the alignment of these molecules. Alignment means that the molecules are rotated such that they are all parallel to a given axis (e.g. the laser polarization), while orientation is an even stricter requirement, which additionally requests that the top and the bottom side of the molecules (in case the molecule is asymmetric) must not be inverted. It was experimentally shown for the linear molecule CO_2 that the spectral intensity $\bar{I}(\omega)$ and the spectral phase of the produced harmonics depend on the alignment angle [57]. The control originates from interference effects of the laser-driven electron wave packet with the core, which depend on the angle of the recolliding electrons, determined by the laser polarization and the molecular axis. This further leads to a modification of the intensities of the individual attosecond pulses within the pulse train and thus to attosecond pulse shaping.

The control approaches in this work are fundamentally different from methods which reshape the attosecond pulses—after they have been produced by conventional HHG—by directly manipulating their amplitude and/or phase in the XUV-region. In 2005, López-Martens *et al.* produced the to that date shortest attosecond pulse with a duration of 170 as by compensation for the most part of the intrinsically non-flat spectral phase of the attosecond pulses by the dispersion caused by three 200 nm thick aluminum foils [58]. A more recent option for pulse compression in the XUV are specially designed multilayer mirrors [59, 60].

2.5 Macroscopic Effects in High-order Harmonic Generation

While the focus of HHG control in this work lies on the microscopic control of HHG, which is given by the time-dependent single-atom response to the electric field of the shaped driving laser pulse, there are a number of macroscopic effects (for a review see Ref. [61]) involved in HHG which are now discussed. This leads us to conditions for the generation of isolated attosecond pulses, for which common techniques are presented.

2.5.1 Phase Matching

In practice the attosecond pulses are not produced from a single atom, but from a large number of atoms, so that the recorded HHG signal results from the interference of all produced pulses, and propagation effects in the generation medium become important. For the determination of the relative phases of the attosecond pulses produced from individual atoms three contributions are important [28, 4]:

1. The neutral dispersion: It arises from the fact that the speed of light depends on the refractive index $n(\omega)$ of the generation medium, which is in turn dependent on the spectral frequency ω . Thus the attosecond pulses travel with a different speed in the

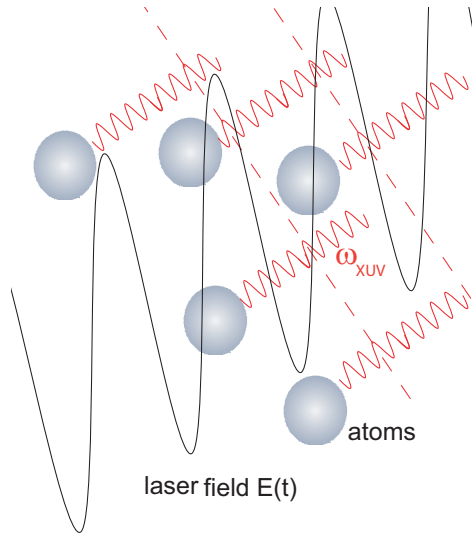


Figure 2.6: Phase matching of high-order harmonic generation. The attosecond pulses produced coherently by many atoms in the conversion medium need to interfere constructively for the build-up of a macroscopic HHG signal, which can be achieved when the driver field and the XUV light travel in phase with the same phase velocity.

generation medium than the near-infrared driver pulses at ω_f . With the wavevector depending on the refractive index

$$k_{disp.}(\omega) = \left(n(\omega) - 1\right) \frac{\omega}{c}, \quad (2.31)$$

we can calculate the wavevector mismatch (=difference) for the m th harmonic at the spectral frequency $m\omega_f$ with respect to fundamental field:

$$\Delta k = mk(\omega_f) - k(m\omega_f), \quad (2.32)$$

$$\Delta k_{disp.}(\omega) = mk_{disp.}(\omega_f) - k_{disp.}(m\omega_f) = \left(n(\omega_f) - n(m\omega_f)\right) \frac{m\omega_f}{c} \quad (2.33)$$

The refractive index is in general higher for the driver pulse at ω_f (in the infrared or visible region) than for the attosecond pulses at $m\omega_f$ in the extreme ultraviolet. Thus, we obtain:

$$\Delta k_{disp.} > 0. \quad (2.34)$$

The neutral dispersion can be controlled by the choice of the conversion medium (different gases, etc.). For this purpose also different gases can be mixed [62].

2. The plasma dispersion:

The strong electric driver field ionizes a large number of atoms in the generation medium. Only a small fraction of the freed electrons recombine directly within the third step of the high-harmonic generation model. The remaining electrons miss the atom and stay free for a much longer time than the driver pulse length (several ns), creating a plasma, whose electron density is increasing in time by this process

during the driver pulse. The freed electrons oscillate with the electric driver field around their ionic parent atoms, for what the resonance (termed plasma frequency) is given by

$$\omega_p = \sqrt{\frac{e^2 N_e}{\epsilon_0 m_e}}. \quad (2.35)$$

Here, N_e is the free electron density, e the unit charge, ϵ_0 the dielectric constant and m_e the electron mass. The plasma resonance leads to a polarizability of the generation medium and thus to a frequency-dependent refractive index of the generation medium:

$$n_{plasma}(\omega) = \sqrt{1 - \left(\frac{\omega_p}{\omega}\right)^2} = \sqrt{1 - \frac{N_e}{N_c(\omega)}} \quad (2.36)$$

with the critical plasma density

$$N_c = \frac{\epsilon_0 m_e \omega^2}{e^2}. \quad (2.37)$$

At the critical plasma density the plasma becomes completely intransparent. For typical field strengths, gas densities, and a driver wavelength of about 750 nm, the free-electron density is much lower than the critical plasma density, so that we can approximate the refractive index in the plasma by

$$n_{plasma}(\omega) \approx 1 - \frac{1}{2} \left(\frac{\omega_p}{\omega}\right)^2. \quad (2.38)$$

It arises then for the wavevector

$$k_{plasma}(\omega) = (n_{plasma}(\omega) - 1) \frac{\omega}{c} = -\frac{\omega_p^2}{2c\omega}, \quad (2.39)$$

and thus for the wavevector mismatch

$$\Delta k_{plasma}(\omega) = m k_{plasma}(\omega_f) - k_{plasma}(m\omega_f) = \frac{\omega_p^2(1 - m^2)}{2mc\omega_f}. \quad (2.40)$$

Hence, the plasma contribution to the wavevector mismatch is negative:

$$\Delta k_{plasma} < 0. \quad (2.41)$$

3. The geometrical dispersion: In the following we consider the situation that the driving laser field is focused into the generation medium by a focusing mirror as in our experimental realization. The geometrical dispersion is different for HHG in a guided geometry, e.g. in a capillary. In the laser focus the beam waist w_0 is determined by the focal length f , the wavelength and the beam radius w on the focal mirror

$$w_0 = \frac{f}{\pi w} \lambda, \quad (2.42)$$

while the beam radius is a function of the z -position, according to

$$w(z) = w_0 \sqrt{1 + \left(\frac{z}{z_R}\right)^2} \quad (2.43)$$

with the Rayleigh length

$$z_R = \frac{\pi w_0^2}{\lambda}. \quad (2.44)$$

This holds true for a previously collimated laser beam. We can define a space-dependent wavevector $\vec{k}(\vec{r})$ as the derivative of the space-dependent phase $\Phi(z)$:

$$\vec{k}(\vec{r}) = \vec{\nabla} \Phi(\vec{r}). \quad (2.45)$$

For our focus geometry the spatial phase is given by

$$\Phi_{geo.}(z) = \arctan\left(\frac{\lambda z}{\pi w_0^2}\right) = \arctan\left(\frac{2z}{b}\right). \quad (2.46)$$

This spatial phase is called the Gouy phase and turns from $-\frac{\pi}{2}$ to $+\frac{\pi}{2}$ by passing through the focus. Its influence on focused few-cycle laser pulses was first measured in Ref. [63]. The Gouy phase produces a geometrical contribution to the wavevector, which we can approximate for a small range around the focus ($z \ll b$) to

$$k_{geo.}(z) = \frac{d\Phi_{geo.}(z)}{dz} \approx -\frac{2}{b}. \quad (2.47)$$

Here, b is the confocal parameter $b = 2\pi w_0^2/\lambda = 2z_R$. Thus, the geometric contribution to the wavevector mismatch is negative:

$$\Delta k_{geo.} = m k_{geo.}(\omega_f) - k_{geo.}(m\omega_f) = \frac{2(1-m)}{b} < 0. \quad (2.48)$$

The attosecond-pulse generation is most efficient for

$$\Delta k = \Delta k_{disp.} + \Delta k_{plasma} + \Delta k_{geo.} = 0. \quad (2.49)$$

In this case the attosecond pulses travel in phase with the driver field and the contributions of all atoms add up constructively. This condition is called phase matching. For $\Delta k \neq 0$ the conversion efficiency decreases and can be described by

$$I(L) \propto L^2 \text{sinc}^2\left(\frac{\Delta k L}{2}\right), \quad (2.50)$$

where L is the propagation length in the conversion medium [4].

Phase-matched HHG in a gas-filled capillary waveguide was experimentally demonstrated in 1998 by Rundquist *et al.* [64]. Today, the production of phase-matched soft x-ray high harmonics by tabletop wave-guides with energies up to 1600 eV have been experimentally realized [65, 66] and the extension to hard x-rays in the multi-keV range has been predicted [37].

In the focused geometry, after choosing the geometrical parameters such as the focal length and the length of the generation medium, the phase-matching conditions and thus also the harmonic yield can be controlled by:

- the z -position of the generation medium with respect to the focus position of the laser field, which determines the Gouy phase.
- the choice of the gas(es) and the gas pressure. The ionization potential of the gas affects the ionization rate and thus the plasma density as well as the rate of electron recollisions.
- the laser power, which implies at a given geometry the peak intensity as a function of the z -position.

See Ref. [67] for a detailed study of the phase-matching conditions and the resulting harmonic yields for the same HHG geometry as applied in our experimental setup. The simulations show that for high peak intensities (>0.13 a.u.) the phase-matching efficiency typically drops drastically within the laser pulse after a few half-cycles due to an increased plasma density.

2.5.2 Temporal Gating Techniques

In the process of traditional HHG attosecond pulses are in general produced every half-cycle of a multi-cycle driving laser field. Several techniques have been developed to reduce the number of attosecond pulses or to especially generate a single, isolated attosecond pulse (IAP) [68]. For this purpose the generation of attosecond pulses at more than one half-cycle has to be averted, e.g. by leaving only a short temporal gate open for HHG [69]. Short IAPs are ideally suited to probe attosecond electron dynamics induced commonly by a more intense few-cycle fs laser pulse. Since the conversion efficiency of HHG is low ($\sim 10^{-5}\%$ of the driver pulse intensity), experiments with IAPs both for pump and probe are usually not applicable [53]. Much effort in the field is devoted to shortening the pulse duration of the IAPs and to increase their comparably still low intensity [70, 71]. One approach is based on the fact that the harmonic cut-off energy depends on the intensity of the driver field. Applying spectral filters, usually foils of metals like zirconium, which remove the low-order harmonics, the production of attosecond pulses is restricted to the half-cycles where the instantaneous driver intensity $I(t)$ is above a threshold I_{thres} . This gating method is accordingly called intensity gating. For the control of high harmonics in our work it implies the important consequence that we have to control the shape of only these few half-cycles where the intensity is high enough for the generation of harmonics in the accessible energy range.

Another important gating technique can be understood with the three-step model. For HHG in atoms it is necessary that the electron returns for recombination to its parent atom, which is classically given for a linear polarization of the laser field, but not for an elliptically polarized field. Quantum dynamically a small part of the wave function still reaches the atom due to the wave packet delocalization and size of the atom, but the fraction is typically reduced by a factor of ten for ellipticities between 0.1 and 0.2 compared to the linear polarization [72]. Thus by temporally varying the ellipticity of the driving laser field a short gate for HHG can be created. Corkum *et al.* [12] suggested and Sansone *et al.* as well as Sola *et al.* [73, 74] demonstrated experimentally that an isolated attosecond pulse can be produced by this technique, which is termed polarization gating.

In contrast to gating by spectrally selecting the highest harmonics [75] the full spectral bandwidth can be used, which is advantageous for the creation of a very short isolated attosecond pulse. The generation of an isolated attosecond pulse can also be achieved by shaping the driver field with the addition of a second or even a third driver laser field at different frequencies. In chapter 4 we will, among other things, discuss the prospects of two-color or multi-color control schemes in the view of the IAP- or isolated-double-pulse production. The methods of polarization gating and two-color control can be combined for the generation of IAPs, which is termed double optical gating [76, 77]. The contrast of the generated IAP can be measured with respect to weak remaining pulses in case there are any by analyzing the photoelectron spectrum when both the attosecond pulses and the driving laser field are refocused into a gaseous medium [78].

A further gating mechanism is based on the rapidly ongoing ionization induced by an intense driver pulse. When all atoms are ionized no attosecond pulses can be produced any more due to ground-state depletion [79]. By the control of the macroscopic phase matching the temporal gate can be closed even earlier on the leading edge of the driver pulse [80, 81]. The reason is that already a comparably small plasma density can lead to a phase mismatch $\Delta k \neq 0$, which suppresses the macroscopic generation of attosecond pulses. This way the increased ionization within a single half-cycle of a 3.3-fs pulse enabled the experimental generation of a sub-100-as pulse [75] without the need of polarization gating or a second laser field. A recent overview over the different gating techniques in HHG has been published in Ref. [70].

2.6 The Laser System

For the HHG-control experiments which are the major goal of this work phase-stabilized few-cycle laser pulses with a peak intensity on the order of several 10^{14} W/cm² when focused to a typical spot size of ~ 50 μm are required. The laser system which delivers such intense ultrashort pulses in the visible to near-infrared range is described in this section along with the applied techniques to broaden the spectral bandwidth of the pulses, to compress them to their bandwidth-limited length, to control their absolute phase ϕ_0 and to determine their temporal duration. The laser system was newly set up, equipped with a self-made monitoring system and is further described in Ref. [3].

2.6.1 Oscillator, Amplifier and Compressor

In our setup the commercially available [82] laser system "Femtopower Compact pro CEP" is utilized. It consists of an oscillator, amplifier and compressor and delivers amplified sub-30 fs long, CEP-stabilized pulses at a center wavelength of 800 nm with a repetition rate of 4 kHz and pulse energies of a few mJ. The details of the CEP stabilization are given in section 5.5.2. The oscillator provides sub-10 fs long laser pulses at a high repetition rate of typically 80 MHz with low pulse energies in the nJ-range. Thus the pulses are subsequently amplified to a pulse energy of up to 0.8 mJ by a technique termed chirped pulse amplification [83]. If the pulses kept their original pulse duration the intensity in the amplifier crystal would be high enough to damage the crystal. To avoid this

a thick fused silica glass plate is employed to introduce a temporal chirp on the pulses, which increases the pulse duration to a few ns and thus drops the peak intensity below the damage threshold. Both in the oscillator and the amplifier a titanium-doped sapphire crystal ($\text{Ti:Al}_2\text{O}_3$, or shortly Ti:Sa) is employed as the gain medium. The pulses are guided 9 times through the amplifier crystal, which is pumped with a high optical power of ~ 28 W by a Q-switched diode laser (DM-30, Photonics Industries). The pump laser is synchronized to the amplifier repetition rate of 4 kHz. After amplification the chirped pulses are finally compressed to close to their bandwidth-limited duration (< 30 fs). This is realized utilizing a compressor built up of two precisely arranged prisms and special "chirped" mirrors which are capable of compensating higher orders of dispersion (see section 2.6.3).

2.6.2 Hollow-core Fiber

For the generation of few-cycle pulses a large spectral bandwidth is required since the Fourier-limited pulse duration scales inversely with the optical bandwidth: A two-cycle laser pulse at $\lambda = 750$ nm with $t_{FWHM} = 5$ fs for example requires a bandwidth $\Delta\omega_{FWHM} = 0.57$ fs $^{-1}$. A cycle number as low as technically realizable is favorable for the observation of CEP effects (which are then most pronounced), the application of CEP control of HHG and the generation of few or isolated attosecond pulses. An effect termed self-phase modulation (SPM) helps to broaden the originally available bandwidth and is described in the following. It is based on the fact that the refractive index is significantly intensity dependent for high intensities of the laser field, which can to the first order be approximated with the nonlinear index coefficient n_2 in the Taylor series expanded in powers of the intensity [17]:

$$n(I) = n_0 + n_2 I(t) + \dots \quad (2.51)$$

This is in contrast to the linear optics at low or moderate intensities, where the refractive index does not or only insignificantly depend on the intensity. Within the duration of the laser pulse there is at first a drastic increase of the temporal intensity $I(t)$ until the peak intensity is reached, followed by a likewise drastic decrease of the intensity in the second half of the laser pulse. Thus an intense laser pulse experiences a significant temporal variation of the refractive index of the medium during its propagation through it. The change of the refractive index affects the instantaneous frequency of the laser pulse, which is given by

$$\omega(t) = \frac{d\phi(t)}{dt} = \omega - \frac{dn(t)}{dt} \frac{\omega}{c} z, \quad (2.52)$$

with the propagation length z . At the rising-intensity edge of the pulse, the instantaneous frequency is lower, which means that in the spectral domain additional lower (red) frequencies are produced. The opposite holds for the trailing edge of the pulse, where additional higher (blue) frequencies are generated. Due to the creation of additional spectral components both at the red and the blue side of the spectrum, the spectrum is broadened, which leads to the ability to reduce the pulse duration to a shorter Fourier limit. The effect is termed self-phase modulation because the laser pulse modifies its temporal phase itself due to the intensity- and thus time-dependent refractive index of the medium,

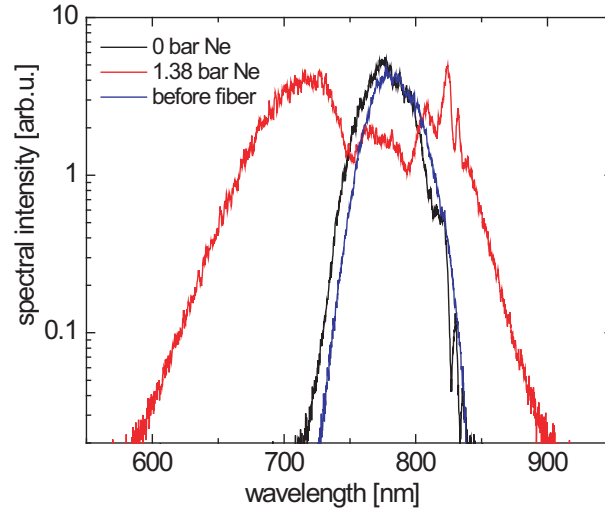


Figure 2.7: Spectral broadening by self-phase modulation in the hollow fiber. Measured laser spectra recorded before (blue line) and after the hollow fiber without (black line) and with 1.38 bar neon (red line).

while the temporal amplitude of the pulse is not affected [4]. To reach the Fourier-limited pulse duration the pulse has to be compressed after the SPM by compensating the non-flat temporal phase accumulated by the dispersion (see the next section) and the SPM.

SPM can be applied for spectral broadening for example in hollow-core waveguides filled with a noble gas [84]. In our experimental setup, we focus the laser beam, for this purpose, with a lens into a roughly 70 cm long hollow-core fiber filled with neon at a pressure of up to 1.5 bar. SPM takes place due to the high laser intensity. The refractive index is not only modulated temporally as described before, but also spatially due to the increase of the intensity towards the spatial center of the beam. This leads to an enhanced focusing of the laser beam and thus to an even higher intensity after the propagation of a few centimeters in the hollow-core fiber. The high intensity induces a weakly ionized plasma by multi-photon ionization, which starts usually at intensities of $\sim 10^{13}$ W/cm² in gases [85]. As a result the plasma defocuses the beam again and thereby reduces the intensity after another few centimeters, which starts the process again. The focusing and defocusing sections take turn several times within the hollow fiber. A filament is generated with the multi-photon ionization acting as a regulating mechanism [85]. A review of filamentation induced by intense femtosecond laser pulses and its spectral effects is given in Ref. [86]. Fig. 2.7 shows a typical laser spectrum before and after the hollow fiber, unfilled and filled with 1.38 bar neon. The spectral broadening reduces the Fourier-transform limited pulse duration from ~ 20 fs to ~ 6 fs. A typical throughput of the optical power through the hollow fiber is about 65%.

The generation of new frequencies either on the blue (+) or the red (-) side of the spectrum can be understood as result of the addition of two frequencies and the subtraction of a third frequency, where these three frequencies ω_1 to ω_3 must belong to the fundamental spectrum:

$$\text{self - phase modulation : } \hbar(\omega_1) \pm (\hbar(\omega_2) - \hbar(\omega_3)) \rightarrow \hbar(\omega_1 \pm (\omega_2 - \omega_3)). \quad (2.53)$$

Besides the spectral broadening, a blue-shift of the spectrum can be observed. The center of mass wavelength is shifted from 779 nm (unfilled fiber) or 784 nm (before the fiber) to 749 nm (fiber filled with 1.38 bar neon) in the measured spectra presented in Fig. 2.7. The intensity-dependent blue shift is caused mainly by optical-field induced ionization [87].

2.6.3 Dispersion Compensation

2.6.3.1 Basics

In a medium different frequencies of the transmitted light travel with different velocities and thus accumulate a different spectral phases $\phi(\omega)$. The effect is known as dispersion and is now discussed in more detail. We consider plane waves of a laser pulse with the spectral amplitude $A(\omega)$ propagating in z -direction through a medium with a frequency-dependent refractive index $n(\omega)$:

$$\tilde{E}(\omega, z) = \tilde{A}(\omega) \cdot \exp[i(\omega t - k(\omega)z)]. \quad (2.54)$$

We identify the spectral phase of this field by

$$\phi(\omega) = \omega t - k(\omega)z + \phi(\omega)|_{t=0, z=0}. \quad (2.55)$$

The frequency-dependent wave-vector depends on the refractive index:

$$k(\omega) = \frac{\omega}{c} \cdot n(\omega). \quad (2.56)$$

We see that a frequency-dependent refractive index adds contributions to the spectral phase that are nonlinear in ω . The spectral phase is changed by the propagation by

$$\Delta\phi(\omega) = \omega t - k(\omega)z, \quad (2.57)$$

while the spectral amplitude and the laser spectrum of course stay the same. In the following we decompose the change of the spectral phase $\Delta\phi(\omega)$ as a Taylor series of ω and explain how the individual orders j effect the pulse shape in time:

$$\Delta\phi(\omega) = \sum_{j=0}^{\infty} \frac{b_j}{j!} \omega^j, \quad (2.58)$$

with the coefficients

$$b_j = \frac{d^j}{d\omega^j} k(\omega) = \frac{d^j}{d\omega^j} \Delta\phi(\omega). \quad (2.59)$$

The zeroth order b_0 changes the absolute spectral phase ϕ_0 as a function of z . This means the CEP of the pulse changes by the propagation, while the pulse envelope stays the same:

$$b_0 = -\frac{z}{c} \omega n(\omega). \quad (2.60)$$

The next three coefficients read:

$$b_1 = -\frac{z}{c} \left(\omega \frac{d}{d\omega} n(\omega) + n(\omega) \right), \quad (2.61)$$

$$b_2 = -\frac{z}{c} \left(\omega \frac{d^2}{d\omega^2} n(\omega) + 2 \frac{d}{d\omega} n(\omega) \right), \quad (2.62)$$

$$b_3 = -\frac{z}{c} \left(\omega \frac{d^3}{d\omega^3} n(\omega) + 3 \frac{d^2}{d\omega^2} n(\omega) \right). \quad (2.63)$$

The first order coefficient b_1 corresponds to a time delay $-\tau$, by which the whole pulse is shifted in time, but still retaining its pulse shape. This can be seen by considering the group velocity, given by

$$v_g(\omega) = \left. \frac{d\omega(k)}{dk} \right|_{k=k(\omega)} = \left(\frac{dk(\omega)}{d\omega} \right)^{-1}. \quad (2.64)$$

With v_g at hand b_1 simplifies to:

$$b_1 = -\frac{z}{v_g(\omega)} = -\tau. \quad (2.65)$$

Therefore b_1 is also called the group delay (GD). The second coefficient b_2 is the group-delay dispersion (GDD). It means that the spectral components build up a now frequency-dependent $GD(\omega)$, which is linear in ω . A positive GDD is introduced by positive material dispersion, for instance in glass or air, and means that the low (red) spectral components travel before the high (blue) frequencies. The third coefficient b_3 is the third-order dispersion (TOD). It describes that the $GD(\omega)$, which the different spectral components experience, is not linear, but quadratic with the frequency ω . The shortest pulses are obtained for a "flat" spectral phase, which means that all nonlinear orders vanish ($b_j = 0$ for $j > 1$) and all spectral components arrive at the same time.

2.6.3.2 Experimental Realization

In our experimental setup the laser pulses experience positive material dispersion by the propagation in air and fused silica glass. One meter of air causes at 800 nm a GDD of $20.05 \pm 0.05 \text{ fs}^2$ and a TOD of $11.8 \pm 0.2 \text{ fs}^3$ [88], while 1 mm of fused silica at 750 nm introduces a GDD of 40.3 fs^2 and a TOD of 25.99 fs^3 [89].

There are several techniques available to compensate for the dispersion. The idea is to add to a dispersion-introduced spectral phase $\phi(\omega)_{dis.}$ an additional spectral phase $\phi(\omega)_{comp.}$ with opposite coefficients $b_{j,comp.} = -b_{j,disp.}$ for $j > 1$ in a way that the resulting phase $\phi(\omega)_{total} = \phi(\omega)_{dis.} + \phi(\omega)_{comp.}$ is only linear in ω and the pulse duration consequently Fourier-transform limited. For this purpose, the different frequencies have to travel different path lengths. For perfect dispersion compensation the necessary path-length difference would have to be

$$\Delta z(\omega) = \phi(\omega)_{comp.} \frac{c}{\omega \cdot n(\omega)}. \quad (2.66)$$

Commonly pairs of prisms or gratings are utilized to introduce a negative GDD [90, 91]. In our setup a pair of prisms is part of the compressor in the Femtopower laser system as manufactured by the company FEMTOLASERS Produktions GmbH (see section 2.6.1).



Figure 2.8: Customized chirped-mirror compressor placed after the hollow fiber.

Another technique are dispersive multilayer mirrors, shortly called chirped mirrors [92]. They are coated with many layers of increasing thickness consisting of alternating low and high-index dielectrics. As a consequence, the classical turning points of the laser light depend on the spectral frequency ω . A lower (red) frequency ω_1 penetrates deeper into the chirped mirror than a higher (blue) frequency ω_2 , leading to a group-delay difference ΔGD_{CM} , and thus a negative group delay dispersion

$$GDD_{CM} \approx \frac{\Delta GD_{CM}}{\omega_2 - \omega_1}, \quad (2.67)$$

which can compensate for a positive material dispersion e.g. produced by glass or air. Usually matched pairs of chirped mirrors are applied to compensate spectral ripples in the $GDD_{CM}(\omega)$ function. The frequency-dependent $GDD(\omega)$ can be flattened by using a pair of chirped mirrors with ripples with opposite phases [93]. An advantage of chirped mirrors is that the total $GDD_{all\ CM}(\omega)$ of all chirped mirrors can be customized to the total dispersion in the setup in a way that also higher orders of dispersion b_j like the TOD are accounted for and can be compensated. This is favorable in comparison to the prisms- or grating-based dispersion compensation, where the shape of the relative $GD(\omega)$ is restricted by the geometry. Chirped mirrors have been presented in the visible (VIS) and near infrared (NIR) with spectral bandwidths up to 1.5 octaves today, allowing a compression of the pulse down to a length of sub-3 fs, which is only little more than one full laser cycle [94]. A review of chirped mirror technology is given in Ref. [93].

In our setup we use a customized chirped-mirror compressor to compensate for the dispersion caused by ~ 5.0 m of air and ~ 5.6 mm of fused silica in the beam path between the hollow fiber and the HHG experiment. A second customized chirped-mirror compressor compensates the dispersion accumulated in a pulse-shaper setup (see chapter 5), to which the beam can be optionally sent before HHG.

2.6.4 Phase Stabilization

Before 2000, it was not possible to stabilize the absolute phase of an ultrashort laser pulse, expressed by the carrier-envelope phase (CEP) ϕ_0 as defined in Eq. 2.5 [95]. The CEP equals the momentary temporal phase of the electric field at the peak of the envelope (see

section 3.1) and its stabilization means that ϕ_0 does not vary from pulse to pulse. In this section the technique of the CEP stabilization and its realization in our setup is described.

The basic principle is that the mode-locked pulse train in the oscillator exhibits a frequency comb in the spectral domain [95]. A frequency comb consists of very narrow and completely equidistant spectral lines. The spacing of these lines is given by the repetition rate f_{rep} , which is in the MHz-range, so that the spectral positions of the n th modes reads:

$$f_n = n f_{rep} + \delta. \quad (2.68)$$

Let us imagine what consequences a stabilization of this comb would have for the shape of the pulses in the time domain. The Fourier transformation into the time domain reveals a pulse train with a pulse spacing of $1/f_{rep}$ and a pulse duration determined by the spectral bandwidth. The constant δ in the spectral domain represents a linear phase in time: $2\pi\delta t$. If δ is a fraction $1/m$ of f_{rep} then the linear spectral phase is $\phi(t) = \frac{2\pi \cdot m}{f_{rep}}$, which means that every m th pulse has the same phase (CEP) modulo 2π . Thus the CEP difference between two subsequent pulses is given by

$$\Delta\phi_0 = \frac{2\pi}{m} = \frac{2\pi \cdot \delta}{f_{rep}}. \quad (2.69)$$

Consequently two tasks have to be solved for CEP stabilization. Firstly, the comb has to be stabilized, which means a stabilization of δ , and secondly every m th pulse (or multiple) has to be selected for amplification. CEP-stabilized laser systems like ours are nowadays commercially available. The first task is realized by broadening the spectrum of the oscillator to more than one octave by SPM or DFG and overlapping a part of the blue side of the spectrum with the frequency-doubled spectrum generated by second harmonic (SH) generation. The frequency-doubled comb has the frequency offset 2δ , its difference to the fundamental comb thus equals δ , which leads to a beating of the two subfields in time with the frequency δ when the interference region is spectrally selected. The resulting beat note is recorded with a photo diode and used in our setup for feedback control of δ . This is realized by precisely modulating the pump laser intensity with an acousto-optical modulator (AOM), which in turn tunes δ . The feedback control is set to the condition $\delta = f_{rep}/4$ so that every fourth oscillator pulse has the same CEP value and is selected for amplification by an electro-optical Pockel's cell.

This kind of stabilization does not yet correct for long-term drifts of the CEP caused by thermal effects and drifts of the beams through the compressor. To account for this a commercial f-to-2f interferometer (from Menlo Systems GmbH) is employed. A low-intensity replica of the laser pulse after the compressor is spectrally broadened to more than one octave in a beta-barium borate (BBO) crystal and then used for SH generation. The interference signal of the frequency doubled and fundamental pulse is recorded with a compact Czerny-Turner spectrometer (Thorlabs SP1-USB) and the interference pattern in the overlap region of both pulses is then analyzed by means of complex Fourier filtering. The relative CEP value arises from the spectral phase of the interference pattern. This computed value is used as a feedback signal to adapt the amount of glass in the beam path. For this purpose the insertion of a prism is piezoelectrically corrected in the pulse stretcher, which in turn controls the CEP. The temporal short and long-term CEP stability

of this method is analyzed in Refs. [3, 96]. The references contain also a further description of the experimental implementation of the feedback-controlled CEP stabilization in the setup, which includes an optional second f-2f spectrometer for CEP determination placed after the hollow fiber. With current technology, the CEP in a train of few-cycle laser pulses, produced by a Ti:sapphire oscillator and compressed to a length of 6 fs, can be stabilized within a precision of $0.016 \times 2\pi$ rad, corresponding to a precision in time of 44 as [97].

2.6.5 Laser Pulse Measurement

In order to measure an ultrashort event like a laser pulse, regardless of whether only its pulse duration or the complete time-dependent real electric field, one needs a sampling process which is at least as short as the event itself. Otherwise the measured temporal structure would be smeared out or even not be detected at all. For ultrashort laser pulses there is typically nothing shorter available as the pulses themselves; thus they are applied as a sampling method themselves. A brief overview over such self-referencing techniques is given in this section, starting with the autocorrelation technique. A more extensive review of different ultrashort pulse characterization and -control techniques can be found in the Refs. [98, 28].

For the autocorrelation, the laser pulse is split up into two identical copies, which are recombined after in one path a variable and controlled time delay τ was applied to one of them. This can be experimentally realized with a Michelson- or Mach-Zehnder interferometer, in which one arm has a variable path length. The electric field of the recombined pulse then reads:

$$E_{rec}(t, \tau) = E(t) + E(t - \tau), \quad (2.70)$$

with τ given by the path difference divided by c . To perform an autocorrelation, a signal which contains the product $E(t) \cdot E(t - \tau)$ is required. This can be achieved only by a nonlinear process, the response of which includes higher orders of the intensity $E_{rec}(t - \tau)$. The easiest process of this kind is the second harmonic generation, at which the doubled frequency $2\omega_c$ is produced with an electric field $\propto E_{rec}(t, \tau)^2$. Thus we can write for the electric field of the produced SH:

$$E_{SH}(t, \tau) \propto E_{rec}(t, \tau)^2 = E(t)^2 + E(t - \tau)^2 + 2E(t)E(t - \tau). \quad (2.71)$$

After spectrally filtering out the fundamental light at ω_c , we measure the photo current, which is proportional to the time-averaged SH intensity and dependent on the time delay:

$$J_{photo}(\tau) \propto \int_{-\infty}^{\infty} I_{SH}(t, \tau) dt \propto \int_{-\infty}^{\infty} |E_{SH}(t - \tau)|^2 dt = \int_{-\infty}^{\infty} E_{SH}(t, \tau) E_{SH}^*(t, \tau) dt. \quad (2.72)$$

As a function of τ we obtain an interference pattern with an amplitude which is determined by the overlap of the two pulse replicas. Out of this signal the pulse duration t_{FWHM} can be determined. Yet the exact shape of the electric field or its temporal phase $\phi(t)$ cannot be retrieved by the autocorrelation method. Fig. 2.9 shows a measured autocorrelation signal and the corresponding laser spectrum for the laser pulse in the ex-

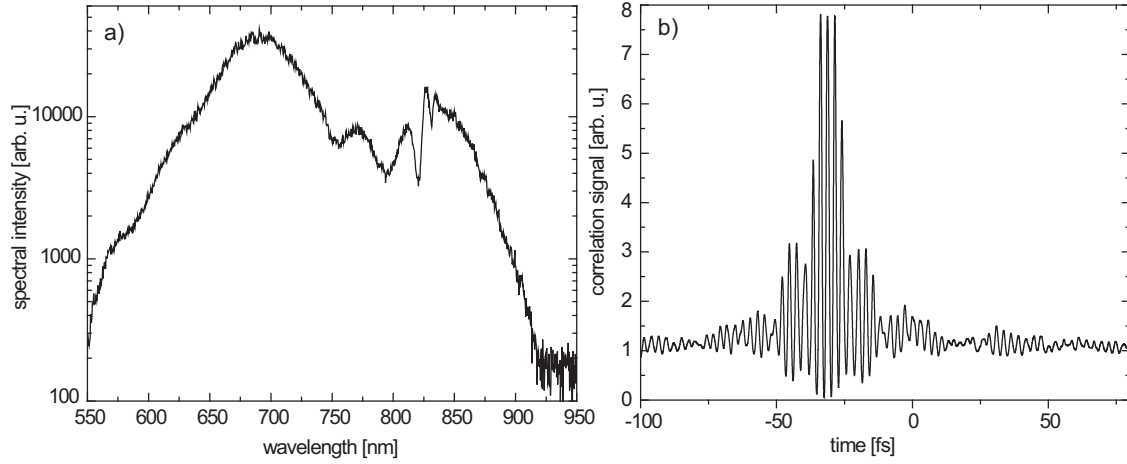


Figure 2.9: Autocorrelation measurement for the determination of the pulse duration. The autocorrelation trace (b) implies a pulse duration of $t_{FWHM} = 6.4$ fs, which is close to the Fourier-transform limited pulse duration $t_{FT-limit} = 5.3$ fs calculated from the measured laser spectrum shown in (a).

periment after the hollow fiber, the chirped-mirror compressors and the pulse shaper (described in section 5.2). The determined pulse duration is $t_{FWHM} = 6.4$ fs. The laser spectrum would support a Fourier-transform limited pulse of 5.3 fs. The close agreement of the measured pulse duration in comparison to the bandwidth-limited value illustrates an excellent dispersion-compensation ability in the setup, where in total the dispersion introduced by about 32 mm fused silica glass and ~ 10 m air after the hollow fiber has been removed. Without chirp mirrors the pulse duration in this case is calculated to be ~ 1 ps.

If the beam intensity is too low to produce a sufficient second harmonic signal for autocorrelation, the pulse duration can be determined with the help of a stronger additional laser field, which is superposed with a variable time delay τ . For this technique, termed cross-correlation, the combined field is applied for the second-order nonlinear process now termed sum-frequency generation, instead of second-harmonic generation, because the frequencies of the weak and the strong laser field are not necessarily the same.

This yields a photo current of the detected sum-frequency generated light proportional to

$$J_{photo,nc} \propto \int_{-\infty}^{\infty} I(t)I_s(t - \tau)dt, \quad (2.73)$$

with I_s being the intensity of the strong reference beam.

Both at autocorrelation and crosscorrelation the correlation signal gives only information about the temporal energy distribution in the pulse and does therefore not reveal the full information (amplitude and phase) encoded in the complex function $\tilde{E}(t)$. Even the intensity profile $I(t)$ cannot be retrieved directly. For a Gaussian-shaped laser pulse the connection between the width (FWHM) of the correlation signal τ_{cor} and pulse duration τ_{pulse} defined by FWHM of $I(t)$ is given by

$$\frac{\tau_{cor}}{\tau_{pulse}} = \sqrt{2}. \quad (2.74)$$

This holds true only for the second-order autocorrelation, but not for crosscorrelations, third- or higher-order autocorrelations.

Other techniques for laser-pulse measurement are frequency-resolved optical gating (FROG) [99] or spectral-phase interferometry for direct electric field reconstruction (SPIDER) [100]. Both methods make use of the spectral information which is encoded in an interference signal.

Another approach to retrieve the waveform of femtosecond laser pulses is the streaking technique. The principle goes back to streaking cameras, where the acceleration of electrons is used to map the time information of a fast changing electric field or laser pulse to a momentum distribution which is encoded in the spatial distribution of the electrons after the propagation through a drift distance and can be detected for example by a multi-channel plate detector [101, 102]. In the advanced method an isolated attosecond pulse (IAP) is used to ionize atoms within the very confined (subcycle) temporal range of the IAP [53, 103]. The freed electrons are then accelerated in the electric field of a CEP-stabilized laser pulse and gain its vector potential at the time of ionization as the final momentum after the laser pulse has passed. This momentum distribution is then measured as a function of the time delay between the IAP and laser field. Thus the electric field of the ultrashort laser pulse can be determined as the derivative of the vector potential encoded in the streaking trace.

2.7 The Attosecond Beamline

High-order harmonic generation was performed in a newly designed and set up attosecond beamline, which is described in this section (see Ref. [3] for further details of the setup and the alignment). Extreme ultraviolet light exhibits a strong absorption in atmospheric-pressure air, but the transmission through 1 m air in the spectral range 25-125 eV is already >93% at a pressure of 10^{-3} mbar. Thus the setup must be placed in vacuum, but the vacuum requirements are not very strict for the HHG experiments (the pressure should be below 10^{-3} mbar). Fig. 2.10 gives an overview over the attosecond beamline. For HHG a stainless-steel cell of 2 mm inner diameter is placed in the first vacuum chamber and filled with argon as generation medium at a variable gas pressure. The laser beam is focused into this cell with a spherical focusing mirror outside the vacuum chamber with a focal length of $f = 50$ cm. The generation cell has two holes of 100 μm diameter to guide the beam. The effective conversion length is 2.5 to 3 mm. For its calculation the thickness of the claddings of each 0.2 mm around the holes and the gas flow out of the cell along the beam direction was taken into account. The produced XUV light travels inside the IR beam through the further setup, with an angular divergence that is much lower than the divergence of the IR light. Turbo molecular pumps keep the gas pressure below 10^{-3} mbar at HHG operation in the first chamber (2000 l/s pumping speed) and below 10^{-5} mbar in the other chambers.

The second large vacuum chamber contains an interferometric split-mirror setup, in which a time delay between the IR und XUV pulses can be introduced with very high (attosecond) precision. For this purpose a gold-coated 2 mm high and 10 mm broad mirror is

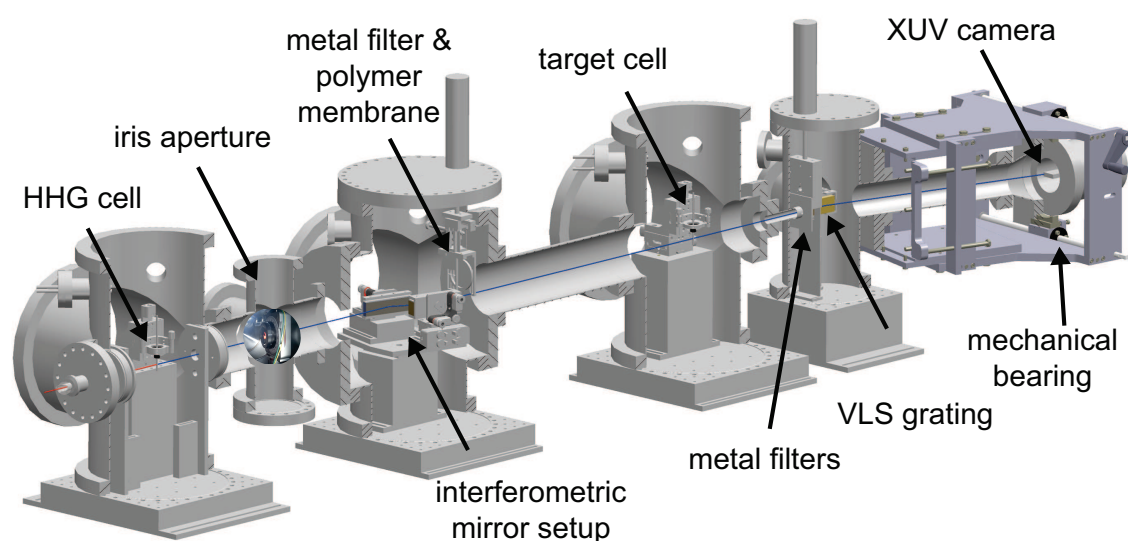


Figure 2.10: Setup of the attosecond beamline (from [3]). In the first vacuum chamber the attosecond pulses are produced in an argon-filled cell. A special split-mirror setup and a target cell allow for interferometric experiments with time-delayed IR and XUV pulses. Finally, the high harmonics are recorded with a high-resolution flat-field XUV spectrometer (see Fig. 2.12).

placed coplanarly within and translated piezo-electrically with respect to a 26 mm high and 100 mm wide silver-coated outer mirror. A root-mean-square (RMS) surface flatness below 0.5 nm allows for a high reflectivity and conservation of the coherence. While the XUV light is reflected only by the inner mirror due to its lower divergence, the outer mirror guides the IR beam. The complete separation of the IR and XUV is secured by a concentrically mounted metal filter and polymer membranes. Holes in the membrane restrict the XUV beam to a position where selectively mounted aluminum or zirconium filters remove the IR and low-order harmonics. A toroidal mirror focuses both beams into a target cell, which is an exact copy of the generation cell and placed in the third big vacuum chamber. For more details on the alignment of the toroidal mirror see Ref. [104]. The inclusion of the interferometric setup in the beamline allows to introduce and measure electron dynamics in atoms and molecules on attosecond time scales. It was not applied in the experiments that are subject of this work, but could be combined in future experiments. With this setup, the correlated electron dynamics of doubly-excited helium was measured, revealing among other results a 1-fs periodic quantum beating of a two-electron wavepacket and the complete inversion of Fano absorption line shapes [105, 3].

In the spectrometer chamber, two additional 200 nm thick metal filter foils remove VIS- and IR stray light and low-order harmonics. A movable mounting of the filters allows the selection of either aluminum or zirconium filters without opening the chamber. A grazing-incidence variable-line-spacing (VLS) diffraction grating with an average groove density of 1200 mm^{-1} spectrally resolves the XUV light into the camera plane. The spectra are recorded in first diffraction order with a back-side-illuminated thermo-electrically cooled charge-coupled device (CCD) camera, the sensitivity of which is optimized for the XUV range and combines a high dynamic range with a low thermal and readout noise [107]. The camera is mounted highly stable and moveable parallelly to the camera plane in a manner that a spectral range from ~ 20 to 120 eV can be precisely selected. Out of the

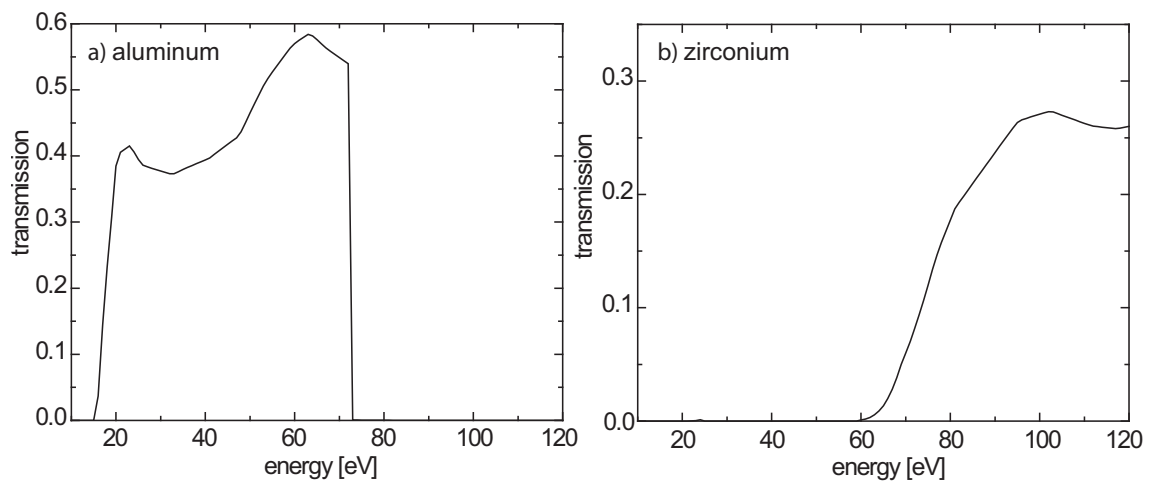


Figure 2.11: Spectral removal of stray light and low-order harmonics by metal foils. Simulated transmission through $0.4 \mu\text{m}$ aluminum (a) and $0.4 \mu\text{m}$ zirconium (b) [106].

geometry and pixel size ($20 \times 20 \mu\text{m}^2$) a spectral resolution of $\sim 27 \text{ meV}$ at 60 eV photon energy is estimated, while a comparison with a line convoluted by a Gaussian function yielded a resolution of $\sim 47 \text{ meV}$ [3].

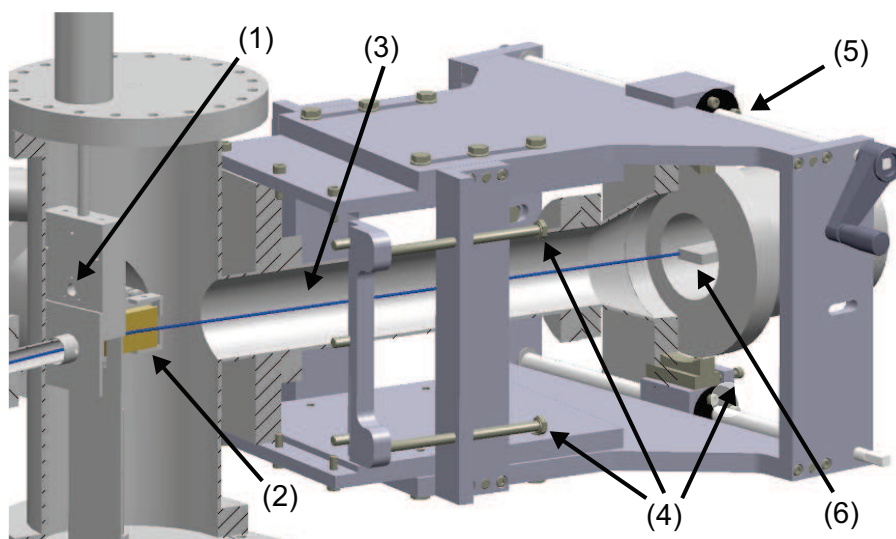


Figure 2.12: Setup of the customized high-resolution XUV spectrometer (from [3]). Pairs of metal filters (1) are applied to remove visible stray light and low-order harmonics. (2) Variable-line-space (VLS) grating, (3) flexible membrane bellow, (4) adjustment screws for coarse and fine positioning, (5) bearing for the high-precision selection of the spectral range and (6) backside-illuminated CCD chip of the cooled XUV camera.

Chapter 3

Coherent Control of High-order Harmonic Generation by the Carrier-envelope Phase

In this chapter the effect of the carrier-envelope phase of the driving laser field on high-harmonic generation is investigated. It is analyzed how this single variable can have a significant impact on the high-harmonic spectra, what demonstrates its ability for control. This controllability will then be further extended in the following chapters. The controllability by means of the CEP is not restricted to HHG but considered to be suitable for other experiments as well where electron dynamics is induced by a strong few-cycle laser pulse. A few examples of such experiments are given. Further, a method is presented which shows that—by applying CEP control and analyzing the high-harmonic spectra—one can learn something about the process of HHG and attosecond pulse generation. In particular, we explore the relative phases of the generated attosecond pulses, which cannot be retrieved from a single high-harmonic spectrum alone.

The chapter is structured as follows: At first the dependence of the high harmonics from the CEP is studied in section 3.1. Section 3.2 illustrates more generally the power of the CEP to steer atomic and molecular electron dynamics. Finally a two-dimensional interferometric method which utilizes the CEP dependence of the measured high harmonics is introduced and applied in section 3.3 to reveal the relative phases between the generated attosecond pulses.

3.1 Carrier-envelope Phase Control of HHG

High-harmonic generation is strongly dependent on the exact shape of the electric field $Re(E(t))$, since it is the instantaneous electric field strength, which determines the ionization rate in the first step of the HHG model [22, 23] and the vector potential

$$A(t_{rec.}) = -\frac{e}{m_e} \int_{-\infty}^{t_{rec.}} E(t') dt', \quad (3.1)$$

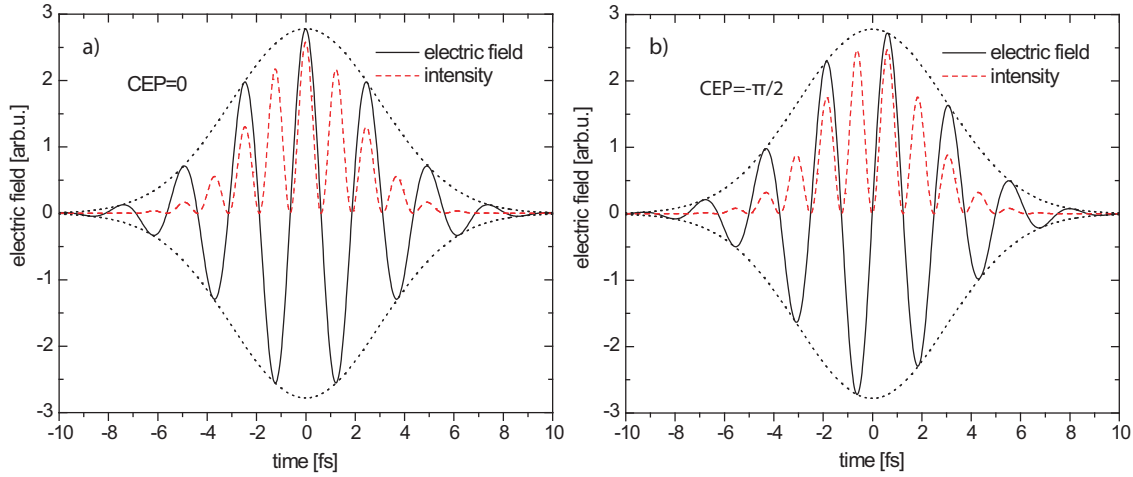


Figure 3.1: Illustration of the carrier-envelope phase (CEP, ϕ_0). Electric field (solid line), instantaneous intensity (dashed line), and envelope (dots) of a Gaussian-shaped laser pulse with a 5 fs duration (FWHM) for $\phi_0 = 0$ (a) and $\phi_0 = -\pi/2$ (b). The CEP $\phi_0 = 0$ yields a cosine-like electric field with the carrier-peak at the envelope maximum, while $\phi_0 = -\pi/2$ gives a sine-like pulse with a carrier which is shifted in time by $\frac{\phi_0}{\omega_0}$.

which defines the kinetic energy of the electrons at the recombination time t_{rec} . The ability to stabilize and set the phase between the carrier of the electric field and the pulse envelope (carrier-envelope phase, CEP) [108, 109, 110] thus delivers a direct control tool for HHG. In 2001, a method was found to measure the absolute CEP value of a few-cycle laser pulse. It was proposed to record and compare high-energy spectra of above-threshold ionized electrons for both sides along the direction of the laser polarization, the relative contributions of which precisely depend on the absolute CEP [111]. The CEP effects of above-threshold ionization in argon, xenon and krypton has also been investigated with few-cycle laser pulses fully angularly resolved by Kling *et al.* [112]. The advancement of this method for single-shot CEP determination overcomes the need for phase stabilization which had limited the precision so far [113]. A review of attosecond-resolved measurements and CEP determination by above-threshold ionization (ATI) is given in Ref. [114]. An alternative method for the absolute CEP determination is the down-conversion of the pulse to the terahertz-regime by plasma generation in air. An induced spatial charge asymmetry is found, which reveals the absolute CEP by the analysis of the terahertz emission [115].

Baltuška *et al.* demonstrated experimentally that the CEP has a large effect on the HHG spectrum, for example a periodic energy shift of the harmonic lines as a function of the CEP enables to determine the relative CEP. They explained this effect by the controlled evolution of the electron wave packet during HHG by the precisely controlled and phase-stabilized electric driver field [116]. The CEP-dependent energy shift of the high-harmonics peaks has also been observed by the first single-shot measurements of HHG and attributed to the nonadiabatic single-atom response [117]. Sansone *et al.* then studied theoretically the influence of the CEP on the short and long electron trajectories. While the short trajectories can be controlled by the CEP only for few-cycle laser pulses, the long trajectories can be influenced also by applying multiple-cycle pulses [118]. More-

over it was observed that center photon energy of an isolated attosecond pulse which is generated by ionization gating can be tuned by the CEP [119].

In general, the CEP effects are the more pronounced, the shorter the driver pulse is. We consider Gaussian-shaped pulses in intensity. As can be seen in Fig. 3.1 sine-like pulses ($\phi_0 = -\frac{\pi}{2}$) have two peaks with equal field intensity $|Re[E(t)]|^2$ while cosine-like pulse ($\phi_0 = 0$) have one strongest peak of the electric field and two next-stronger peaks. Hereby, the intensity contrast between the strongest and subsequent peak is larger the shorter the driver pulse is. Hence also the CEP effects in HHG are more pronounced for few-cycle or even sub-cycle pulses than for multiple-cycle pulses. Since the vector potential is generally different for every half-cycle at which the electron trajectory starts (let us consider for a moment only the short trajectories) the harmonic cut-off energy is different for every attosecond pulse which is produced. The total spectrum then results from a coherent addition of all half-cycle contributions. Each half-cycle contribution thereby strongly depends on the CEP. Haworth *et al.* [120] showed experimentally that the individual cutoff energies of the half-cycles can be identified in the harmonic spectrum and the CEP can be determined precisely with an accuracy of 20 as for their 8.5 fs long driver pulse. Chipperfield *et al.* demonstrated that by choosing the right focus conditions the cut-off harmonics of each half-cycle can be selected by phase matching while the plateau harmonics are suppressed for each half cycle [121]. The energies of these macroscopic half-cycle cut-offs then yield a "fingerprint" of the driving laser pulse. The interference of spectrally overlapping half-cycle cutoffs leads to modulations in the spectrum, e.g. possibly but not necessarily to the two-omega spacing of the odd harmonics, but the half-cycle cutoff energies can still be identified by a thought envelope or determined more precisely if a low-pass filter is applied to the spectrum. By plotting the harmonic spectrum as a function of the CEP one can see how the cut-off energies of the individual half cycles increase at first as the peak of the electric field comes closer to the maximum of the envelope, then saturates for cosine-like shaped pulses (at $\phi_0 = 0$ and $\phi_0 = \pi$) and then would go down, if phase matching is still fulfilled. Jullien *et al.* [81] proposed this method for the identification of the temporal phase-matching gate. They demonstrated that the wavelength-tunable isolated attosecond pulse in their CEP-controlled experiment has been phase-matched on the leading edge of the few-cycle driver pulse. This produces half-cycle-cutoffs which increase in energy when the CEP is scanned.

Figure 3.2 shows high-order harmonics generated in neon as a function of the CEP. The measurements were performed in our experimental setup with a backing pressure of ~ 100 mbar and two $200 \mu\text{m}$ zirconium foils to remove the low-order harmonics and the IR light. The conversion cell was placed shortly after the focus in (a) and shortly before the focus in (b). The half-cycle cutoffs as regions with the highest spectral intensities are clearly visible in b) and tuned periodically by the CEP from about 80 eV to 92 eV. As described above the CEP dependence of the half-cycle cutoff energies resolves the part of the driver-pulse envelope where the attosecond pulses are emitted, which is the leading edge in our case. The 2ω -modulation in energy is more pronounced in b) compared to a). A possible explanation could be that more attosecond pulses are generated before the focus, while the number of contributing trajectories and thus attosecond pulses is reduced after the focus due to modified phase-matching conditions. Moreover, we clearly see in a) that the energy of the odd harmonics is tuned periodically by the CEP. This behavior will

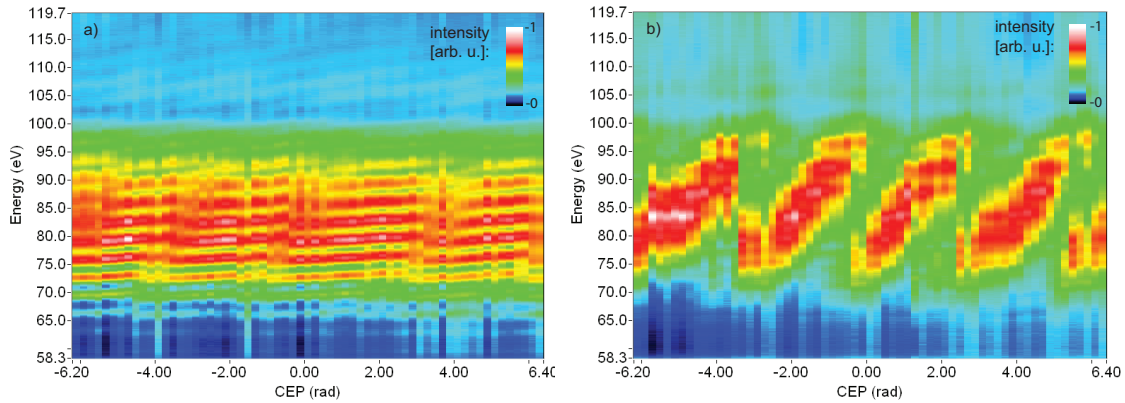


Figure 3.2: CEP-dependence of high-order harmonics and half-cycle cut-offs (experimental results). Spectra of high-order harmonics as a function of the CEP measured after (a) and before the focus (b). In both cases the energy of the harmonics is shifted by the CEP. This demonstrates the ability of the CEP to control electron dynamics on a time scale corresponding to a fraction of an optical cycle. In b) the high-harmonic spectra are composed of a coherent sum of CEP-dependent half-cycle emissions which peak at different energies depending on their individual cutoff energies. These so-called half-cycle cut-off (HCO) energies are clearly visible in the observed harmonic spectra. The CEP dependence of the HCO energies resolves the envelope of that part of the driving laser pulse where the attosecond pulses are emitted.

be further investigated in section 3.3. One goal behind this measurement was to demonstrate the ability of the newly set up attosecond beamline described in chapter 2 to perform pronounced CEP control with few-cycle laser pulses and to reproduce the findings in literature, before more enhanced control- and analysis schemes are introduced. The results are in good agreement with the literature [120, 81].

3.2 CEP-Control of Electron Dynamics

The CEP of few-cycle laser pulses has become a key tool for ultrafast control of quantum dynamics in the last years. For a review of quantum control see Refs. [50, 122] and of CEP-control and spectroscopy of attosecond electron dynamics see Refs. [123, 124]. Since the measurement and control of electron dynamics is one goal targeted by the generation of tailored attosecond pulses a short overview over a few recent achievements in the field of CEP control of electron dynamics (other than the electron dynamics involved in HHG) are reviewed. In 2006, Kling *et al.* showed that the localization of electrons at molecular dissociation can be controlled by the CEP by the example of molecular deuterium $D_2 \rightarrow D^+ + D + e^-$ [125]. They use a 5 fs long, intense, phase-stable laser pulse to ionize the molecule and to create a vibrational wave packet. Several pathways lead to the production of D^+ , the angular and energy distribution of which is measured by a technique called velocity-map imaging. A pronounced asymmetry in the angular distribution of the measured D^+ ions and thus also in the electron localization at the other ion, respectively, is observed and found to be controllable by the CEP. The ionization events are integrated over the D^+ -energy range from 3 to 8 eV, in which the fragments are mainly generated. In particular, it is possible to reverse the electron localization by changing the

CEP by π , which turns the electric field upside down. The underlying mechanism is the following: At first the D_2^+ ion is formed in its $1s\sigma_g^+$ ground state, secondly a recollision of the remaining second electron starts the dissociation of D_2^+ by transferring it to the repulsive $2p\sigma_u^+$ state. This event depends on the field polarization and thus the CEP. The superposition with the $1s\sigma_g^+$ state leads to an oscillation of the electron between the two ions. When the distance and thus the potential barrier between the ions gets too large, the electron is trapped and thus located on one of the two D^+ ions [112]. Similarly, also the dissociative ionization of carbon monoxide (CO) induced by a phase-stable, linearly polarized, 4-fs long laser pulse was measured, exhibiting as well a strong CEP dependence of the emission directions of the fragments C^+ and O^+ [126]. During the dissociation population is transferred between the excited states of CO^+ .

Fischer *et al.* [127] studied the electron localization of H_2^+ by a combination of pump-probe spectroscopy and CEP control. While the pump pulse creates a nuclear wave packet, the probe pulse starts the dissociation and localization of the single electron at one of the two aligned ions (left or right). The asymmetry parameter

$$A = \frac{N_{left} - N_{right}}{N_{left} + N_{right}} \quad (3.2)$$

is hereby controlled by both the time delay between the pump and the probe and the CEP of both phase-stabilized 6-fs long laser pulses. Here, N_{left} and N_{right} are the number of protons detected on the left/right side.

Not only atomic or molecular electron dynamics can be controlled by the CEP of the applied laser pulses. Beyond this, it was shown that the emission of electrons from a nanoscale metal tip exhibits strong energy-dependent modulations with the CEP as well. Since the emission is controlled on the attosecond time scale, the finding gives an example that attosecond techniques applied in atoms or molecules can be transferred to solids [128]. Recently, Borot *et al.* focused a CEP-stabilized few-cycle laser pulse on a rotating glass surface with a peak intensity around 10^{18} W/cm² [129]. Collective electron motion in the laser-induced plasma is driven by the intense laser field and probed by the coherent XUV-light emission, which forms harmonics as known from HHG. The CEP dependence of these harmonics illustrates the ability to steer the attosecond electron dynamics in laser-driven dense-plasma experiments. As we have seen, the CEP control is a powerful tool to control the electron dynamics in various processes such as HHG, laser-induced ionization, dissociation and fragmentation. Besides the influence of the CEP on the temporal shape of the electric field, which drives these processes, exhibiting e.g. an up-down asymmetry, there is another approach to understand the ability of CEP control. It is described in Ref. [123] and linked to the control scheme of Brumer-Shapiro [130]. In general the control of a quantum-mechanical transition requires the coherent interference of multiple pathways leading to the same final state. In the case of population transfer by multi-photon absorption different pathways can be covered by a single octavebroad laser pulse so that the CEP governs the phase between these pathways and thus the transfer probability for example between bound states of atoms and molecules. The quantum interference of the different pathways to the same final energy level is also the mechanism behind the optimal control of molecular dynamics performed by closed-loop pulse shaping [131]. Taken together the variety of the discussed different electronic processes for which CEP control

can be applied indicates that microscopic HHG-control methods (such as the CEP control) are not limited in their applicability to the particular electron dynamics involved in HHG. Instead the HHG-control techniques which are based on the shaping of the electric driver field in different manners should be able to steer other kinds of electronic processes as well, given the electron dynamics evolves on a matching (femto- or attosecond) time scale.

3.3 Carrier-Envelope Phase Spectral Interferometry

3.3.1 Method and Numerical Results

In the following a spectroscopic method is presented how one can resolve information about the temporal structure of the attosecond pulses out of measured CEP-dependent high-harmonic spectra. We refer to the method as carrier-envelope spectral interferometry (CEPSI); it is described in detail including the numerical and experimental results in Refs. [132, 133, 3]. The harmonic spectra result from the interference of three attosecond pulses, which are spaced in time, defining two independent temporal distances τ_{12} and τ_{23} . The distance of the pulses 1 and 3 is then given by τ_{13} . The spectral interference is in analogy to the diffraction pattern of a triple slit. Important for the interference are the relative phases between the pulses. For a simulation we set the phases of the pulses 1 and 2 to $\Phi_{1,2} = 0$ and vary the phase $\Phi_3 = \varphi$ of pulse 3. We choose slightly asymmetric temporal spacings $\tau_{23} = 1.1\tau_{12}$. In the spectral domain, which is calculated by the Fourier transformation of the pulses in the temporal domain, the fastest modulation that we see has the periodicity of $\sim 1/\tau_{13}$. Due to the interference of two subsequent pulses every second of the peaks has comparable intensity, thus major and minor peaks spaced by $2/\tau_{13}$ are formed. Due to the spacing asymmetry the major peaks transit to minor peaks and reverse with the periodicity $\frac{1}{\tau_{12}-\tau_{23}}$. The spectral position of this transition depends on the relative phase φ and is marked with arrows in Fig. 3.3a). Fig. 3.3b) shows the spectrum of the three pulses as a function of φ from -2π to 2π . A second complex Fourier transformation of the spectra in b) with respect to the energy and as a function of φ is depicted in Fig. 3.3c). This makes the method two-dimensional, while in contrast to conventional 2D-spectroscopy [134] we now have with φ and the Fourier-time (which reveals the temporal separation of the attosecond pulses) dynamical quantities on both axes, instead of two spectral axes. The Fourier amplitude reveals the two spectral-modulation components with periodicities of τ_{13} , τ_{12} and τ_{23} with the broadening resulting from the variation of the relative phases between the attosecond pulses (their absolute duration cannot be measured by CEPSI). The last two Fourier components transform continuously into each other, but can be distinguished by their different Fourier phase behavior. The Fourier amplitude stays constant in the τ_{13} region, while the amplitude of the other components (at τ_{12} and τ_{23}) are modulated by φ . This means that here the 1ω -modulation is always present in the spectrum in contrast to the 2ω -modulation. The numerical results in Fig. 3.3 demonstrate that if we apply the Fourier transformation of a measured spectrum of attosecond pulses we can not only obtain the pulse number, but also the temporal separation of the pulses and the relative phase of each pair of pulses. As a requirement the harmonic spectrum

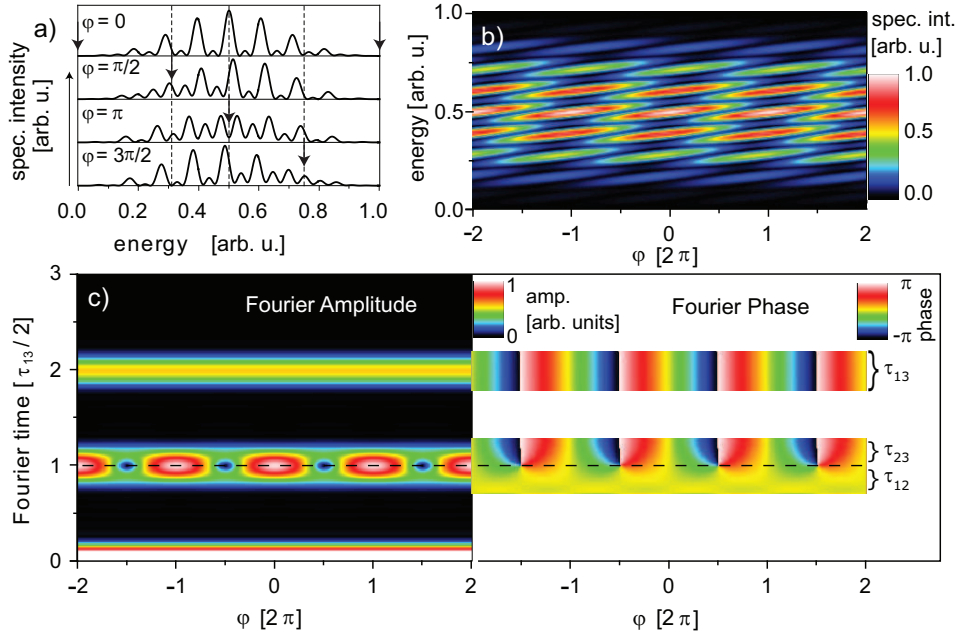


Figure 3.3: Simulation of phase-controlled spectral interference (from [133]). a) Spectrum generated by the interference of three pulses non-equidistantly spaced in time by $\tau_{23} = 1.1\tau_{12}$. The relative phase of the third pulse is varied $\Phi_3 = \varphi$ while the phases of the first two pulses are constant at $\Phi_1 = \Phi_2 = 0$. The arrows indicate the spectral positions where the alternating major and minor peaks swap their order. b) Spectra as in a) as a continuous function of the relative phase φ . c) Complex Fourier transformation of b) with respect to the energy. The three components of the spectral modulations can be identified which correspond to the temporal distance of each two pulses. The Fourier phase indicates the phase changes between the pairs of pulses.

must be recorded as a function of a dynamical parameter: the relative control phase φ , which is the CEP in our case.

3.3.2 Experimental Results

We now apply the CEP SI-method to analyze the experimentally obtained spectra. Here the stabilized CEP takes over the role of the relative phase control parameter φ . HHG was produced in neon at a backing pressure of ~ 100 mbar and at a peak intensity of $\sim 1 \times 10^{15}$ W/cm². The peak intensity was derived from the harmonic cut-off energy (see Eqs. 2.24 and 2.22). The conversion cell was located shortly after the laser focus to phase match preferentially the short trajectories [43]. Zirconium filters with a total thickness of $0.4 \mu\text{m}$ filtered out the low-order harmonics. Fig. 3.4a) shows the measured HHG spectrum as a function of the CEP. Again one observes a CEP-introduced energy variation of the odd harmonics, which are clearly visible over a spectral range of about 40 eV. The large covered energy range enables a high resolution in the Fourier time. Fig. 3.4b) presents the CEP-dependent Fourier amplitude and Fourier phase obtained as described above. The result is similar to the simulation in Fig. 3.3. We see that mainly three attosecond pulses produce the measured spectra for all values of the CEP. The Fourier phase of the first peak splits up into two time-delay regions τ_{12} and τ_{23} . One observes that the

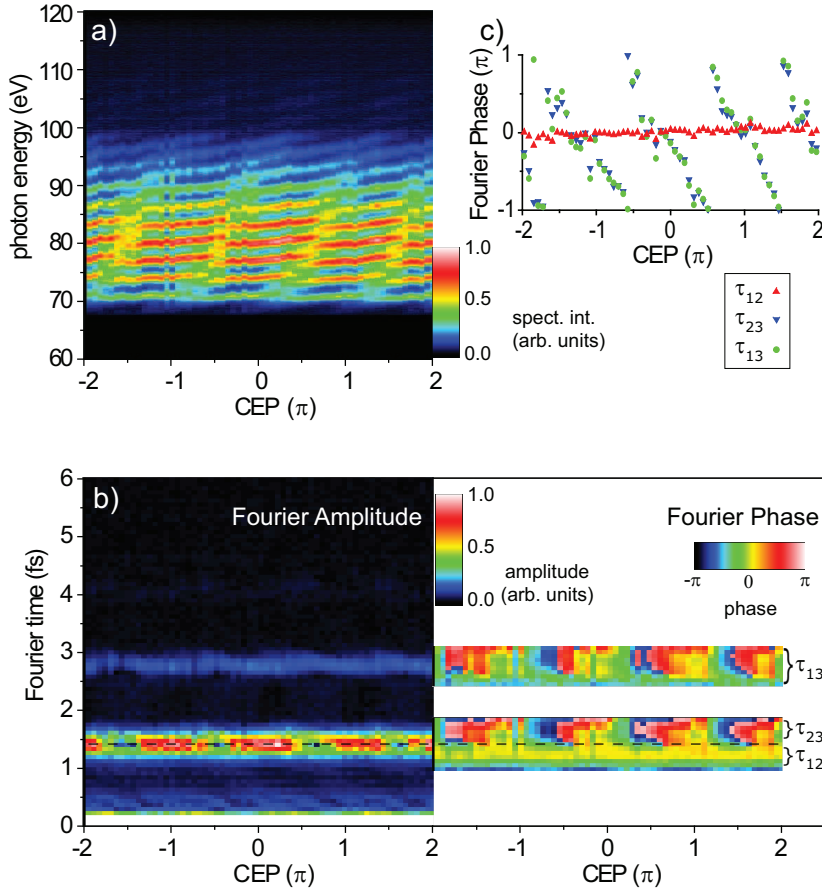


Figure 3.4: Carrier-envelope phase spectral interferometry (CEPSI): experimental results, from [133]. a) Measured high-order harmonics as a function of the CEP. b) Fourier transform of a), revealing the non-equidistant temporal spacing of three attosecond pulses. The phase between the first two attosecond pulses is not influenced by the CEP, while the relative phase between the third pulse and the others is fully modulated within 2π . c) The CEP modulates the phase between the two pairs of attosecond pulses which are displayed by the triangles (down, τ_{23}) and circles (τ_{13}) as given by the average over the marked temporal regions in b). In contrast, the phase between the pulses 1 and 2 (triangles, up, τ_{12}) is hardly influenced by the CEP.

phase between the attosecond pulses 1 and 2 is not altered by the CEP, while both phases between the pulses 2 and 3, and between the pulses 1 and 3 are changed by the CEP in the same way. These two relative phases are varied within full 2π , as can be seen in Fig. 3.4c), where the averaged Fourier phases are plotted as a function of the CEP for the three temporal regions marked in Fig. 3.4b). We think that the different temporal distances of the attosecond pulses are introduced by their different relative positions in the driver pulse. While the first pulse is produced close to the driver pulse center, the third pulse is generated on the trailing edge. This results in a different cut-off energy for the third electron trajectory, irregular attosecond pulse spacings $\tau_{23} > \tau_{12}$ and a CEP-induced modulation of τ_{13} of 54 ± 16 as [133]. The two-dimensional spectroscopy introduced here serves as a versatile detection method for the CEP control of HHG. It provides not only a trajectory-selective measurement of the electron dynamics involved in HHG, but offers also a spectroscopic technique to reveal these dynamics in the time domain with

a resolution in the low attosecond range and complementary information encoded in the Fourier amplitude and phase. We will apply this technique further in chapter 5 since it gives access to the relative phase between experimentally obtained attosecond pulses and even entire attosecond pulse trains.

3.4 Conclusion

In this chapter the carrier-envelope phase of the driving laser field was introduced as a control parameter the effect of which can be understood on the single-atom level. The power of this single control parameter was illustrated for the direct control of femtosecond electron dynamics induced by few-cycle laser pulses with variable CEP. The CEP as well influences high-harmonic generation in different manners; for instance the half-cycle cutoff energies of the individual electron trajectories are governed by the CEP of the driver pulse. This leads to an experimentally observed spectral tuning of the high harmonics with the CEP and a modulation of the spectral position with the highest harmonic intensities. Moreover, a new two-dimensional interferometric method (carrier-envelope phase spectral interferometry, CEP-SI) was presented [132]. For its application the high-harmonic spectrum has to be measured as a function of the CEP. Complex Fourier analysis then gives insight into the temporal structure of the produced attosecond pulses. The method enables to extract both the temporal distance and what is even more important the phase differences between each pair of attosecond pulses as a function of the CEP. Applying the method to the experimentally-obtained high harmonics which result from the interference of three attosecond pulses it was found that these attosecond pulses are unequally spaced in time. Moreover, the attosecond pulses show a different behavior of their pairwise relative phases when the CEP is tuned.

While the harmonic yield can be increased by optimizing the macroscopic phase matching of the contributions of many atoms, phase-matching considerations can be transferred to the microscopic control, where by shaping of the driver-field contributions of several trajectories for a single atom can be phase-matched. By means of this so-called intra-atomic phase matching particular harmonics can be selectively enhanced [135]. To perform such a sophisticated HHG control the driver-pulse shape has to be varied more comprehensively than possible with the CEP alone. One option is adaptive control which can be implemented with deformable mirrors or liquid-crystal displays (see appendix A and the references therein). The driver pulses (mostly multi-cycle pulses have been employed so far) are shaped in this case by controlling up to several hundreds degrees of freedoms in the spectral domain (spectral phases and/or amplitudes). While evolutionary algorithms deliver optimized pulses by closed-loop control, there are due to the complexity difficulties to recover the control mechanisms. Moreover, the investigation of subcycle-shaping effects and the direct control of single or few electron trajectories request rather a large laser bandwidth than hundreds of degrees of freedom. Another control option which prevents these limitations and delivers further even more remarkable features will be developed and studied in the following main part of this work.

Chapter 4

Independent Control of Attosecond Pulse Generation

In chapter 3 we studied the control of attosecond pulse production by a single control parameter, the carrier-envelope phase (CEP) of the driving femtosecond laser field. We have seen that this control method alone has a large impact on high-order harmonic generation. Yet the capability of control is limited since it utilizes only a single control parameter. Thus, despite the fact that by the CEP control of HHG different properties of the produced attosecond pulses can be influenced, only one property can be set *at once*. In this chapter we enhance the control of attosecond pulse generation adding a second control parameter. High-order harmonic generation with two driving laser fields at different frequencies is studied. This way, the time delay between the two driving laser fields is gained as an additional control parameter besides the CEP. We introduce and demonstrate the concept of independent coherent control of high-harmonic generation for the example of attosecond double-pulse production. It will be numerically shown that the two control parameters act independently on the generation of attosecond pulses, which means that two qualitatively different properties of the produced attosecond pulses can be set at the same time. For instance, attosecond twin pulses of equal peak intensity can be generated while the spectral-phase difference between the pulses can be set at the same time. Such well-prepared twin pulses could be used for attosecond interferometry or control experiments. An increase of control parameters can enhance the control capability. But it also exponentially increases the complexity of the control scheme and the measurement or computing time which is needed to scan the full control space. Evolutionary algorithms can deal with a larger number of control parameters. However, when applying such algorithms it is very challenging to gain insight about the mechanisms and the effects of the individual control parameters, due to the complexity of the controlled multidimensional space. It is therefore most effective to identify the most powerful and independent control parameters and then perform the maximal (or aimed) control with the minimal number of degrees of freedom. We realize this approach with the concept of independent open-loop control.

Furthermore, it will be explained by the principle of kinetic-heterodyne mixing of laser fields why the control of high-order harmonic generation with a second laser field is very effective even when the second laser field is very weak. The method will be general-

ized leading to the effective control of HHG with a single laser field with a continuous broadband laser spectrum which is cut in two spectral sections. A variable time delay is then applied between the two sections. It is numerically studied to what extent this split-spectrum time-delay method in combination with the CEP control is capable of independent control of several temporal or spectral properties of the generated high-order harmonics or their corresponding attosecond pulses in the time domain.

The chapter is structured as follows: The principles of two-color control, kinetic-heterodyne mixing of laser fields and field synthesis are presented in section 4.1 as well as a definition of independent control capability. In section 4.2 the numerical model is described. In sections 4.3 and 4.4 we study the independent control of attosecond double-pulse production by the addition of the second harmonic and by the split-spectrum control method respectively. Parts of this chapter have been published in [136].

4.1 Principle

4.1.1 Definition of Independent Control

The principle of independent control of high-order harmonic generation is based on the idea that by having a set of control parameters at hand or by applying several control methods at once it could be possible to steer and realize several target quantities (in our case properties of the attosecond pulses in the temporal or spectral domain) at the same time. We define a control experiment e :

$$e : C \rightarrow T \quad (4.1)$$

Spanning a multidimensional control space C which contains all combinations of the control parameters we gain access to a target space T by the control experiment e , in which $\dim(C) = n$ is the number of control parameters. Other expressions for n are the number of degrees of freedom for the control or the number of control "knobs" we can apply. $\dim(T) = m$ is the number of target quantities we want to steer, in our case properties of the produced attosecond pulses (e.g. their total intensity, intensity ratios, number, spectral-phase difference between attosecond pulses, average photon energy, cutoff energy, and many more). We consider both the values of the control parameters and target quantities to be continuous, but the definition is fine with distinct values as well. We define a control experiment to be *multidimensional*, if both $n > 1$ and $m > 1$.

For $n > 1$ there might be many combinations $c \in C$ of the individual control parameters leading to the same aimed value for the first target quantity t_1 , with $t = (t_1, t_2, \dots)$. These combinations would form a subspace $S \subset C$ (e.g. a line in the two-dimensional case). Within this subspace S the second target quantity t_2 could then be set, and so on. In the best case a number of target quantities m equal to the dimension n of the control space can be set to a proposed value that way.

The applicability and power of this control scheme for a given control experiment e depends on the following three constraints:

1. the number of control parameters n .

2. the impact of each control parameter c_i on the individual target quantities $t = (t_1, t_2, \dots)$.
3. the degree of independence of the control parameters in their action on the target quantities.

The third constraint is fulfilled e.g. when each control parameter acts on only one, but respectively different target quantity. We define a set of n control parameters to be *fully independent* with respect to a set of $m = n$ target quantities if there exists for every element $t \in T$ a combination of control parameters $c \in C$, which results in the aimed combination of the target quantities t . The control parameters act often similarly or in a connected manner on the target quantities. Thus the set of control parameter has to be chosen carefully to be able to perform fully independent control. In this chapter the number of control parameters is restricted to two: the CEP and the time delay between the driver laser fields. After reviewing the effect of the addition of a second laser field on HHG alone, the independence of these two control parameters in terms of the above definition will be studied in sections 4.3 and 4.4.

4.1.2 Two-Color Control of High-Harmonic Generation

The addition of a second laser field at a different frequency to the fundamental laser field is a well-established method to control the generation of high-order harmonics and termed two-color control. Two-color HHG control is reviewed in Ref. [137] and an overview over atomic phenomena in two-color laser fields can be found in Ref. [138]. The coherent interference of the two laser fields substantially changes the shape of the resulting driving laser field, which is then applied for HHG. The modified shape of the electric driver field thereby depends on the time delay or relative phase of the two laser fields. Consequently the gained energy of the electrons in the shaped electric field, as well as contributions of individual trajectories, their recollision times and relative phases can be strongly influenced by two-color control methods. Experiments and simulations have been reported for a couple of different combinations of driver field frequencies and are listed in the following.

In 1994, it was shown that the addition of the third harmonic can enhance the high-harmonic intensity in the plateau region by an order of magnitude [139]. In the last years several approaches have been suggested how multi-color laser fields can be used to generate isolated single attosecond pulses and soft x-ray supercontinua [140, 141, 142, 143, 144, 145, 146, 147, 148]. Feng *et al.* described theoretically that an isolated attosecond pulse shorter than 40 as can be generated utilizing two chirped fields at 800 nm and 1200 nm [149]. Besides, it was demonstrated theoretically that attosecond double pulses can be produced in a chirped two-color laser field and the relative intensity of the double pulses can be changed just by adjusting the relative time delay of the two driving fields [140]. Mauritsson *et al.* showed that attosecond pulse trains with a stable CEP can be generated with two-color laser fields [150]. Furthermore, the CEP and the central frequency of the generated attosecond pulses can be controlled [151]. Two-color control of HHG allows also to vary the energy of single harmonics [152] or to manipulate the

relative strength of harmonics [153]. Chang [76] showed that with double optical gating the number of attosecond pulses and their intensities can be controlled by either the relative phase between the two-color fields or the CEP. Chan *et al.* [154] demonstrated experimentally that by Fourier synthesis of five discrete optical harmonics (1ω to 5ω) it is possible to tailor the optical field in the shape of a square, sawtooth or subcycle sine and cosine. They developed a method to measure these shapes, but they did not yet apply the pulses to HHG. Their findings illustrate the possible power of multicolor-methods to tailor a driving laser field.

4.1.3 Field Synthesis

Common to all multi-color control schemes is the fact that they make use of the spectral bandwidth $\Delta\omega = \omega_{max} - \omega_{min}$ to shape the driver pulses on a time scale which is given by

$$\delta t = 1/\Delta\omega. \quad (4.2)$$

To shape the laser field on a subcycle basis a bandwidth of at least one octave is required. For this aspect it is not important whether the covered spectrum is continuous or whether it contains spectral gaps, or whether it is even composed of several laser fields as long as the resulting spectral phase can be precisely controlled. Shaping on a subcycle basis would allow to produce more intense and shorter isolated attosecond pulses, which is a key goal in the attosecond community. Laser sources with an octave-wide continuous spectrum would deliver the necessary bandwidth for subcycle pulse shaping. Advances in the development of chirped mirrors [93] have enabled to deliver such laser pulses even with near-transform bandwidth limited pulse duration. Goulielmakis *et al.* generated a coherent supercontinuum with a bandwidth ranging from 220 nm to 1000 nm by self-channeling in helium [155], yet with a non-flat spectral phase. Later Goulielmakis *et al.* utilized near-bandwidth-limited ~ 3.5 fs long pulses for CEP-controlled high-harmonic generation, attosecond metrology and spectroscopy. They termed the steering of electrons inside and around atoms "lightwave electronics" [156].

To gain comprehensive control with that bandwidth at hand it is now necessary to have control over the spectral phase $\phi(\omega)$ and to have more control parameters besides the CEP (ϕ_0). A few methods have been studied so far. One option to realize the missing additional control parameters is to split up a continuous broadband laser spectrum into two or more spectral sections and apply a time delay between the spectral sections. This split-spectrum time-delay method was introduced by Dudovich *et al.* for applications in femtosecond control [157]. We apply this method to the independent control of attosecond twin-pulse production [136] by high-harmonic generation in section 4.4 and to the generation of combs of fractional high-order harmonics [158] in chapter 5. Recently, Wirth *et al.* built up a sophisticated optical field synthesizer, where they divided a continuous laser field spanning 1.5 octaves from 330 nm to 1100 nm into three channels [159]. The pulse compression is done in each of the three channels, since there are no chirped mirrors available which are suitable for the whole spectrum. Time delays between the three channels are applied to generate pulses shorter than one optical cycle, which they name "light transients", while its generation and measurement is referred to as "synthesis". The

idea behind this is to be able to almost arbitrarily shape few- or subcycle optical pulses in analogy to a microwave synthesizer [160]. As an application Wirth *et al.* field ionized krypton atoms with a subcycle light transient to study the dynamics of a valence-shell electron wave packet evolving from well-defined initial conditions. Huang *et al.* [161] demonstrated numerically the capability of field synthesis to generate isolated attosecond pulses without or with greatly reduced need for temporal gating or spectral filtering.

4.1.4 Kinetic-Heterodyne Mixing of Laser Fields

An important principle in two-color control of HHG is the effect of kinetic-heterodyne mixing of laser fields, which was introduced by Pfeifer *et al.* [162, 163]. They found that the coherent addition of a laser field at a different frequency ω_2 has a large impact on HHG even if the intensity of the second field is weak (e.g. only 1% of the intensity of the strong field at ω_1). This way for example the half-cycle symmetry of the electric driver field can be broken, which leads to the generation of even harmonics (see Fig. 4.1c). To understand the mechanism of this principle we calculate the classical velocity an electron gains in the superposition of the electric fields $E_1(t) + E_2(t)$ at the distinct frequencies ω_1 and ω_2 with a relative phase φ :

$$v = - \int_{t_0}^{t_r} [E_1(t) + E_2(t)] dt = v_1 + v_2 \quad (4.3)$$

$$v_1 = \frac{\hat{E}_1}{\omega_1} [\sin(\omega_1 t_0) - \sin(\omega_1 t_r)] \propto \hat{E}_1 \quad (4.4)$$

$$v_2 = \frac{\hat{E}_2}{\omega_2} [\sin(\omega_2 t_0 + \varphi) - \sin(\omega_2 t_r + \varphi)] \propto \hat{E}_2 \quad (4.5)$$

The kinetic energy of the electron is then given by:

$$E_{kin} = \frac{1}{2}(v_1 + v_2)^2 = \frac{1}{2}(v_1^2 + v_2^2 + 2v_1v_2) \quad (4.6)$$

If the intensity of the second (weak) field is 1% of the first (strong) field, its electric field peak amplitude \hat{E}_2 is still 10% of \hat{E}_1 , since the electric field is the square of the intensity. Thus the velocity the electron is able to gain can be modulated by $\sim 10\%$ by the second field. The possible modulation of the kinetic energy is then $\sim 21\%$. It is encoded in the term $2v_1v_2$, where we can see that the influence of the weak field is amplified by $2v_1$.

We now introduce the generalization of this principle, which is its application to field synthesis with a single broadband laser field. The field is cut into two spectral sections, such that the integrated intensity of the second section is only a small fraction of the intensity in the first section (see Fig. 4.1d). We obtain a strong and a comparably weak field with different center frequencies. For those two subfields all considerations of above-discussed kinetic-heterodyne mixing principle are applicable, which we now refer to as *generalized kinetic-heterodyne mixing of laser subfields*. We see in Fig. 4.1d-f) that both intensity ($|E(t)|^2$) and electric field are strongly modulated by applying a time delay between the section with only 1% relative intensity and the main spectral section. The shaping of the pulse occurs here on a time scale which is identical to the pulse duration,

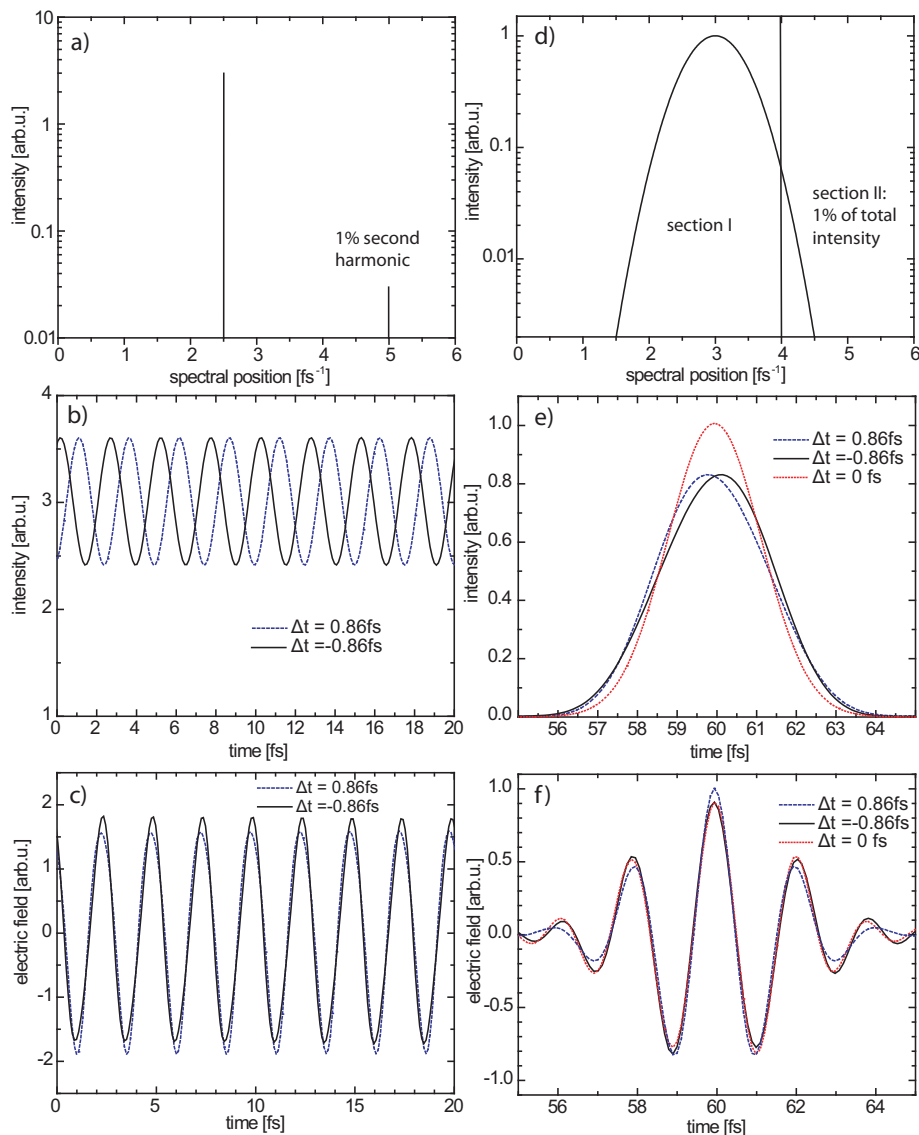


Figure 4.1: Kinetic-heterodyne mixing of two continuous-wave (cw) laser fields (a-c) and generalized kinetic-heterodyne mixing of two laser subfields (d-f). Even the addition of a weak second harmonic with 1% intensity (a) strongly modulates the intensity of the driver laser field (b) and leads to a pronounced asymmetry of the electric field (c) for the time delay +0.86 fs (dashed lines) and -0.86 fs (solid lines). Similarly, a time delay between a 1%-relative intensity spectral section (II) of a broadband spectrum (d) and the main section (I) leads to a remarkable intensity modulation of the driver field as well (e). The field is now compressed to a few-cycle pulse. Pronounced changes of the electric field are displayed for the time delays +0.86 fs (dashed line), -0.86 fs (solid line) and 0 fs (dotted line).

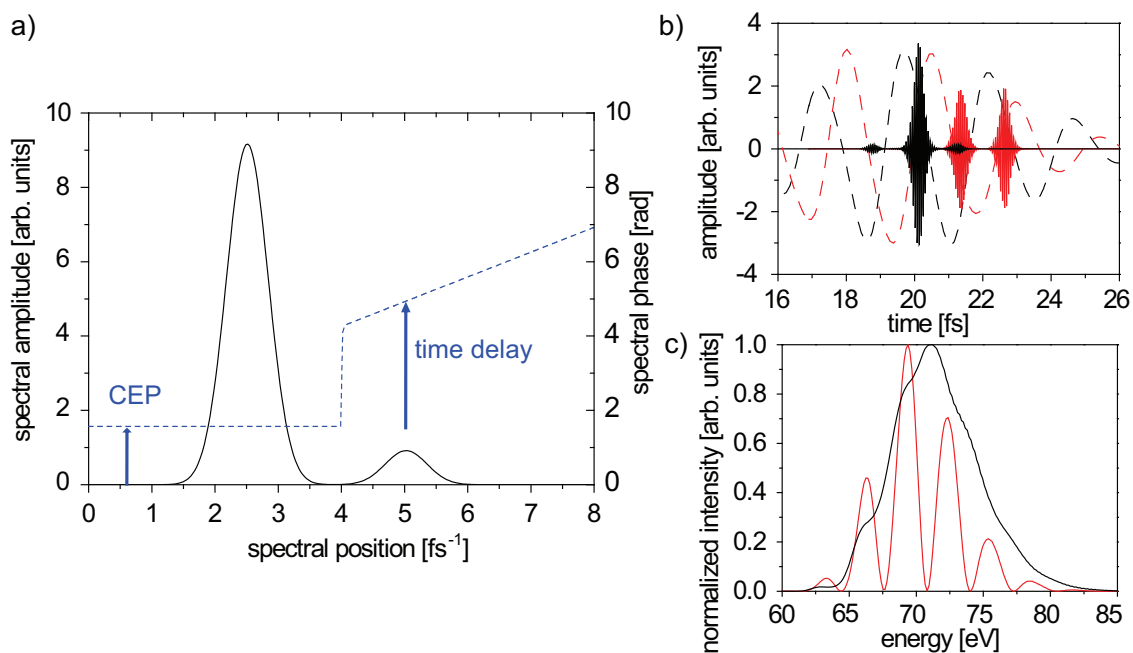


Figure 4.2: Kinetic-heterodyne mixing of laser fields for attosecond twin-pulse generation (from [136]): a) Spectral phase (dotted line) and amplitude (not intensity!) of driving laser fields. b) Shaped electric fields of two different driving laser pulses (black and red dashed lines) and electric fields of generated attosecond pulses (black and red solid lines). c) Spectrum of the emitted attosecond pulses shown in (b).

for which reason we do not observe multiple intensity oscillations as in the case of two separate spectral frequencies in Fig. 4.1b). As a consequence of the generalized principle for field synthesis, it is not necessary to divide the broadband laser field into spectral sections of comparable intensities to perform effective control of HHG. And what is even more important: It is the almost full bandwidth of the laser spectrum which is strikingly accessible for the control, including the wings of the spectrum. A good measure for the accessible bandwidth in equation 4.2 is rather the width (e.g. at $1/e$ of the maximum) of the spectral amplitude $\bar{E}(\omega)$ than the width of the spectral intensity $\bar{I}(\omega)$.

4.2 Numerical Model

In this section the numerical model for the two-color control of HHG with a second-harmonic laser field is described. The results are then discussed in section 4.3, while the results in section 4.4 are obtained by an adaption of this model. We consider a two-color laser field, consisting of a strong fundamental pulse with a center wavelength of 750 nm and a weak second-harmonic (SH) pulse centered around 375 nm. We choose the frequency-doubled SH as the second laser field, because the SH is experimentally well accessible, for example by using a barium borate (BBO) crystal for SH generation out of the fundamental laser field. The laser pulses are Gaussian-shaped with a spectral width of 0.275 fs^{-1} FWHM (full width at half maximum), corresponding to a bandwidth-limited pulse duration of 5 fs FWHM. The peak intensities of the laser pulses are kept constant at

2.6×10^{14} W/cm² (fundamental pulse) and 2.6×10^{12} W/cm² (SH pulse) respectively. The spectral phase of the combined field of fundamental and second harmonic driver pulses is calculated, using the CEP of the main pulse and the time delay of the SH pulse as free parameters (see Fig. 4.2a). Inverse Fourier transformation into the time domain gives the shaped laser field (Fig. 4.2). To simulate the generation of attosecond pulses, we calculate the single-atom response of a model neon atom in the shaped laser field as a function of both the CEP and the time delay between the two laser fields. For this purpose, we numerically solve the time-dependent Schrödinger equation for an electron bound to a soft-core Coulomb potential [164]. We use the split-step operator method [165, 166] to solve the Schrödinger equation. Out of the dipole-acceleration expectation value we obtain the high-order harmonics spectrum by employing Ehrenfest's theorem [167]. The restriction to one spatial dimension is necessary for keeping the computation time to an acceptable level for the calculation of the multidimensional control data sets shown in the following sections. In order to reject the low-energy harmonics in the spectrum (as would be necessary experimentally) we apply a filter and an additional spectral phase according to the absorption and dispersion in 0.4 μ m zirconium. Complex inverse Fourier transformation then gives the attosecond pulses in the time domain.

4.3 Control with the Second Harmonic

Having described the numerical model we now can discuss the results of the combined control of HHG by both, the CEP and the addition of a weak laser field at the doubled frequency. After spectrally filtering out the low-order harmonics, only one or two strong attosecond pulses are produced, depending on the CEP and the time delay between the two laser fields. Besides these strong pulses, up to three satellite pulses can be observed, whose intensity is ~ 100 times less than the intensity of the main pulses. In Fig. 4.3a the ratio R of the peak intensity of the two most intense attosecond pulses is plotted as a function of the CEP and the time delay between the fundamental and the weak SH pulse. A ratio $R = 1$ means that two attosecond pulses with equal peak intensity are generated. The simulation shows that such pulses with $R = 1$, which will be further referred to as attosecond twin pulses, can be generated for various combinations of the CEP and the time delay. Furthermore, one can see in Fig. 4.3a) that by only changing the CEP and the time delay the intensity ratio R can be controlled by more than two orders of magnitude. If R approaches 0, the intensities of the weakest attosecond pulses become negligibly small so that a single isolated attosecond pulse remains. Thus, by applying the combined CEP and two-color control method it is feasible to generate both, isolated attosecond twin pulses and isolated single attosecond pulses. The attosecond pulses in Fig. 4.2b) have durations (FWHM) between 210 as and 259 as, mostly limited by the available HHG bandwidth, which could be increased by scaling to higher intensities or longer wavelengths.

Moreover, we can make use out of the ability of our multidimensional control scheme. To demonstrate that our two control parameters (the CEP and time delay) allow for independent control of attosecond pulse production, we show that two properties of the generated attosecond pulses (e.g. the number of attosecond pulses produced, their total intensity, their intensity ratio or their relative spectral phase) can be controlled at once.

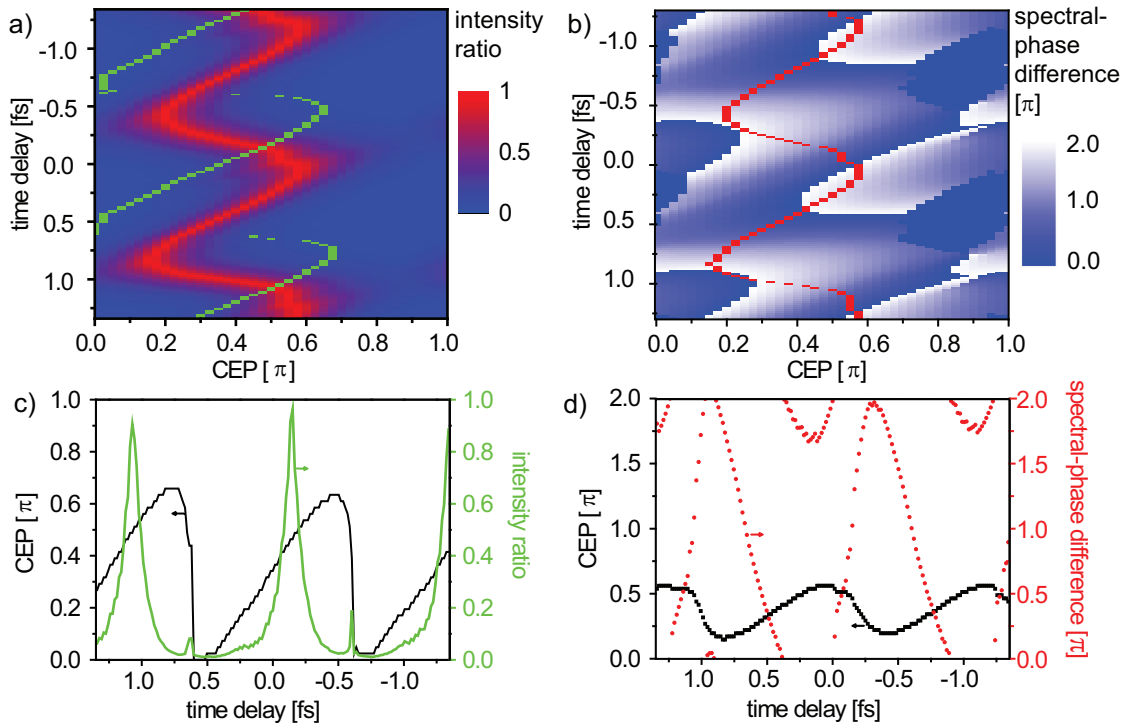


Figure 4.3: Control of attosecond pulse generation with a two-color laser field consisting of a fundamental pulse and a weak second harmonic pulse (from [136]): a) Intensity ratio of the attosecond double pulses as a function of the CEP of the fundamental pulse and the time delay between the fundamental pulse and SH pulse. The green line indicates the parameters that result in a spectral-phase difference of π . b) Control of the spectral-phase difference between the attosecond pulses by the CEP and the time delay. The red line traces the maximal values of a), indicating the positions at which a perfect twin pulse is generated. c) Intensity ratio (green line) of attosecond pulses at a constant spectral-phase difference of π . d) Spectral-phase difference (red dots) at a constant intensity ratio of 1 and corresponding CEP (black squares).

As a condition we have to leave all the experimental parameters constant, except for our two control parameters. To this purpose, we study whether we still have full control over one target quantity while keeping another target quantity constant at a chosen value. As an example we choose to keep the intensity ratio constant at $R = 1$, meaning we choose to have perfect attosecond twin pulses. As an important example towards phase-control of quantum processes we secondly choose the relative spectral-phase difference between the two attosecond pulses as our second target quantity. We determine the relative spectral-phase difference by spectral interferometry analysis [168, 169] as follows: The spectrum of the attosecond pulses is band-pass filtered using a Fourier filter to retain only the modulating component resulting from the interference between the two attosecond pulses. The relative spectral-phase difference is then given by the argument (phase) of the filtered complex-valued spectrum. After subtracting each time the same linear phase term (which corresponds to a time delay between the two attosecond pulses) the spectral-phase difference is constant in energy within a standard deviation of 0.2π .

Fig. 4.3b) shows the relative spectral-phase difference between the attosecond pulses modulo 2π for $0.01 < R < 1$. The spectral-phase difference can be set to any value

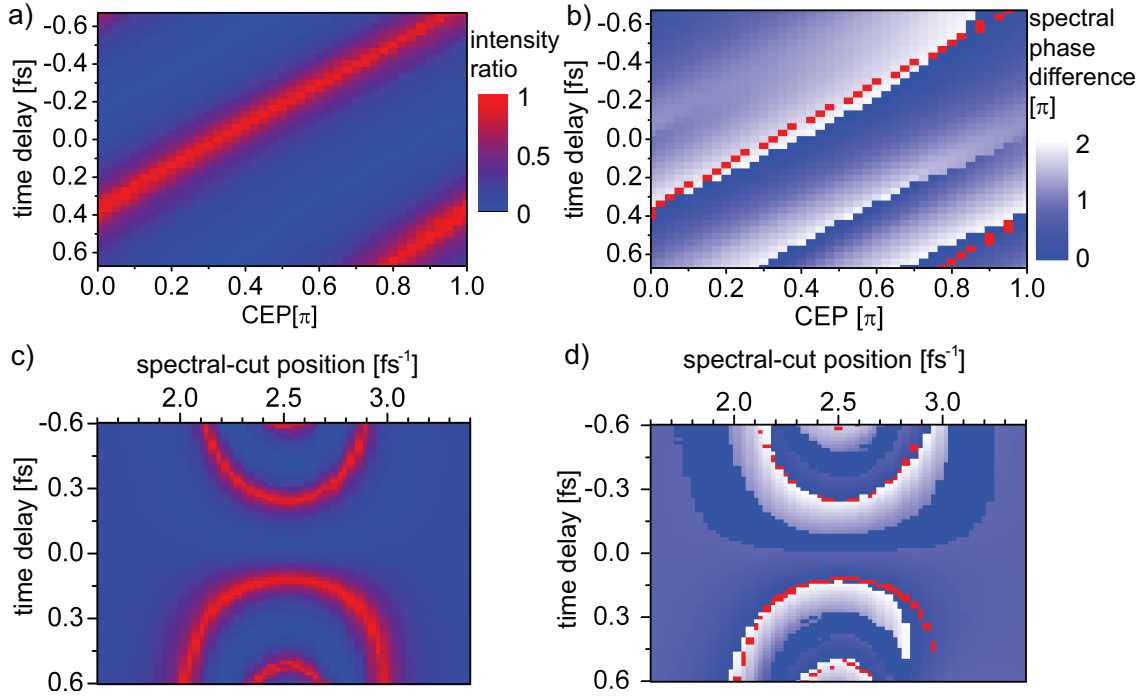


Figure 4.4: Control of attosecond double-pulse generation by splitting up a broadband laser spectrum into two sections and applying combined CEP- and time-delay control (from [136]): a) Dependence of the intensity ratio of the two main attosecond pulses on the CEP and the time delay between the two parts of the laser spectrum (spectral cut located at 2.1 fs^{-1}). c) Control of the intensity ratio of the two main attosecond pulses as a function of the time delay and the spectral-cut position. b) and d) Spectral-phase difference between the attosecond pulses as a function of the time delay and the CEP (b) and as a function the time delay and the spectral-cut position (d). The red lines trace the maximum found in a) and c), demonstrating the control over the relative spectral phase while retaining an attosecond twin pulse at a constant intensity ratio of 1.

within the entire range between 0 and 2π while at the same time the peak intensity ratio is constant (Fig. 4.3d)). On the other hand, the intensity ratio can be freely chosen while keeping the spectral-phase difference constant (Fig. 4.3c)). Thus we have numerically proven the ability of independent control of attosecond double-pulse production with the CEP and the time delay as control parameters.

4.4 Control by the Split-Spectrum Time-Delay Method

In the last section we have shown that the CEP control in combination with the two-color technique gives access to the simultaneous manipulation of several properties of the generated attosecond pulses. We now transfer the approach to the broadband, and nowadays even ultra-broadband laser sources. To keep the time-delay knob, which we have proven to be essential for a comprehensive control of HHG, we divide our spectrum into two parts between which we apply the time delay. This way we obtain the spectral position of the arbitrary cut between the two sections as additional control parameters, of which we now have three. The laser intensity could be chosen as fourth control option, to fur-

ther enhance the controllability in terms of number of desired properties of the attosecond pulses that could be manipulated. To reduce complexity in the result figures we choose to restrict ourselves to two combinations of two control parameters:

1. The CEP and the time delay.
2. The spectral-cut position and the time delay.

The principle of generalized kinetic-heterodyne mixing of laser fields plays an important role for the power of this control scenario as will be justified by the following insight: When the cut-position is moved from the center of the spectrum towards either of the spectral edges, the energy ratio of the two spectral sections differs increasingly from one. This can be pushed to the situation where a small fraction of the spectrum forming a weak field is time delayed with respect to the rest of the spectrum forming a strong field. The principle of generalized kinetic-heterodyne mixing as described in section 4.1.4 now means that this small fraction, even if its energy content is as small as 1% of the total energy, still retains a huge impact and control capability on the HHG process. Thus the cut position can be tuned over almost the whole spectral bandwidth without loss of impact on the process of high-order harmonic generation.

The approach can be realized experimentally by spectrally resolving the driving laser field with a prism or grating and employing a split mirror for the time-delay control. The split mirror changes the optical path length for one part of the laser spectrum with respect to the other part leading to a spectral-phase shift analogous to that in Fig. 4.2a). Numerical simulations were performed using the same model as in the previous section, but this time with only one Gaussian pulse of 2.9×10^{14} W/cm² peak intensity centered around 750 nm with a spectral phase defined by the CEP, the spectral-cut position and the time delay. The simulations of the generated attosecond pulses show that their intensity ratio R can again be varied over two orders of magnitude. This can be achieved both by changing the CEP and the time delay for a spectral cut located off-centered at 2.1 fs^{-1} (see Fig. 4.4a)), as well as by tuning the time delay and spectral-cut position, leaving the CEP constant at 0 (see Fig. 4.4c)). In both cases isolated single attosecond pulses (e.g. $R \leq 0.02$) can be generated as well as isolated attosecond twin pulses ($R = 1.00$) for various combinations of the control parameters. The spectral-phase difference between the two attosecond pulses can be controlled within 0.7π by adjusting the CEP and the spectral-cut position (see Fig. 4.4b) and 4.4d)), while leaving the intensity ratio constant.

As a result, we find that the CEP and the spectral-cut position are only partially independent in this configuration. They are correlated in their mechanism to influence the studied attosecond double pulse properties relative intensity and spectral-phase difference. The same holds for the combination of time delay and CEP, where the correlation is even stronger. We expect that this correlation between the influence of the CEP and the time delay decreases with increasing accessible bandwidth. Fully independent control should become at the latest feasible when the bandwidth exceeds one octave so that it contains its second harmonic and thus becomes similar to the configuration in the last section. The observed correlation is not necessarily present for other combinations of attosecond pulse properties. In our simulation we considered a laser pulse with a bandwidth that is much lower as today's leading super-octave wide laser systems, but we have chosen the

bandwidth corresponding to our setup and the setup of other groups (delivering 5 fs long pulses, FWHM). Current and future achievements in laser and dispersion control technology will further advance the power of the presented split-spectrum time-delay method towards a comprehensive control tool to steer electron dynamics in atoms and molecules on their natural attosecond time scale. Apart from this we already observed a remarkable control capability in the split-spectrum configuration. As it was shown here, while we did not even make use of all three and more control knobs at the same time, we can set the intensity ratio of the attosecond pulses, prepare attosecond twin pulses as well as isolated attosecond pulses and are able to manipulate the spectral-phase difference between the perfectly-balanced attosecond twin pulses within 0.7π .

4.5 Conclusion

In this chapter we have combined the principles of CEP control, two-color control and kinetic-heterodyne mixing of laser fields to a versatile control approach for high-order harmonic generation. We have established the concept of multidimensional and independent coherent control of high-harmonic generation where in principle as many properties of the attosecond pulses can be independently controlled as there are control variables. We have demonstrated the capability of this scheme at the independent control of attosecond double pulses. Employing only the two control parameters CEP and time delay isolated attosecond pulse as well as attosecond twin pulses with equal intensity can be generated. The spectral-phase difference between these attosecond pulses can be set in the full range between 0 and 2π without changing the intensity ratio. We have extended the control scheme towards the independent coherent control with a single continuous laser spectrum which is divided into two arbitrary sections between which a time delay is applied. We introduced the generalized principle of kinetic-heterodyne mixing of laser subfields. Showing that almost the entire spectral bandwidth including the spectral wings is available for effective control, the generalized principle has important implications for field-synthesis applications. It provides us the spectral-cut position as a third parameter for HHG control. The combination CEP and time delay as well as the combination spectral-cut position and time delay were found to be partially independent in their control effect on HHG. Isolated attosecond pulses and attosecond twin pulses with a tunable spectral-phase difference can be delivered with the split-spectrum time-delay scheme as well.

There were no special temporal gating techniques (e.g. polarization gating [12, 74]) applied in the simulations. Yet, the generation of isolated single and double attosecond pulse could be provided by intensity gating. The low-energy harmonics were filtered out in the same way as realized with zirconium foils in the experimental implementation, obtaining approximately an open temporal gate, when the intensity is above a threshold. Thus the gate is fixed to the envelope of the shaped laser pulse, while the electric field carrier can be shifted under this envelope by the CEP. The presented results should therefore be able to be transferred to all gating techniques which are mainly intensity dependent or fixed to the pulse envelope. The independence of the CEP and the time delay in their action on the generation of attosecond pulses should not be affected by the choice of another gating

technique or the application of different phase-matching conditions. In the next chapter we will experimentally realize the here-developed multidimensional control scheme by utilizing a single broadband CEP-stable laser field.

Chapter 5

Fractional High-order Harmonic Combs - Coherent Control of Attosecond Pulse Trains

In the last chapter we introduced and numerically studied the control of high-order harmonic generation (HHG) by the combination of carrier-envelope phase (CEP) control and field synthesis using few-cycle CEP-stabilized laser pulses. We found that this control scheme provides independent control over several properties of the produced high harmonics. In this chapter, we want to experimentally apply this split-spectrum time-delay control scheme to HHG. For this purpose we apply a prism-based 4f-pulse shaper. A split mirror is located in the Fourier plane, which divides the spectrum into two variable sections between which a time delay is applied. We use this time delay, the spectral-cut position and the CEP as control variables. In the harmonic spectrum we observe additional features components generated at distinct time delays, which constitute fine combs of fractional (noninteger-order) high harmonics. We find these combs to be produced by the controlled coherent interference of two attosecond pulse trains which are spaced in time. While in the last chapter we have studied the coherent control of single and double attosecond pulses, in this chapter we perform the independent and manifold control of attosecond pulse *trains*. We experimentally observe a number of different spectral and temporal effects of the control of the high harmonics. Since we only use a few control variables we are able to extract the physical origins and mechanisms behind these effects in the time and energy domain. We show how the phenomena can be precisely steered by just the three above-mentioned control variables. Among these effects are the beating of the harmonic intensity with the time delay and a strong energy-tuning capability of the individual high harmonics. We develop a quantitative and intuitive model to understand and predict these energy modulations steered by the time delay between the two subfields.

The experimental results are guided and compared to numerical simulations based on the strong-field approximation. Macroscopic effects (e.g. the target gas pressure, focusing conditions or the length of generation medium) are on purpose not considered in our models and simulations. In this chapter, we want to point out the power of the purely microscopic picture based on the single-atom response to explain our experimental findings and we demonstrate the ability of the applied technique to enhance the control of

HHG. Since we intend to extract the individual control mechanisms we do not apply the CEP-control in the first series of experiments. Extracting these mechanisms, we gain insights how the control of HHG is achieved in detail and which series of effects of the individual control parameters lead to the observed changes of HHG and the properties of the generated attosecond pulses. The CEP control is then added in a second series of measurements. Having introduced the generalized principle of kinetic-heterodyne mixing of laser subfields in the last chapter, we now apply the principle in this chapter and experimentally check its validity. Moreover, we experimentally verify the principle of independent control by the combination of the CEP and the time-delay control, which we developed in chapter 4 as well. We make use of the multidimensional controllability of our control scheme, which is the ability of multiple control knobs to steer several target quantities at once, to in this case further optimize the produced fractional high-order harmonic combs. We aim for combs with a fully modulated intensity contrast and regular frequency spacing over a broad spectral range in the extreme ultraviolet (XUV). One application of such combs lies in the field of high-precision frequency metrology and interferometry. Moreover we apply the method of CEP SI introduced in chapter 3 to the fractional-harmonic combs to study the time structure and relative phase of the two interfering APTs. This analysis opens the door to the complete-information retrieval in XUV transient-absorption spectroscopy. Besides, we find that temporal chirps of the driving laser field have a significant influence on the controlled high-harmonic spectrum, which is investigated. Finally, we extract how the individual control parameters act on high-harmonic generation in the combined control scheme.

The chapter is structured as follows: After reviewing noninteger harmonic generation in section 5.1, the design and setup of the split-spectrum pulse shaper is described in section 5.2. The numerical model used in the simulations is then illustrated in section 5.3, while the results for the measurements with averaged CEP are presented and discussed in detail in section 5.4. Both comparisons to simulations and the energy tuning model are shown in this section as well. Section 5.5 presents the CEP-stabilized measurements and the optimization of the fractional high-order harmonic combs, their analysis by CEP SI as well as temporal chirp studies and the influence of the individual control parameters. Finally, some applications of the fractional high harmonics are discussed in section 5.6 and the results are summarized in section 5.7. Parts of this chapter have been published in Ref. [158].

5.1 Noninteger High-order Harmonic Generation

As the observation of fractional (noninteger) high-order harmonics is one main result in this chapter, the generation of noninteger-order harmonics is reviewed in this section. Commonly, only the odd orders of the harmonics are produced in HHG. This results from the fact that usually every half laser cycle $\frac{T}{2}$ an attosecond pulse is generated. Fourier transformation into the energy domain gives an energy spacing of two times the fundamental energy ω : $\frac{2\pi}{T/2} = 2\omega$. Even and odd order harmonics can be produced if the symmetry of the driving laser field is broken in a way that every full laser cycle an attosecond pulse is emitted [162, 170], which results in an $1-\omega$ -spacing of the high harmonics:

$\frac{2\pi}{T} = \omega$. In 2011, Teng *et al.* [171] showed that in sub-5-fs driver pulses the symmetry between sequent half-cycles is broken, which leads to the production of attosecond pulses which differ in amplitude and phase. This can produce a complex, irregular spectrum which contains noninteger harmonics.

Already in 1998, it was found that HHG with two beating driver fields leads to spectral modulations with maxima spaced by the frequency difference of the two laser fields $\omega_2 - \omega_1$ [172, 173, 174]. A broad quasicontinuum was measured in krypton and argon by adding to the 800 nm fundamental field a second field at almost double wavelength [175] and in argon and neon by adding a 1.45 μm field [176]. The mixing of two unrelated frequency fields is also found to increase the cut-off energy and the harmonic yield [175, 176]. Takahashi *et al.* [177] demonstrated experimentally and numerically that it is possible to generate an intense isolated attosecond pulse by superposing an 800 nm with a 1300 nm laser field. They explain the observed dense harmonic spectrum by high-order sum and difference frequency generation, which was theoretically described by Gaarde *et al.* [178]. The energy of the noninteger high harmonics which are generated by a two-color field consisting of the frequencies ω_1 and ω_2 can be expressed by the sum of multiples of these frequencies:

$$E = n_1\omega_1 + n_2\omega_2 \quad (5.1)$$

So far, the generation of noninteger harmonics is well understood in the energy domain, but it is in most cases still lacking a clear picture with an experimental evidence about the mechanism in the time domain.

Besides applying multi-colors fields, a different way of producing high-harmonic combs is the implementation of fine substructures into the individual harmonics themselves for example by applying frequency-comb stabilized IR driver pulse trains. The generation of very regular frequency combs (spectra of equally spaced lines, for a review see Refs. [179, 180]) in the extreme ultraviolet has been pioneered by the group of T. Hänsch [181, 182] utilizing HHG in an enhancement cavity. The generation of frequency combs in the XUV by HHG has also been reported by Jones *et al.* [183] and recently by Cingöz *et al.* [184]. The odd high harmonics, which are generated intra cavity in their setup, split up and form a fine and coherent frequency comb down to wavelengths of 40 nm, yet containing spectral gaps between the odd harmonics.

5.2 Design and Set-up of the Split-Spectrum Pulse Shaper

The setup of the split-spectrum pulse shaper utilized in the experiment is illustrated in Fig. 5.1. A precise time delay between two arbitrary parts of the broadband laser spectrum can be introduced by a highly stable split mirror placed in the Fourier plane of a 4f-pulse shaper [185]. This configuration enables a coherent shaping of the broadband IR laser pulses with a high-precision timing control of ~ 400 as or better. From the interferometrically determined stability of a similar split mirror equipped with a piezo stage with the same specifications we obtained a temporal stability between the spectral components

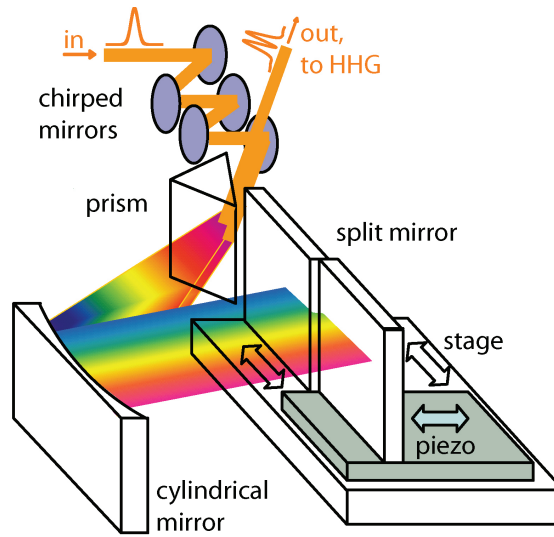


Figure 5.1: Setup of the split-spectrum pulse shaper (from [158]). A piezoelectrically driven split mirror is located in the Fourier plane of a Brewster-angled prism-based 4f-pulse shaper. The dispersion is compensated by a customized chirped-mirror compressor. The beam enters through the chirped-mirror compressor and is incident on the prism before a cylindrical mirror spectrally collimates and spatially focuses the beam onto the split-mirror surface. The beam is then redirected in reverse through the setup, leaving slightly above the original entrance spot to avoid the closest chirped mirror and is then sent to the HHG experiment.

of ~ 40 as. The accessible spectral bandwidth of the pulse shaper is only limited by the bandwidth of the chirped-mirror compressor (550-1000 nm in our setup). The split mirror is placed on a perpendicularly operated translation stage so that the cut position in the spectrum can easily and reproducibly be scanned throughout the full extent of the spectrum. The stage has a low pitch and yaw deviation ($< 20 \mu\text{rad}$, and $< 40 \mu\text{rad}$ respectively) which means the shaped beam is only negligibly affected when the split mirror is moved. Both parts of the split mirrors are aligned in a way that the two spectral parts propagate on top of each other and have the same focus spot position and size, which is confirmed by recording the focus spot with a complementary metal-oxide-semiconductor (CMOS) camera. The laser spectrum after the pulse shaper is measured with a fiber-coupled IR/VIS spectrometer.

The dispersion accumulated due to about 9.8 m air and 23.1 mm fused silica in the total optical path was compensated by 13 broadband chirped mirrors. The chirped-mirror compressor was customized in a way that the dispersion, including higher orders, is well compensated resulting in a near-flat spectral phase. The calculated deviation of $\phi(\omega)$ from zero is $< 0.3\pi$ over a large wavelength range as illustrated in Fig. 5.2). A large amount of the dispersion is caused by the fused silica prism, but the choice of a Brewster prism instead of a grating allows for a higher optical throughput and for a spectral bandwidth exceeding one octave [186], which is not possible for a grating due to overlapping diffraction orders. Another difference between the choice of a grating and a prism as dispersive element is the dispersive opening angle $\Delta\alpha = \alpha(\omega_{max}) - \alpha(\omega_{min})$. Due to the large bandwidth $\Delta\omega$ the angle is big for a grating with sufficient diffraction efficiency, but much smaller for a prism. A large $\Delta\alpha$ forces the choice of a small focus length f in

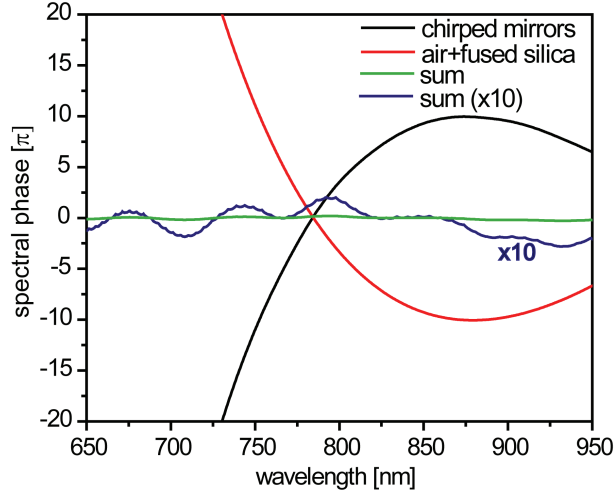


Figure 5.2: Compensation of dispersion (simulation result, from [158]). Calculated change of the spectral phase due to the dispersion of 9.8 m air and 23.1 mm fused silica in the setup (red), due to the customized broadband chirped mirrors (black), the sum of both (green), and the sum magnified by a factor of 10 (blue). The spectral phase after the compensation is close to flat over a long wavelength range, allowing the shaping of few-cycle laser pulses.

the 4f-setup, which is difficult to realize. We have chosen a prism for the higher power throughput and a more suitable choice of f , whereas it has the drawback that the dispersion compensation is sensitive to the prism insertion and thus the alignment.

A temporal chirp can be introduced in a controlled manner for studies of its influence on the experiment. This can be realized by changing the amount of fused silica in the beam path, e.g. by adapting the insertion of the two wedges or the prism. The split-spectrum shaped laser pulses are then used as driving pulses for controlled high-order harmonic generation in argon utilizing the attosecond beamline described in section 2.7.

5.3 Numerical Model

In the following the numerical model for the simulations of split-spectrum controlled HHG, to which we compare our experimental results, is described. The experimental split-spectra, measured after the pulse shaper, are used for the simulations. The laser peak intensity is set to 0.44 PW/cm^2 at zero time delay since this corresponds to the experimental situation. A variable time delay between the two parts is introduced by adding a linear spectral phase to the part with the higher spectral frequency, as it is in the experiment:

$$\Delta\phi(\omega) = \begin{cases} 0, & \omega \leq \omega_{cut} \\ \tau\omega, & \omega > \omega_{cut}. \end{cases} \quad (5.2)$$

ω_{cut} is the spectral-cut position. For some simulations the residual spectral phase after the dispersion compensation was included:

$$\phi(\omega)_{residual} = \phi(\omega)_{SPM} + \phi(\omega)_{fused\ silica} + \phi(\omega)_{air} + \phi(\omega)_{chirped\ mirrors}, \quad (5.3)$$

where $\phi(\omega)_{SPM}$ is the spectral phase due to the self-phase modulation (SPM) in the hollow fiber. Considering the CEP ϕ_0 , the total spectral phase yields:

$$\phi(\omega) = \phi_0 + \phi(\omega)_{residual} + \Delta\phi(\omega). \quad (5.4)$$

The electric field of the shaped driving laser pulse is then given by Fourier transformation into the time domain. The phase-stable field can be calculated for different CEPs and is used to compute the ionization rate and electron trajectories by applying the strong-field approximation. The ionization rate is given by the ADK-rate [30] in Eq. 2.16. Only the short trajectories were considered for the calculation of the high harmonics and a spectral filter corresponding to the absorption in the aluminum filters was not applied since the absorption in the experimentally observed energy region is negligible (see Fig. 2.11).

5.4 CEP-averaged Results

5.4.1 Experimental Details

Here, the remaining experimental settings for the measurements which are presented in this chapter are summarized as far as they have not been given in the sections 5.2 and 2.7, where the experimental setup of the pulse shaper and the attosecond beam line have been described. The step size for the time-delay scans between the two spectral sections was 67 as. The CEP control was only applied in the second part of the experiment. For HHG the shaped laser pulses were focused by a spherical mirror with 50 cm focal length into a gas tube filled with argon at a backing pressure of ~ 60 mbar. The laser peak intensity was ~ 0.44 PW/cm² for zero time delay, as derived from the harmonic cut-off energy. A spectral overlap of all colors at the same focus spot was ensured by measuring the focus position for the different spectral components with a CMOS camera.

5.4.2 Beating of the Harmonic Intensity

Fig. 5.3b) shows the recorded high-order harmonics as a function of the time delay between the two spectral sections. The corresponding split spectrum is depicted in Fig. 5.3a). As expected we measure the odd orders of the harmonics (orders 23 to 29, as labeled in the figure). As a first pronounced effect we see that the intensities of the high harmonics beat with the time delay. The period for this beating is 2.80 fs for all harmonics and thus in rough agreement with the laser cycle T . The beating of the individual harmonics is in phase. The reason for the harmonic intensity beating is a periodic change of the temporal intensity profile of the shaped driving laser pulse when the time delay is scanned through the temporal overlap of the two subfields. This periodic change is illustrated in Fig. 5.4, where the measured spectrum and residual spectral phase after the dispersion compensation were used to calculate the pulse intensity for different time delays. At time delays $\Delta t = NT$, with integer N , the subfields (given they overlap in time) interfere constructively at the temporal center of the pulse, forming a pulse shaped like that in Fig. 5.4a). In contrast, at time delays $\Delta t = T/2 + NT$ the subfields interfere

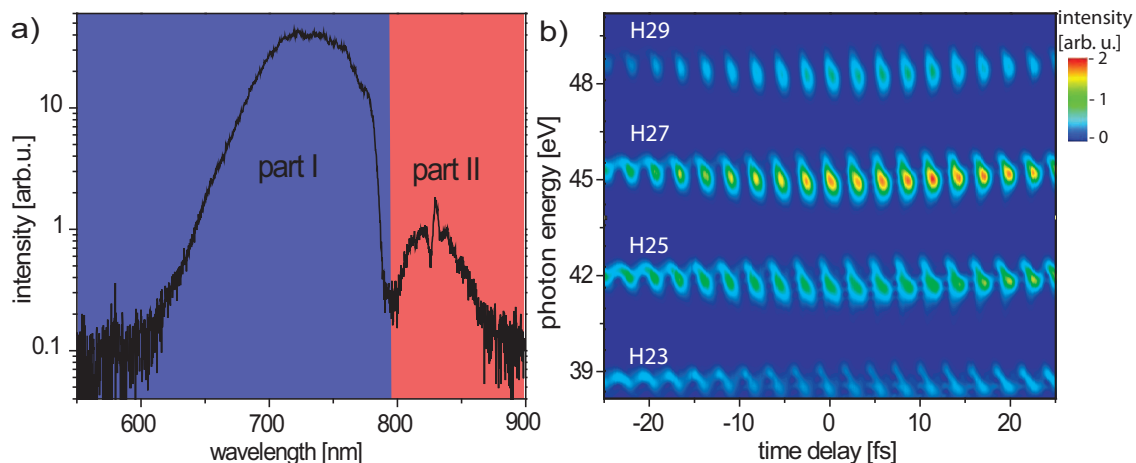


Figure 5.3: Beating of the high-order harmonics (experimental results, from [158]). a) Driving split-spectrum fundamental pulse with the spectral cut at 795 nm. b) Spectra of the high harmonics as a function of the time delay between the two subfields labeled part I and II in a).

destructively at the center of the pulse, forming a pulse which has two intensity maxima with lower peak intensity as shown in Fig. 5.4b). This can be understood as follows: We consider the two laser subfields at the frequencies ω_1 and ω_2 . They are infinitely long if we at first neglect their spectral width. They beat in *time* with the following periodicity (which defines the temporal spacing of the intensity maxima):

$$t_{max2} - t_{max1} = \frac{1}{\omega_2 - \omega_1}. \quad (5.5)$$

Since our pulses are short, we obtain only two such intensity peaks for $\Delta t = T/2 + NT$. The sequence of con- and destructive interference at a given time with respect to the center of the shaped pulse repeats of course in *time delay* with the periodicity of the laser cycle T . The beating of the driver pulse peak intensity with time delay causes the corresponding beating of the high-harmonic intensity. For time delays where the driver peak intensity is below a threshold no high harmonics can be observed, since the harmonic cut-off (the energy limit, up to where high harmonics are produced) depends on the driver (peak) intensity (see Eqs. 2.24 and 2.22). The beating of the driving subfields not only modulates the peak intensity but also leads to a significant longer driver pulse in the case where two maxima are produced.

It should be stated for clarity that the interference of both spectral parts is fully coherent. Thus, in case the shaped laser pulse has two pronounced intensity maxima and is even shaped like two separate pulses, it is wrong to assign the intensity maxima of the shaped pulse to the two time delayed spectral components, as it would be in case of an incoherent superposition of the subfields. Instead, the above mentioned characteristic temporal spacing of the inverse of the spectral-mean difference between the two spectral parts is obtained for a large range of time delays around the temporal overlap of the two spectrally separated subfields. In conclusion, we have identified the beating of driving subfields as a mechanism which strongly modulates the driver peak intensity, the number and temporal position of the intensity maxima and the duration of the shaped driver pulse. As we will see, this has major further impacts on HHG besides the harmonic intensity modulation.

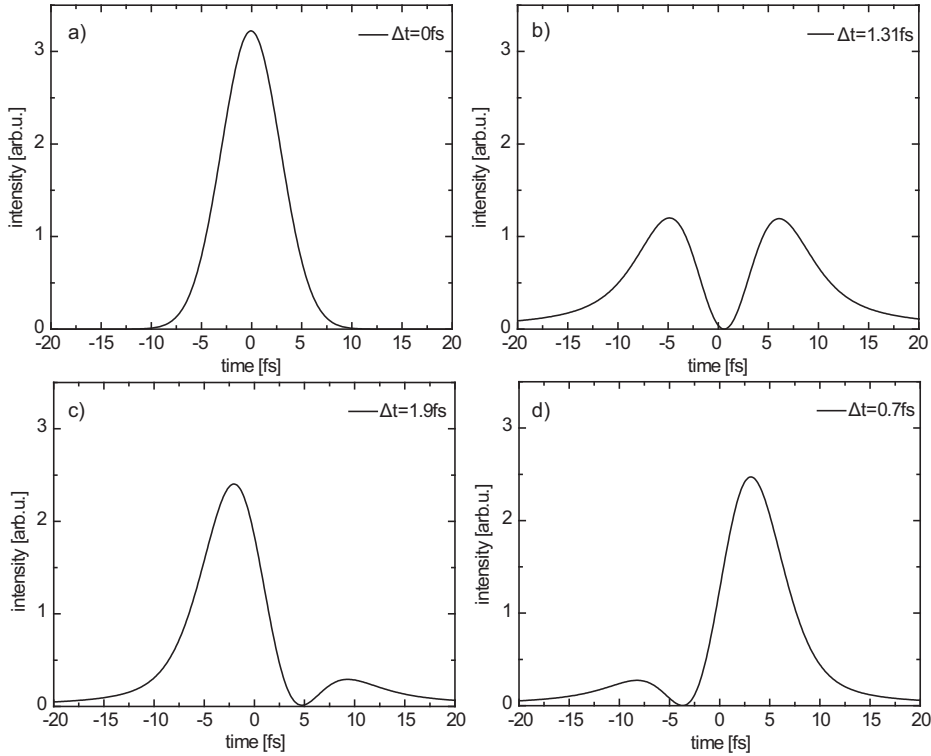


Figure 5.4: Beating of the driving laser field in time due to the interference of the two subfields (simulation results). A time delay Δt is introduced between the two symmetric halves of a Gaussian shaped laser spectrum centered around 780 nm. Intensity profiles of the shaped driving laser pulses for the following time delays: a) $\Delta t = 0$ fs. b) $\Delta t = 1.31$ fs. c) $\Delta t = 1.9$ fs. d) $\Delta t = 0.7$ fs.

5.4.3 Energy Tuning of the High Harmonics

5.4.3.1 Experimental Evidence

Besides the harmonic intensity beating, we observe in Fig. 5.3b) a pronounced tuning of the energy of the high harmonics as a function of the time delay between the two asymmetric intense subfields with the split spectrum as previously depicted in Fig. 5.3a). The energy tuning occurs both on the short (subcycle) time-delay scale, and on the longer scale given by the temporal overlap of the two subfields. A tuning of the energy of high harmonics in general has previously been observed e.g. introduced by a variation of the driver wavelength, by chirping the driver field or by moving the focus position [187].

5.4.3.2 Mechanism and Model

To explain this energy tuning capability and to retrieve its physical mechanism we developed the following model: It is known that the instantaneous frequency of a pulse can change with time throughout the pulse. The instantaneous frequency is given as the derivative of the time-dependent phase:

$$\omega(t) = \dot{\phi}(t). \quad (5.6)$$

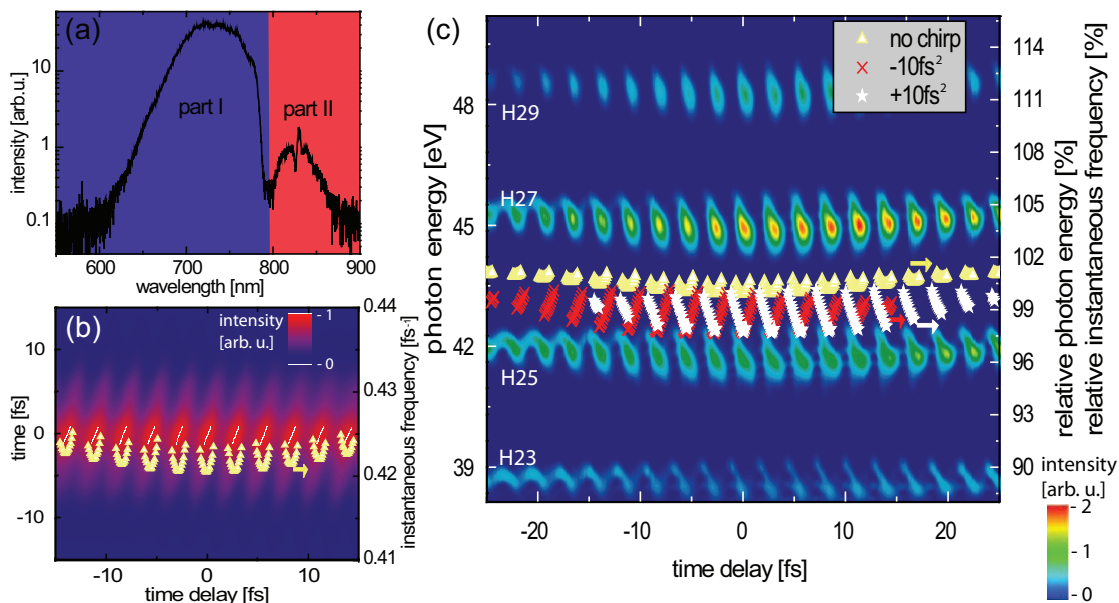


Figure 5.5: HHG energy tuning and mechanism with an asymmetric energy-split spectrum (experimental results, from [158]). An asymmetric cut of the spectrum at 795 nm leads to a pronounced modulation of the instantaneous frequency at the peak of the driving laser field and thus to an attosecond-delay-dependent energy modulation of the high harmonics. a) Measured split spectrum of the driving laser field. b) Intensity of the shaped driving pulse dependent on time and time delay between the two spectral parts, and time-delay dependent modulation of the instantaneous laser frequency (yellow squares) at the intensity peaks (white lines) (simulation result). c) Measured energy modulation of the high harmonics compared to the relative modulation of the instantaneous laser frequency without chirp as in (b) (yellow squares) and for chirps of -10 fs^2 (red crosses) and $+10 \text{ fs}^2$ (white pluses). Excellent quantitative agreement is found, confirming atom-level HHG control even with weak ($\sim 1.7\%$ of strong-pulse energy) control fields.

We calculate the instantaneous laser frequency at the intensity maximum (white lines in Fig. 5.5b) dependent on the time delay between the two spectral parts (as measured, Fig. 5.5a) with the cut moved to 795 nm, since the energy tuning is most pronounced for an asymmetric split spectrum. Although the total energy of the second spectral part is much lower here than the first part ($\sim 1.7\%$) it has a strong impact on HHG due to electron-kinetic heterodyning. As a model approximation, we assume that HHG occurs predominantly at the intensity maximum of the pulse. This is justified as the highest ionization rates, leading to the strongest emission of attosecond pulses, occur near local temporal intensity maxima. The instantaneous driver frequency at the peak of the pulse (yellow triangles in Fig. 5.5b) thus changes with time delay. In Fig. 5.5b) the temporal intensity profile of the shaped pulses is shown in color scale. The relative change of the measured harmonic energies and its dependence on the time delay (Fig. 5.5c) matches both qualitatively and quantitatively the relative change of the simulated instantaneous

laser frequency at the intensity peaks considering a chirp of $+10 \text{ fs}^2$ of the full laser pulse, which is assumed to have been present in the experiment. We were not able to measure the absolute amount of the residual chirp of the driving pulses at the interaction region. Therefore, the $+10 \text{ fs}^2$ chirp value was used as a single fitting parameter. The qualitative and quantitative agreement between experiment and model results supports the overall validity of the model. We thus find the change of the instantaneous laser frequency near the intensity maxima of the laser field to be the main control mechanism and physical picture behind the experimentally observed energy modulation of the high harmonics.

Let us have a closer look at some details behind the results presented in Fig. 5.5c). In the following, we restrict ourselves to the three time delays -0.96 fs , -0.48 fs and 0 fs . The minus sign means that the visible part (VIS) arrives before the near infrared (NIR). Fig. 5.6 shows the shaped driver pulse (red lines) and the instantaneous frequency (black line), with the chirp of $+10 \text{ fs}^2$ taken into account in the simulation. A relative frequency decrease of -1.5% at the peaks of the driver field is calculated within in the selected time-delay range. The resulting energy tuning ΔE of the n th harmonics then given by:

$$\Delta E = n \cdot \Delta \omega \quad (5.7)$$

We thus find that the harmonic order n amplifies a relatively small change of the instantaneous driver frequency to a large energy-tuning range of the harmonic photon energy, in our case to a modulation by 35-44% of the fundamental laser field photon energy ω , depending on n .

5.4.4 Fractional High-order Harmonic Combs

We now move the spectral-cut position more towards the center of the spectrum. The split spectrum with the cut now at 758 nm is displayed in Fig. 5.7b), while the measured high harmonics are shown as a function of the time delay in Fig. 5.7a). For the case of destructive interference of the two spectral sub-fields at the center of their respective temporal field profiles, the peak intensity of the synthesized light fields is too low to generate intense high-order harmonics. Instead, fine comb-like structures of fractional (non-integer) harmonics appear in the spectrum at energies below 44 eV . Superimposed to the usual harmonic modulation with an energy spacing of 2ω we see an about 10.4 times faster modulation in energy (see Fig. 5.7c).

With the intensity beating picture of the driver laser field at hand (see section 5.4.2), the generation of fractional harmonics can now easily be understood: The interference of the two spectral parts of the driving laser field leads to a beating in time with a beating period which is the inverse of their frequency difference (see Eq. 5.5). At time delays corresponding to destructive interference an intensity minimum is created at the center of the pulse, leading to two intensity peaks spaced about 5.2 laser cycles (Fig. 5.8). The intensity at these two peaks is still high enough to generate attosecond pulse trains (APTs) with energies up to 44 eV , on the other hand the intensity is low enough that the plasma density stays low over many cycles. This enables phase matching at both intensity peaks of the driving laser field such that two interfering APTs are generated, which are spaced in time by about 5.2 laser cycles. The half laser-cycle spacing of the attosecond pulses

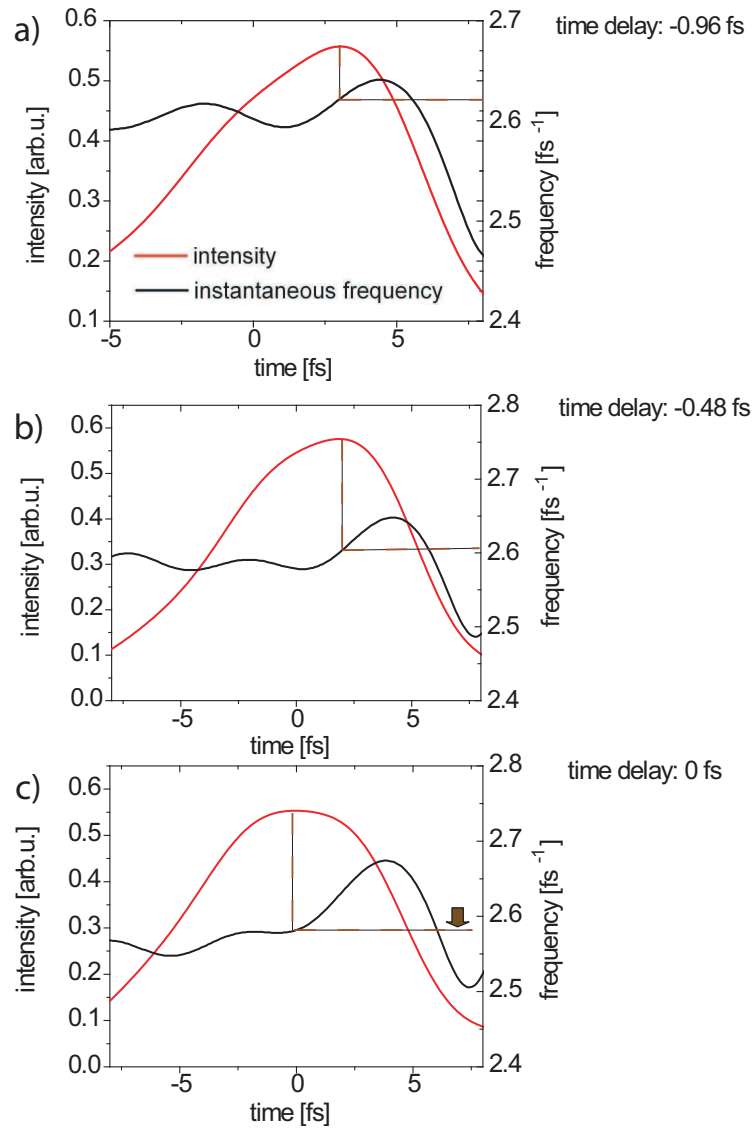


Figure 5.6: Simulated intensity profiles of split-spectrum shaped driver pulses (red lines) and instantaneous laser frequency (black lines) for the time delay -0.96 fs (a), -0.48 fs (b) and 0 fs (c). A decrease of the instantaneous frequency at the intensity maxima from 2.62 to 2.582 fs^{-1} results in an energy tuning of up to 0.7 eV after n -fold magnification by the harmonic order n . For the calculation of the shaped pulses the residual spectral phase after dispersion compensation (see Fig. 5.2) was taken into account.

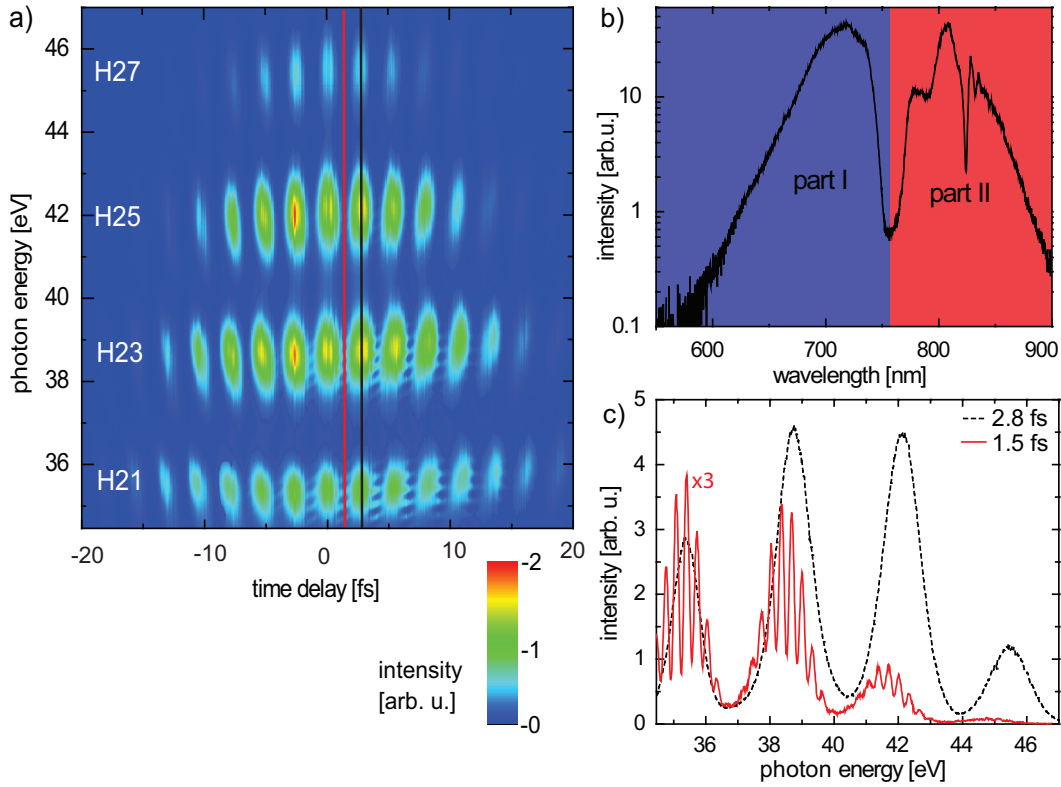


Figure 5.7: Generation of fractional-harmonic combs by split-spectrum control of high-harmonic generation (experimental results, from [158]). a) Measured spectrum of high harmonics dependent on the time delay between the two spectral ranges indicated in (b). b) Broadband split spectrum measured after the pulse shaper. c) Spectrum of conventional odd-integer harmonics at time delay 2.8 fs and fractional (non-integer) high harmonics at time delay 1.5 fs (intensity magnified by a factor of 3).

within the pulse trains leads to the well-known two-omega spacing of the harmonics. The additional interference between the two pulse trains leads to the faster modulation with an energy spacing of about $2\omega/10.4$, which is the inverse of the 5.2-cycle spacing of the pulse trains. In contrast to this, for time delays with constructive interference only a single most intense peak of the laser intensity is created in the pulse, resulting in only one APT and the commonly known high harmonics as arising from a single pulse train. An interesting property of the set of shaped driving pulses is the controllability of the relative intensities of the two subpulses produced as a consequence of the temporal beating of the two spectral sections (see Fig. 5.9). As a consequence, the relative intensity of the two attosecond pulse trains, one produced at each peak, can be arbitrarily set. A little higher peak intensity at the second peak can hereby compensate for a reduced phase-matching efficiency resulting from the increased number of ionized atoms at the second peak. In section 5.5.4 it will be studied how the controllable relative peak intensities can be used to create highly modulated fractional high-harmonic spectral combs which have a near-perfect contrast ratio between peaks and valleys of the interference pattern. In Fig. 5.9 the residual spectral phase after the dispersion compensation as given in Fig. 5.2 was taken into account. A small time delay between the spectral sections then compensates best

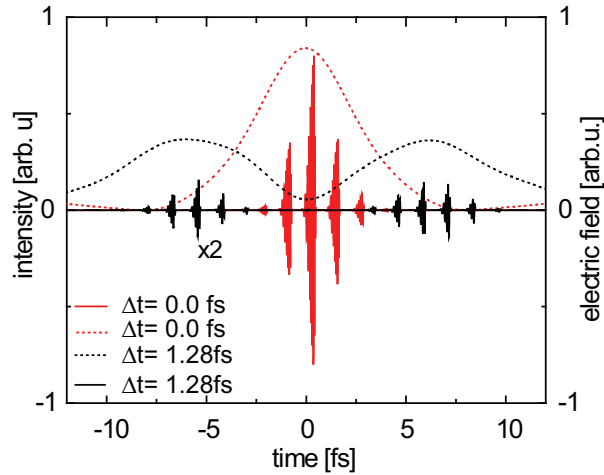


Figure 5.8: Mechanism of fractional-harmonic comb generation: Double attosecond pulse train generation (simulation results, from [158]): Shaped electric driving field intensity (dashed lines) and attosecond pulse trains (solid lines) for zero time delay (red lines, constructive interference of the two fundamental spectral parts at time 0) and for the time delay 1.28 fs (black lines, destructive interference at time 0). Two interfering attosecond pulse trains are generated in the latter case leading to deeply modulated fractional harmonics.

for this residual spectral phase. As a consequence the time-delay positions are shifted at which the best-balanced (or worst-balanced) intensity ratios are given (compared to Fig. 5.8 and Fig. 5.10).

5.4.5 Comparison to Simulations

In this section, we compare our measured data with numerical results. We consider the same laser spectrum as in the experiment with the spectral cut at 758 nm as shown in Fig. 5.7b) and a laser peak intensity of 0.44 PW/cm² at zero time delay corresponding to the experiment. The spectrum of harmonics is depicted in Fig. 5.10a). As in the experiment, a beating of the harmonics occurs as a function of time delay and deeply modulated fractional-harmonic combs are observed for time delays corresponding to destructive interference of the subfields at time 0 fs. The fractional harmonics in Fig. 5.10b) have an energy spacing of 0.31 eV corresponding to a 13.3 fs (5.4 cycle-) spacing of the two APTs. This compares well to the calculated the 5.2-cycle spacing of the pulse trains in Fig. 5.8. By virtue of the excellent qualitative agreement, we thus confirm the origin of the observed HHG spectral control clearly as a microscopic phenomenon, i.e. directly coherently controlling the higher-order emission dipoles caused by recolliding electrons of each of the atoms in the interaction region. We see that the fractional-harmonic combs can be fully modulated (e.g. for $\Delta t = 1.28$ fs) and range continuously over a number of harmonic orders, yet additionally modulated with the regular 2ω -periodicity of the odd harmonics.

In the above-shown simulation, where the CEP is fixed in contrast to the experiment, we see that the odd harmonics show subcycle time-delay resolved structures. They split up

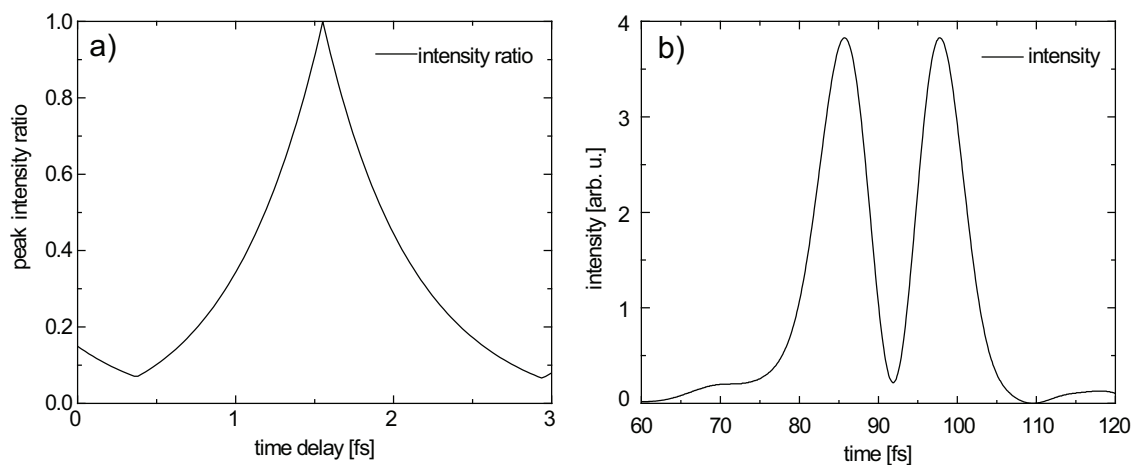


Figure 5.9: Generation of two equally intense attosecond pulse trains by coherent control of the peak intensity ratio of the driving subpulses (from [158]). a) Intensity ratio of the two most intense maxima of the shaped driving laser pulse dependent on the time delay. Simulation for the measured split-spectrum displayed in Fig. 5.7 including the residual spectral phase after the dispersion compensation given in Fig. 5.2. b) Shaped driving laser pulse with two equally intense subpulses at time delay 1.55 fs.

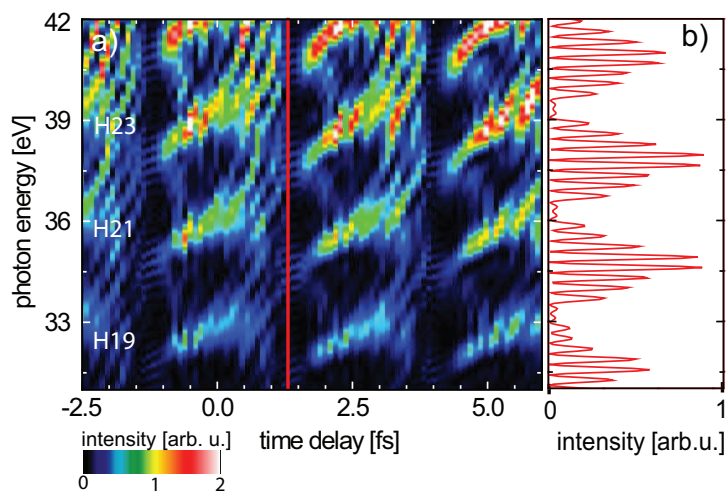


Figure 5.10: Generation of a deeply-modulated comb of fractional harmonics (simulation results, from [158]). a) Simulated harmonic spectra dependent on the time delay between the two spectral parts for the same settings as in Fig. 5.8. b) Spectrum of a fractional-harmonic comb with a high peak-to-valley contrast for the time delay of 1.28 fs in (a) (red line).

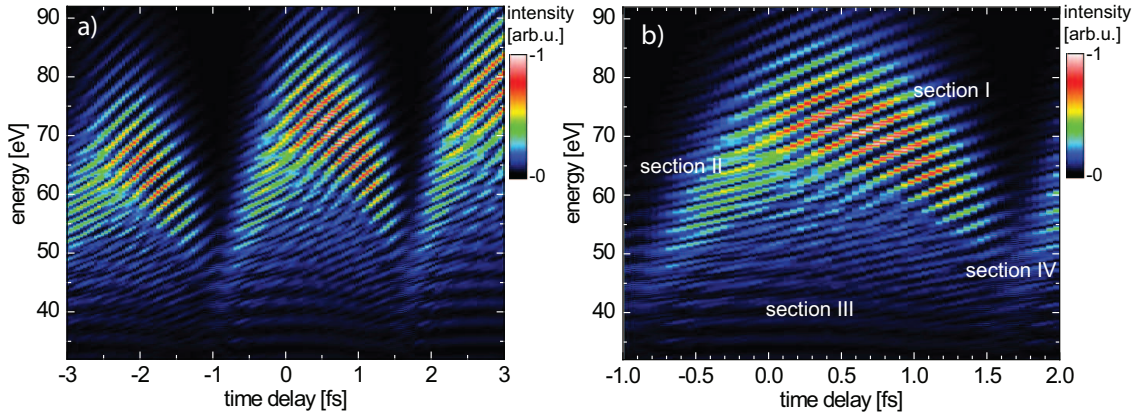


Figure 5.11: Rapid subcycle time-delay dependence of the high-order harmonics (simulation result). a) Simulation of the time-delay dependent high harmonics for the measured split spectrum displayed in Fig. 5.7 including the residual spectral phase after the dispersion compensation as shown in Fig. 5.2. In contrast to the previously-discussed experiment, the CEP of the driver pulses was fixed. b) Enlargement of a) revealing different patterns of harmonics. In section I the energies of the odd harmonics tune rapidly within few attoseconds of time delay over a large range of more than 10 eV for most of the harmonics. In section II even and odd harmonics appear, while in section III the substructures smear out. In section IV the fractional-harmonic combs are observed.

into finer lines, which strongly tune with the time delay. To resolve these tunings we repeat the simulation with a finer time-delay resolution $\delta t = 50$ as $\approx T/50$. Fig. 5.11a) displays the simulation in a larger energy range and Fig. 5.11b) is the enlarged time-delay range -1 fs to 2 fs, where we divide the spectrum into sections where we observe different harmonic patterns. Section I covers the higher energies and shows the most intense harmonics: odd harmonics spaced by 2ω in energy. Interestingly they tune very fast with the time delay and span continuously over a large energy range. Following such a harmonic to smaller Δt (lower energies), we observe a splitting of the odd harmonics. Thus in section II we identify even and odd harmonics with a 1ω -energy spacing. The splitting occurs at much higher energy for smaller Δt within the beating cycle T . At even lower energies (section III) the harmonic intensity contrast between the individual lines, which tune rapidly with time delay, decreases. Instead the lines smear out and form regular high harmonics, which vary only slowly with the time delay. In section IV the fractional-harmonic combs are generated as described earlier. The overall subcycle time-delay shape is as follows: At high energies, there is only a harmonic signal for time delays where the two subfields interfere mainly constructively at the center of the driver pulse, thus for a smaller time-delay range. In contrast, the harmonics are produced at almost all time delays at lower energies. The reduced time-delay dependence of the lower-energy harmonics results from the fact that here independently of the pulse shape (governed by Δt), the intensity is always high enough that every half-cycle an attosecond pulse is produced.

In the experiment we did not resolve the subcycle tuning of the harmonic energies with the extremely small time-delay changes. We did not have the time-delay resolution of 50 attoseconds as in the simulation. Though the time-delay step size was 67 as, the effective capability to resolve precise time-delay changes can be limited by other factors

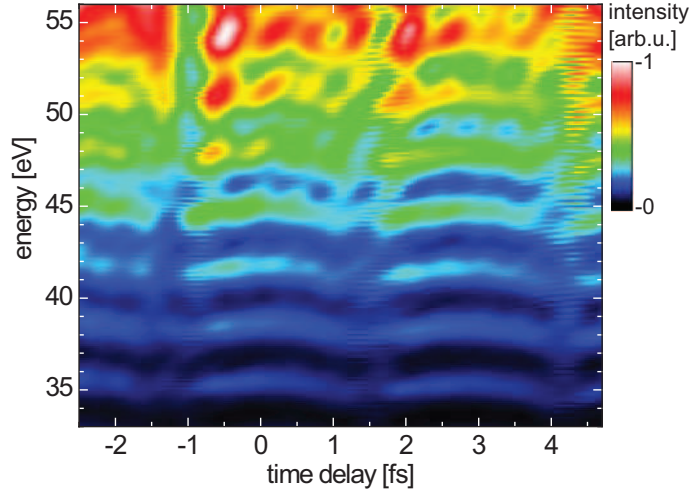


Figure 5.12: Simulated harmonic spectrum with a time-delay resolution of 250 as, corresponding to the assumed experimental interferometric stability between the two driver subfields. A Fourier filter was applied to the simulation in Fig. 5.11 to match the time-delay resolution. While the rapid subcycle energy tuning is smeared out, the fractional-harmonic combs are clearly visible.

as well. Among these are the surface quality of the mirrors, which is $\lambda/10$ in our setup, the interferometric stability of the pulse shaper, spatial effects as spatial chirps and spatial (vertical) averaging over the XUV beam on the camera chip. The effective time-delay resolution is studied in section 5.5.6. We have chosen a reasonable effective resolution of $\Delta t = T/10 \approx 258$ as to Fourier filter the simulated time-delay scan, removing higher frequencies with the time delay. The result is depicted in Fig. 5.12 and compares well with the experimental data. The very fast subcycle energy tunings with Δt are smeared out, while the fractional-harmonic combs are clearly visible.

The origin and mechanism behind the rapid subcycle energy tuning of the high harmonics in Fig. 5.11 is different from the energy-tuning mechanism described in section 5.4.3 and must not be confused with it. While the latter one results from the change of the instantaneous frequency at the intensity maximum of the shaped driver pulse, the first one is an effect of the stabilized CEP. Even a small change of the time delay Δt changes the carrier-envelope phase of the *shaped* driver pulse ϕ_0^{shaped} . The first reason is that the application of a time delay moves the envelope of the shaped pulses in time with respect to the stable carrier by

$$\Delta t^{envelope} = const(\omega_{cut})\Delta t \quad (5.8)$$

with a constant $0 < const(\omega_{cut}) < 1$ which depends on the spectral-cut position. This would induce a change of ϕ_0^{shaped} , which would be too small to explain the rapid harmonic-energy tuning, since it would be $< 2\pi$ for $\Delta t = T$:

$$\Delta \phi_0^{envelope} = \omega \Delta t^{envelope} \quad (5.9)$$

Instead, additionally, the shape of the envelope is drastically altered due to the beating of the subfields. This leads to a fast shift of the temporal peak position of

$$\Delta t^{peak} = \Delta t^{envelope} + f\left(\frac{\Delta t}{T}\right) \frac{1}{\omega_2 - \omega_1} \quad (5.10)$$

and thus to a rapid change of the phase between carrier and envelope at the highest intensity maximum of the shaped driver pulse:

$$\Delta\phi_0^{shaped} \approx \omega\Delta t^{peak}. \quad (5.11)$$

The definition of ϕ_0^{shaped} at the highest envelope maximum is suited for our application because the regular high harmonics are predominantly generated close to this intensity maximum. A numerical measure for ϕ_0^{shaped} is the temporal phase at this envelope maximum. The shaping-induced change of ϕ_0^{shaped} is illustrated in Fig. 5.13. The electric field (solid line) and the pulse envelope (dashed line) is calculated for a Gaussian shaped driver spectrum centered around 750 nm and a fixed CEP $\Delta\phi = 0$. A time delay Δt is applied for the half of the spectrum with the higher frequencies. Starting with a cosine-like pulse at $\Delta t = 0$ fs the effective CEP ϕ_0^{shaped} is altered drastically as a function of the time delay, which shifts the peak position in time. The peak position is marked with the black arrow compared to the original time zero position, which is indicated with the blue arrow. Already at a time delay of about 0.75 fs a roughly cosine-like pulse is obtained again as can be seen in Fig. 5.13d).

Thus, we have identified the fast shift of the temporal peak position of the shaped driver pulse to rapidly change the newly defined effective CEP of the shaped driver pulse. Since the energy of the high harmonics is tuned by the CEP of the driver field, as we have seen in chapter 3, this change of the ϕ_0^{shaped} then causes the rapid subcycle energy tuning, which we showed in the numerical simulation (Fig. 5.11). While we cannot resolve these rapid subcycle energy tunings with the time delay, we will at least give experimental evidence for the energy tuning with the CEP in section 5.5.2. In the following, we show that the rapid subcycle energy tunings are a CEP effect. To that end, we add up ten simulated harmonic spectra with the CEP ϕ_0 (not ϕ_0^{shaped}) of our laser field given by 0, 0.1π , 0.2π , ..., 0.9π . As can be seen in Fig. 5.14a) the rapidly tuning harmonic substructures are almost completely smeared out and instead form odd harmonics, which vary only slowly with the time delay. The fractional-harmonic combs are still clearly visible. Their peak-to-valley intensity contrast is lowered compared to the CEP-stable simulation as can be seen for the time delay 1.62 fs in Fig. 5.14b).

5.4.6 Time-delay Asymmetries and Spectral Broadening

The spectra of high harmonics displayed as a function of the time delay are not symmetric with respect to a reversion of the time delay (though there might be symmetric patterns in some cases). It matters for the driver pulse shape and for HHG, if the visible or the NIR part of the spectrum comes "earlier" (this expression can be misleading, as both fields are overlapping in time and form a coherent superposition). We observe in Fig. 5.7 that the fractional-harmonic combs are mostly produced around positive time delays, while the most intense harmonics are produced at earlier time delays. Possibly, an ionization gate anticipated the generation of a second attosecond pulse trains at earlier time delays. More likely, the time-delay asymmetry results from the asymmetric shape of the two subfields in the time domain, which in turn originates from a non-perfectly flat spectral phase and the non-Gaussian spectral shape of two driver subfields. Theoretically, fractional harmonics could also be generated at much larger positive or negative time delays, if the intensity

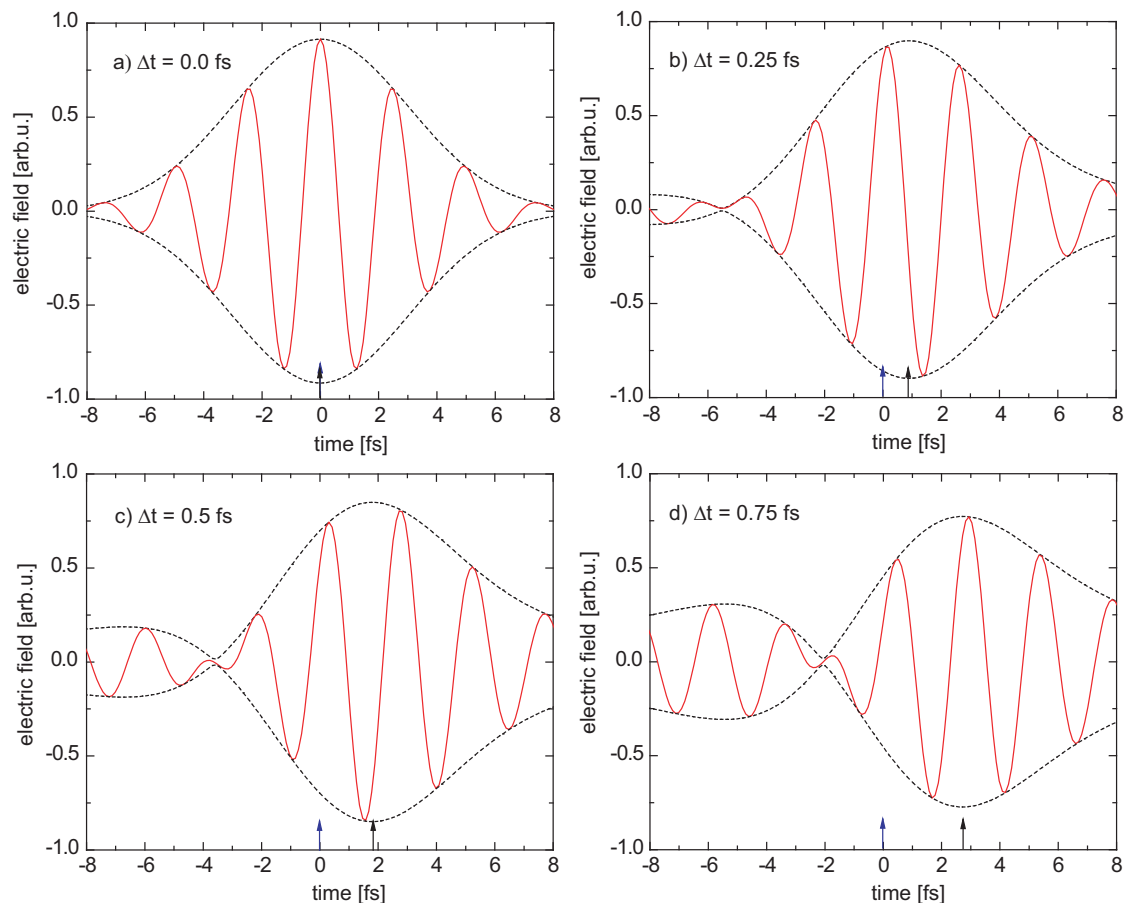


Figure 5.13: Shaping-induced variation of the effective driver-pulse CEP (numerical results [188]). The time-delay controlled shaping of the driver pulse shifts the peak position of the pulse envelope (dashed line) in time (black arrows) compared to the original peak position (blue arrows) while the electric-field carrier (solid line) is locked. This strongly modulates the effective CEP, which is defined at the highest intensity maximum. While a time delay of 0 fs causes a cosine-like pulse (a), a time delay of 0.25 fs produces almost a minus sine-like pulse (b), the pulse at $\Delta t = 0.5$ fs comes close to a minus cosine-like pulse (c) and $\Delta t = 0.75$ fs obtains again a roughly cosine-like pulse (d). The temporal phase at the envelope peak gives an effective CEP $\phi_0^{shaped} = 0$ in (a), $\phi_0^{shaped} = 0.64\pi$ in (b), $\phi_0^{shaped} = 1.2\pi$ in (c) and $\phi_0^{shaped} = 1.84\pi$ in (d).

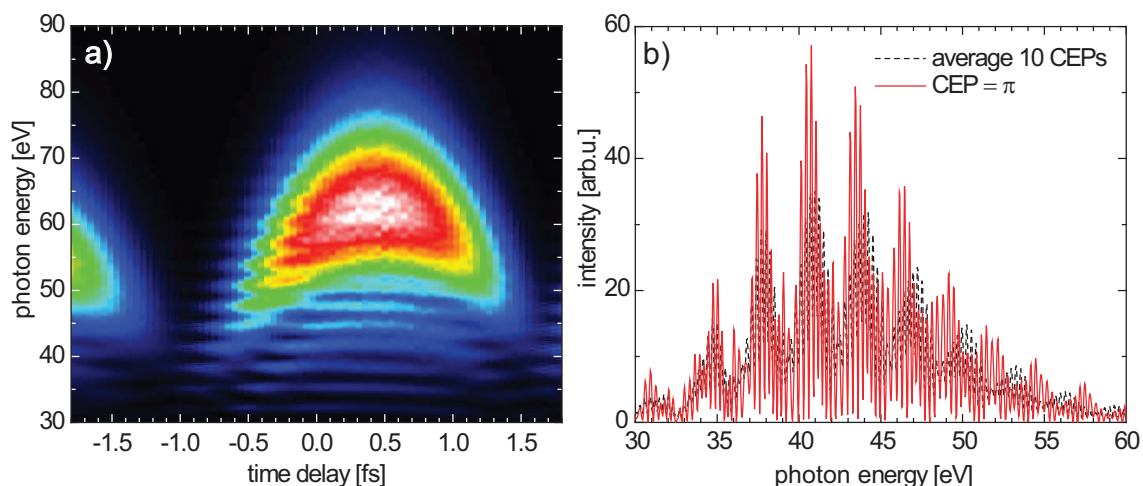


Figure 5.14: Influence of the CEP-stabilization (simulation results). a) Sum of ten harmonic spectra generated with $\phi_0 = 0, 0.1\pi, 0.2\pi, \dots, 0.9\pi$. Taking the sum of harmonic spectra produced with different CEPs smears out the rapid subcycle harmonic-energy tuning and results in the regular odd harmonics which vary only slowly with the time delay. b) Fractional-harmonics comb spectra at the time delay 1.62 fs. The sum of harmonic spectra with different CEPs as in a) (dotted line) is compared to a spectrum produced by a CEP-stabilized driver field $\phi_0 = \pi$ (solid line). The latter produces a much higher comb contrast.

of the subfields is well-balanced and compensates for ionization as well. Even if the subfields do not overlap anymore, the full coherence of the two attosecond pulse trains would be retained and the fractional harmonics would form finer and finer combs as the temporal spacing increases with the time delay.

Besides the time-delay asymmetry we observe in Fig. 5.15 that the measured high harmonics are spectrally broadened, when the temporal overlap of the subfields is large. This means that the number of attosecond pulses which contribute to HHG is reduced here to about two or three. An explanation could be that at the overlap of both subfields the peak intensity of the driving laser pulse is much higher. The enhanced ionization increases the plasma density within a few half-cycles to a value where the XUV- and NIR-pulse phases propagate no longer with the same speed. Thus the XUV-emission adds no longer up constructively and the phase-matching condition (see section 2.5.1) is no longer fulfilled such that attosecond pulse production is limited to few half-cycles. Thus we have found an experimental indication that the number of attosecond pulses is controlled by the time delay, which steers the ionization phase-match gating [81] as described before. This is among the observed effects in this chapter the only one that originates from the macroscopic aspects of HHG.

5.4.7 Effects of the Generalized Kinetic-Heterodyne Mixing of Laser Subfields

In sections 5.4.3 and 5.4.4 we already studied HHG at two different cut-positions of the driving split-spectrum: A spectral cut located close to the edge of the fundamental spec-

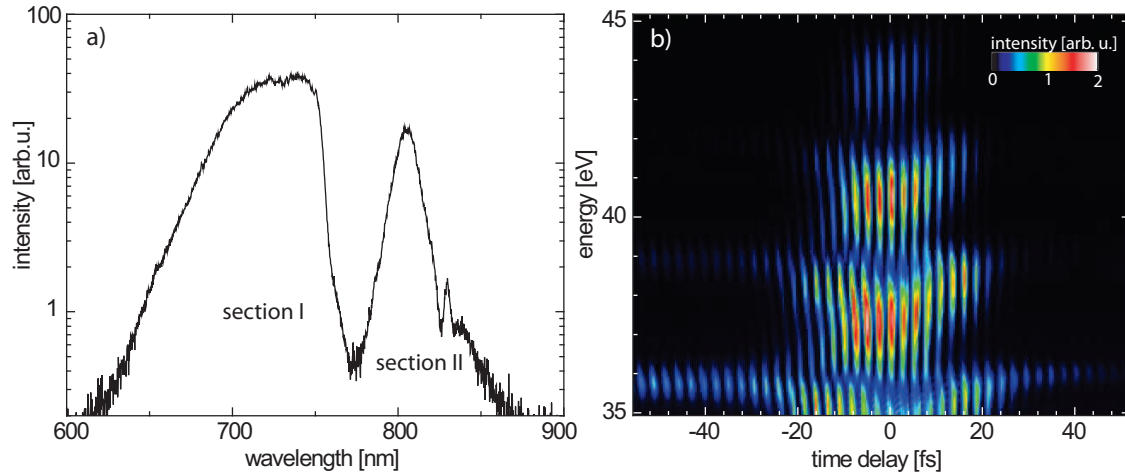


Figure 5.15: Split-spectrum controlled HHG in the asymmetric-cut regime (experimental result). a) Driver spectrum with 12.3% of the total pulse energy in section II. b) High-harmonic spectrum as a function of the time delay between the spectral sections. A strong beating of the harmonic intensity is visible besides a spectral broadening and energy modulation of the high-harmonic lines.

trum and later a more symmetric cut with an energy ratio between the two sections of 1.53:1. While the focus in these sections was on the explanation of the observed effects (energy tuning in the first case, the generation of fractional-harmonic combs in the second case), the influence of the spectral-cut position as an adjustable control parameter in split-spectrum controlled HHG will be studied more systematically in this section. For this purpose, we at first examine how the beating of the driving laser field is affected by the cut position. While the shape of the driver pulse after the pulse shaper is the same (unshaped) profile at $\Delta t = 0$ fs for all cut positions, it strongly depends on the cut position for other time delays, e.g. for $\Delta t = 1.25$ fs as illustrated in Fig. 5.16.

The simulations reveal that the smaller part of the Gaussian spectrum needs to have a fraction of more than 11.7% of the total intensity to produce driver pulses with two intensity maxima (see Fig. 5.16). The latter is a requirement for the generation of fractional-harmonic combs. But also for fractions smaller than 11.7% the pulse shapes (both intensity and the electric field) are strongly modulated with the time delay. There is a large impact on the peak intensity. But also the instantaneous laser frequency and the peak position in time are modulated (increasingly with the intensity fraction in this regime). The remarkable impact of the lower-intensity subfield on HHG is a consequence of the generalized principle of kinetic-heterodyne mixing of laser subfields as described in chapter 4. Due to this principle the cut position can be chosen within the almost entire range of the driver spectrum and still a remarkable controllability of HHG (e.g. the pronounced energy tuning and the beating of the harmonic intensity with the time delay) is retained. By the experimental evidence of these observed control effects in Fig. 5.5, where the fraction of the second spectral part was only 2% of the total energy, we can validate the generalized principle.

As a function of the energy fraction of the smaller spectral section (which is connected to the spectral-cut position), we can distinguish three different regimes, which have a smooth

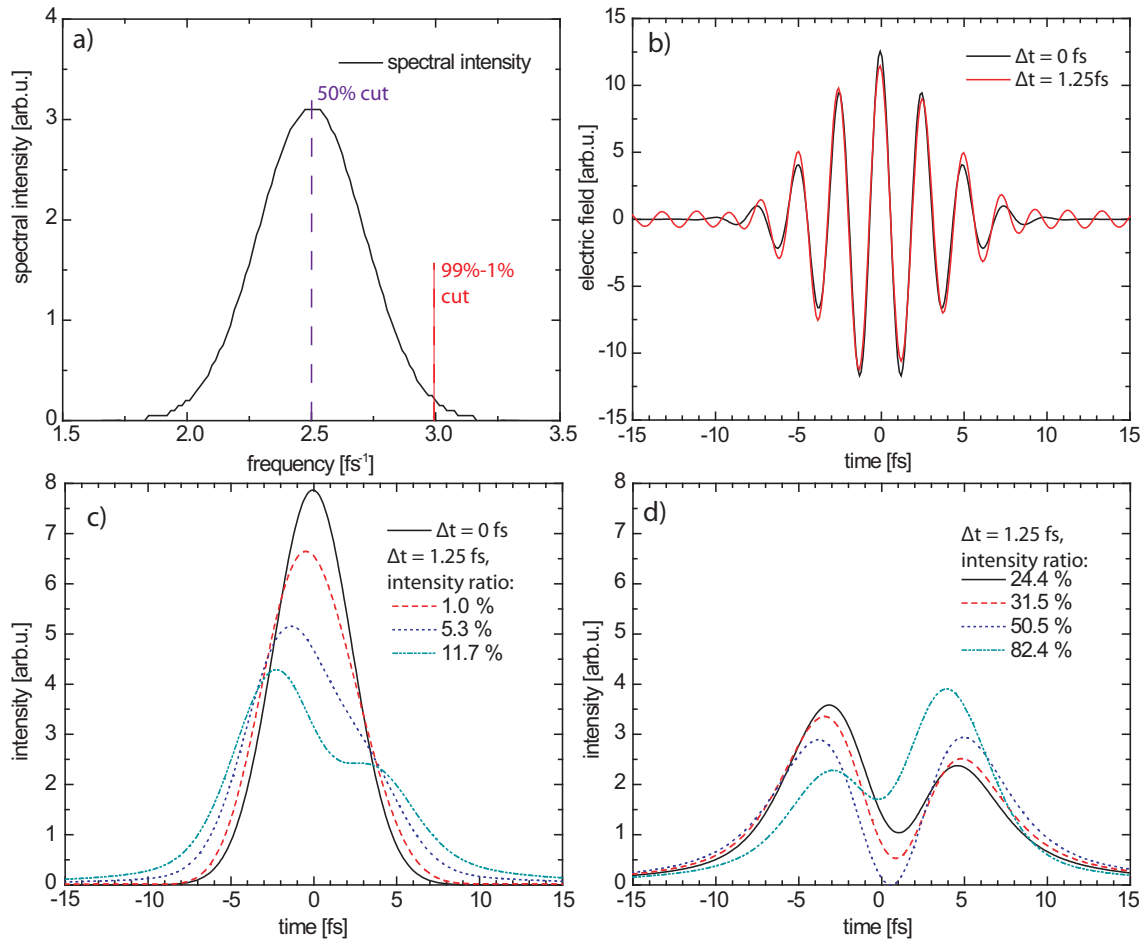


Figure 5.16: Dependence of the beating of the two driving laser subfields on the spectral-cut position and effect of the generalized kinetic-heterodyne mixing (simulation results). Even if only a very small fraction of the laser spectrum is time delayed, it reshapes significantly the driver pulse. a) Spectral intensity of the driver field. b) Electric field for 0 fs (black line) and 1.25 fs (red line) time delay, where the driver spectrum is asymmetrically cut in a way that the second spectral part contains only 1% of the total intensity. c) Modulated pulse shapes at the time delay 1.25 fs for different fractions of the second-section intensity: 1% (dashed line), 5.3% (dotted line) and 11.7% (dash-dotted line) and comparison to 0 fs time delay (solid line). d) Pulse shapes for spectral fractions of 24.4% (solid line), 31.5% (dashed), 50.5% (dotted) and 82.4% (dash-dotted line). The pulse shape exhibits two intensity maxima at $\Delta t = 1.25$ fs if the smaller spectral section contains more than 11.7% of the total intensity.

transition between each other:

- $<2\%$: Kinetic-heterodyne mixing regime. Mainly the intensity beating of the HHG and the energy tuning of the odd harmonics are observable here. The controllability is enabled by the principle of generalized kinetic-heterodyne mixing of laser subfields. High harmonics can be produced for all time delays with a modulated cut-off energy.
- $\sim 2\text{-}25\%$: Asymmetric-cut regime. The intensity beating is increased and the high harmonics vanish every full cycle time delay in this regime. Additionally, the temporal driver peak position is increasingly modulated. We predict this to additionally cause strong, few-attoseconds time-delay dependent (rapid) harmonic-energy tunings. A second driver peak appears for a fraction $\gtrsim 12\%$, but its intensity is too low to generate an attosecond pulse train (APT) with a considerable intensity compared to the APT which is produced at the higher intensity peak. Thus the fractional-harmonic combs are not yet visible in the higher-energy range. The generation of fractional harmonics at lower energies depends on whether the phase-matching- and ionization gate is open sufficiently long (e.g. the driver intensity must not be so large that the ground state is mostly depleted, before a second APT can be produced).
- $25\text{-}50\%$: Central regime: The driver pulse becomes deeper modulated leading to a strong beating of the harmonic intensity with the time delay. The generation of intense fractional-harmonic combs at moderate harmonic orders is possible, while the instantaneous-frequency-driven harmonic-energy tuning is reduced in magnitude. In contrast, the rapid harmonic-energy tuning on few attoseconds time delay is very pronounced here. Ionization gating leads to a spectral broadening of the high harmonics when the subfields overlap extensively.

Fig. 5.15b) gives an example for a measurement of split-spectrum controlled high harmonics in the asymmetric-cut regime. 12.3% of the energy is in the smaller spectral section (see driver spectrum in Fig. 5.15a). As expected we see a pronounced beating of the harmonic intensity with the time delay with the period of the full laser cycle. We see fractional-harmonic combs only at lower energies and less intense compared to the odd harmonics. Special to this cut-position is that the energy of the odd harmonics tune widely here, for some time delays around (e.g. around -18 fs) even continuously over more than two harmonic orders. This was so far only observed in this scan and cannot be explained entirely by the presented energy tuning model based on the instantaneous frequency. The large energy modulation might instead originate from the rapid shaping-induced energy tuning. But since the CEP was not stabilized in the experiment the data have to be compared to simulations where like in Fig 5.14 the energy tuning is due to averaging effects qualitatively changed compared to the phase-stable simulations like the one in Fig 5.11. In the phase-averaged simulation there are as well energy modulations visible with the same periodicity with the time delay, but further investigations would be needed to exclude other possible explanations for the large experimentally observed energy tuning. Especially for the time delay around -15 fs, there seem to be local harmonic intensity maxima at different energies spaced by only 1ω instead of 2ω implying odd- and

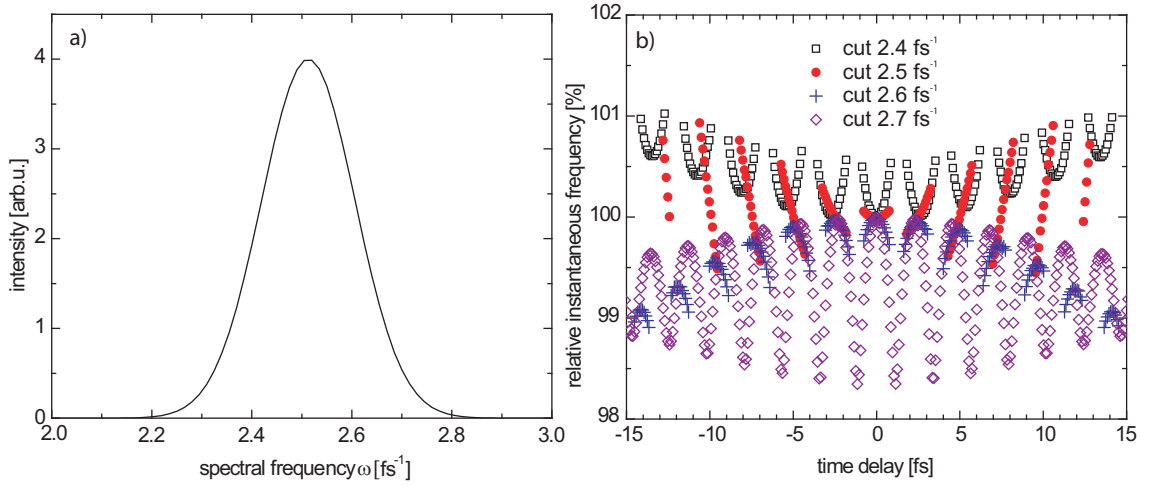


Figure 5.17: Spectral-cut position dependence of the high-harmonic energy tuning (simulation results). a) Intensity of Gaussian shaped driver spectrum centered around 2.513 fs^{-1} ($\cong 750 \text{ nm}$) used for the simulations. b) Relative change of the instantaneous laser frequency at the peak of the driver pulse as a function of the time delay between the spectral sections for a spectral-cut position of 2.4 fs^{-1} (squares), 2.5 fs^{-1} (red circles), 2.6 fs^{-1} (pluses) and 2.7 fs^{-1} (diamonds). The highly unbalanced spectral cut at 2.7 fs^{-1} causes the most-pronounced frequency modulations. The values are plotted only for time delays for which the driver peak intensity is strong enough to produce high-order harmonics.

even-order harmonic generation with peaks at different subcycle time delays compared to the odd harmonics.

To exemplarily quantitatively demonstrate the influence of the spectral-cut position on a single property of the high-order harmonics, we show how the energy tuning varies as a function of the spectral-cut position (see Fig. 5.17). We see that the energy tuning patterns turn upside down when the spectral cut is moved through the center of the Gaussian-shaped driver spectrum. The strongest energy tunability is given for an off-center spectral-cut position. In the simulations the relative change of the instantaneous frequency is displayed for time delays, where the peak intensity is above 0.013 a.u. The threshold is applied to meet the experimental situation, where a sufficient peak intensity is necessary to produce high harmonics in the measured energy range. For a spectral cut at the high-frequency wing of the spectrum (e.g. at 2.7 fs^{-1}), the instantaneous frequency at the driver peak is highest for zero time delay. When a time delay is applied the contribution of the high-frequency section can be only lowered, which "moves" the high frequencies out of the pulse or sets their phase into destructive interference with the main pulse, what both reduces the instantaneous frequency at the driver peak. The opposite result is obtained for a cut located at the lower-frequency wing of the driver spectrum. Here, a lower contribution of the lower spectral frequencies increases the instantaneous frequency at the intensity maximum. According to our model this change of the instantaneous frequency translates directly to a proportional change of the harmonic energies.

In conclusion, in this section we have performed remarkable control of HHG by only applying the split-spectrum time-delay control without CEP stabilization. Both experimentally and theoretically, we found a strong energy tunability of the harmonics, a beating of

the harmonic intensity, a controllability of the pulse number in the APT and the generation of fractional-harmonic combs. We explained the underlying mechanism for different relative segmentation scenarios (energy sharing) of the driver spectrum. In the next section we will refine the achieved control by including the CEP and later a temporal chirp of the driver field as further control variables.

5.5 CEP-stable Results

While in the last section the carrier-envelope phase (CEP) was not stabilized, we will now experimentally apply additional CEP control, to further enhance the controllability of HHG and to make use of the multidimensional (multi-parameter) control scheme, which we developed in chapter 4.

5.5.1 Time-delay Dependence

Fig. 5.18b) shows the odd harmonics and the fractional-harmonic combs as a function of the time delay between the split-spectrum sections given in Fig. 5.18a). The energy distribution between the spectral sections is about 1 : 1.4. The harmonic spectra look similar to the CEP-averaged case and again show the pronounced beating of harmonic intensity as well as the energy tuning with the time delay. Moreover, we observe the generation of fractional-harmonic combs here as well. Again the fractional harmonics are more intense at positive time delays (visible spectral section first), while for the odd harmonics it is the other way round. Note that the intensity in Fig. 5.18 is in log-scale to the basis 10. In total, by CEP stabilization the effects described in the last section are maintained, maybe even with a better subcycle time-delay precision. We find the following general fact advantageous for a precise control and optimization of different properties of the produced harmonics: As a function of the time delay the pattern repeats every full cycle but at the same time varies slowly from cycle to cycle. It varies furthermore differently for instance for the odd and fractional high harmonics. That finding will be applied in section 5.5.4, where we investigate the combs with an emphasis on the optimization of the fractional-harmonic combs.

We see in Fig. 5.18 that harmonics are generated also for time delays, where the temporal overlap between the two subfields is low (e.g. for $\Delta t < -25$ fs or > 25 fs). The hereby observed harmonic beating with time delay is again an effect of the kinetic-heterodyne mixing of the laser fields. In this case the more intense subfield is strongly modulated by the temporal wing or by subpulses of the delayed other subfield, whose temporal width of the electric field is much longer than its width in intensity. This explains as well why in all time-delay scans we see highly-modulated high harmonics for a significantly wider range of the time delays than given by the driver pulse duration (~ 10 fs).

Before we study the influence of a CEP variation, it shall now be explained how the time delay between the two subfields is derived. The relative time delay is given by the mirror position z , set by the piezo-controller: $\Delta t = \frac{\Delta z}{c} + \text{const.}$, where c is the speed of light and a positive Δt means the visible (VIS) part of the spectrum comes first. However, the

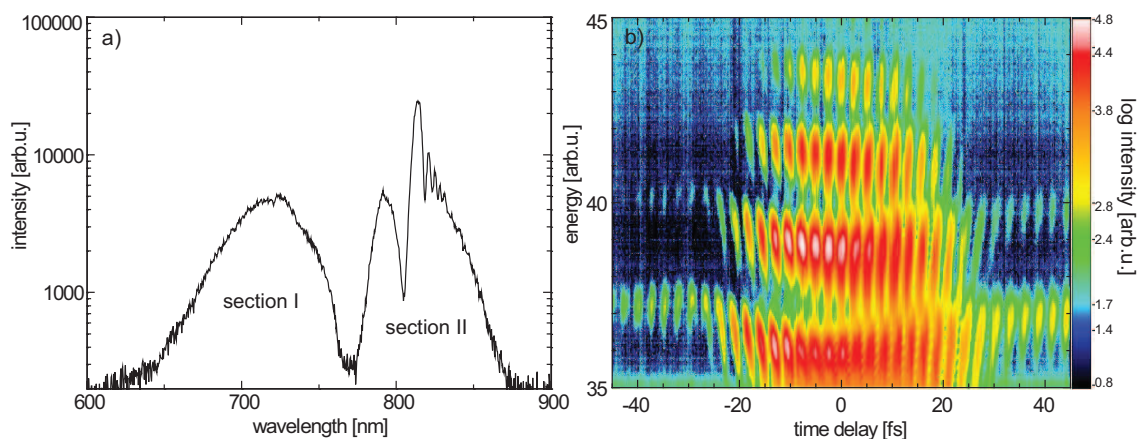


Figure 5.18: Split-spectrum controlled high harmonics as a function of the time delay for a phase-stabilized driver field (experimental results). a) Driver split-spectrum with the cut at 768 nm. b) Similar high harmonics and fractional-harmonic combs are revealed as in the CEP-averaged case. Low-intense odd high harmonics are produced and beat with the time delay for low pulse overlap as well (the color encodes the logarithm to the base 10 of the harmonic intensity). The latter finding results from the kinetic-heterodyne mixing effect for time-delayed laser fields.

absolute time delay has to be calibrated interferometrically. We use the fundamental laser pulse itself for this purpose and record a highly nonlinear response, which is the HHG in our case, as a function of the relative time delay. We do not choose the absolute time delay by comparison to simulation, as this way we can better test their validity. Instead we calibrate the absolute time zero from its effect on the cut-off harmonics. The highest harmonics are produced for the driver pulses with the highest peak intensity. This is given for an unshaped pulse with flat spectral phase, thus for $\Delta t = 0$. In the simulation considering the spectral phase after dispersion compensation the most intense driver pulse is obtained at $\Delta t \approx 0.4$ fs, because this small time delay compensates best for the non-perfect, but close-to-flat spectral phase after the dispersion compensation (see Fig. 5.2). We cannot determine the residual spectral phase with a precision better than in Fig. 5.2, but confirmed the influence to be small (see autocorrelation measurements in Fig. 2.9), which is why we neglect it. We estimate the error of the absolute time delay to be about one laser cycle T .

5.5.2 CEP Dependence

Having a phase-stabilized fundamental laser field, we now change ϕ_0 of the field before the pulse shaper and record the generated high harmonics spectra as a function of ϕ_0 . To study the influence of the CEP on the fractional-harmonic combs, we set the spectral-cut position to 770 nm and the time delay to a setting, where the fractional high harmonics are predominantly generated. As we can see in Fig. 5.19 the fractional-harmonic comb is produced for all CEPs ($0-2\pi$). While the shape of the comb is not affected by the CEP the spectrum is shifted in energy. The tuning of the energy of the individual fraction harmonics is linear with the CEP. Within a CEP-range of 2π they shift by twice the energy spacing between two subsequent comb lines. This can be understood as follows: While

the time delay between the spectral sections changes both the shape and the phase between the carrier and envelope of the shaped pulse at its most intense peak ϕ_0^{shaped} , the CEP of the fundamental field ϕ_0 only changes ϕ_0^{shaped} , but leaves the envelope of the shaped driver pulse constant. In simulations we find for $\Delta t = \text{constant}$:

$$\Delta\phi_0^{shaped} \approx \Delta\phi_0. \quad (5.12)$$

Since the temporal spacing of the intensity maxima of the shaped pulse and thus the temporal spacing of the two attosecond pulse trains is not affected by ϕ_0 the energy spacing of the fractional harmonics is not altered. A change of ϕ_0^{shaped} moves the electric field carrier underneath the envelope at both intensity peaks. This changes the energy and possibly also the intensity of the fractional high harmonics. The mechanism can be transferred from the energy-tuning with the CEP, which was studied in chapter 3. A change of $\Delta\phi_0^{shaped} = \pi$, achieved according to Eq. 5.12 by $\Delta\phi_0 = \pi$, leads to the same amount of the electric field and thus the same fractional-harmonic comb resulting in the observed periodicity with $\Delta\phi_0 = \pi$. The shift of the fractional-harmonic combs in Fig. 5.19 in energy implies that the spectral-phase difference (equals the CEP difference) between both produced APTs can be entirely set by the CEP. In chapter 4 the relative phase between the attosecond pulses was found to be influenced by the position within the pulse envelope (trailing edge or close to the peak). Here, we find a different behavior of the attosecond pulse phases at the first driver intensity maximum compared to the second maximum. These different behaviors could result from different plasma conditions or different single-atom trajectories for both APTs. While in chapter 4 we controlled independently the intensity ratio and spectral-phase difference between two attosecond pulses we now find the ability to perform the same control with two attosecond pulse trains.

The complementarity of the influences and control mechanisms of the CEP and the time delay is an important finding towards the independent control of HHG with these two control parameters. Indeed we experimentally find that two properties of the generated high harmonics (in Fig. 5.19 e.g. the peak-to-valley intensity contrast of the comb lines on the one hand, and the peak positions in energy of the fractional harmonic lines on the other hand) can be fully controlled by just the two parameters Δt and ϕ_0 . This fulfills the conditions of the definition of independent control as defined in chapter 4. In section 5.5.4 we will make use of the independent controllability to optimize the fractional-harmonic combs. Thereafter the independence and the influence of the individual control parameters with inclusion of all control parameters will be further studied in section 5.5.7.

5.5.3 Influence of Temporal Chirps

In this section the influences of temporal chirps of the laser field before the pulse shaper on the split-spectrum controlled HHG are analyzed. Such chirps (defined by the group delay dispersion) temporally broaden the driver laser pulse and additionally change the instantaneous frequency of the electric field of the pulse. This change of the instantaneous frequency adds onto the modulation induced by the split-spectrum pulse shaping itself, whose dependence on the time delay causes the energy tuning of the high harmonics as demonstrated in section 5.4.3. We study the influence of the temporal chirp for the driver spectrum as depicted in Fig. 5.20a), where the intensity in the second spectral

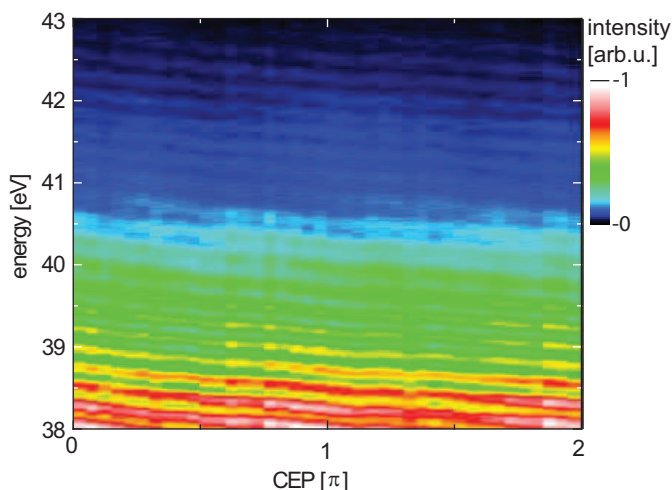


Figure 5.19: Energy tunability of the measured fractional high-harmonic comb as a function of the CEP of the fundamental pulse (experimental result). The energy of the individual peaks shift linearly with the CEP with a periodicity of one peak spacing per π CEP-change, while the shape of the comb stays the same.

part is low compared to the intensity in part I (1.4% of the total flux), yet the expected energy tuning capability is still large due to the generalized kinetic-heterodyne mixing principle. Fig. 5.20c) and d) show the high harmonics as a function of the time delay, where the measurement conditions were the same for both figures, except that in d) a temporal chirp of -5.7 fs^2 was added by reducing the amount of glass (fused silica wedges) in the beam before the pulse shaper. While in Fig. 5.20c) an energy tuning is not noticeable, we record a sloping of the harmonics in d). The experimental finding matches the numerical simulations displayed in Fig. 5.20b), where the measured driver spectrum was used to calculate the change of the instantaneous frequency at the intensity maximum of the driver pulse as a function of the time delays. Besides, we observe in Fig. 5.20 that the high harmonics of different orders peak at different time delays. The time-delay shift is more pronounced when the temporal chirp is added. A reason could be related to the time-delay difference found when a second harmonic is added for HHG [170], but the further investigation of this effect is beyond the scope of this work.

5.5.4 Fractional-Harmonic Comb Optimization

Having introduced the effect of the individual control variables, we show in this section how they can be applied for optimization at the example of the fractional-harmonic combs.

5.5.4.1 Experimental Results

The first degree of freedom for an experimental optimization of these combs is the spectral-cut position. In the experiment we found pronounced results for a close to symmetric spectral-cut position of 770 nm. The split spectrum and the measured harmonics are presented as a function of the time delay in Fig. 5.21. The complete scan was con-

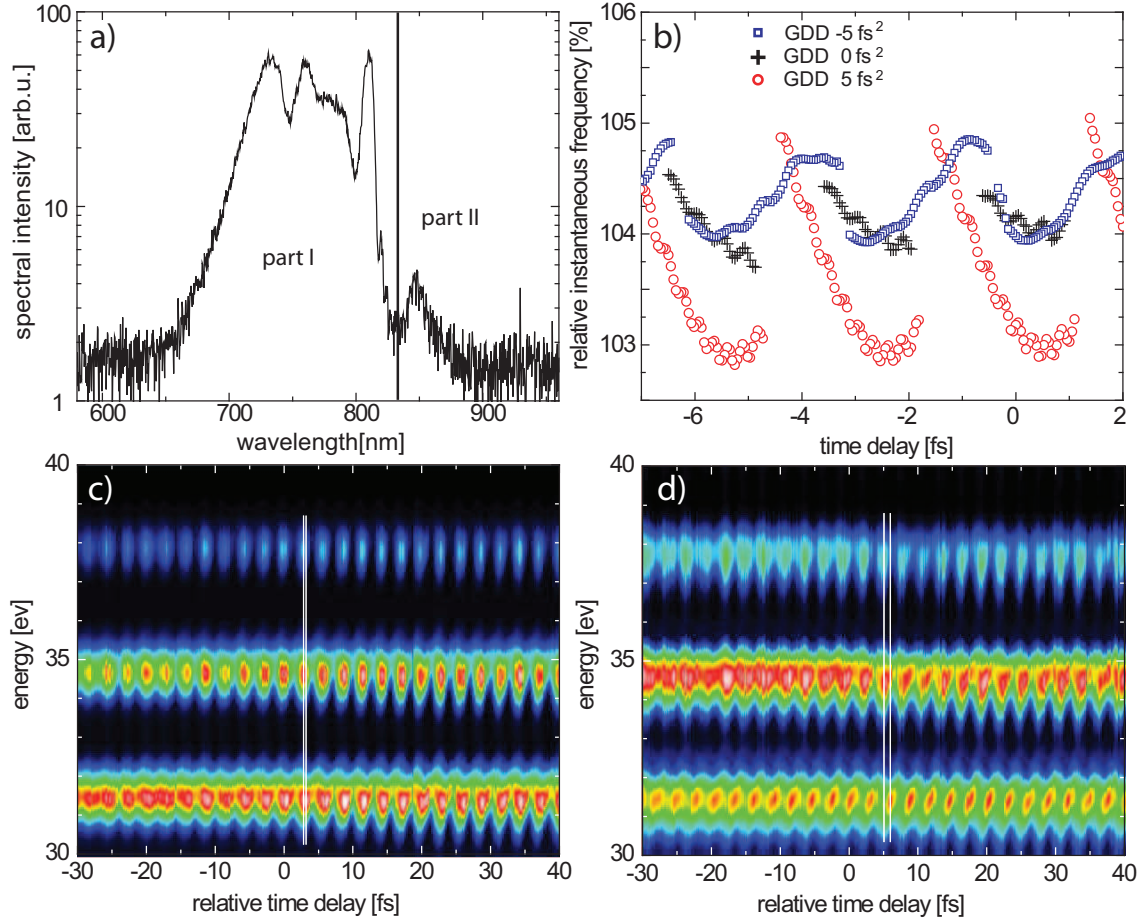


Figure 5.20: Influence of a temporal chirp on the split-spectrum controlled HHG. a) Measured heterodyne split spectrum with the spectral cut at 830 nm. b) Comparison to the energy-tuning model employing the measured spectrum and group delay dispersion (GDD) of $+5 \text{ fs}^2$ (circles), 0 fs^2 (pluses) or -5 fs^2 (squares). Relative instantaneous frequency at the driver pulse maximum as a function of the time delay. c) Measured high harmonics as a function of the time delay between the two spectral sections. d) Measured high harmonics with a negative temporal chirp of -5.7 fs^2 compared to (c) added to the fundamental laser field. Besides, we find here that the measured harmonics peak at different time delays (white lines). The difference is $0.18 \pm 0.10 \text{ fs}$ in c) and $0.77 \pm 0.08 \text{ fs}$ in d).

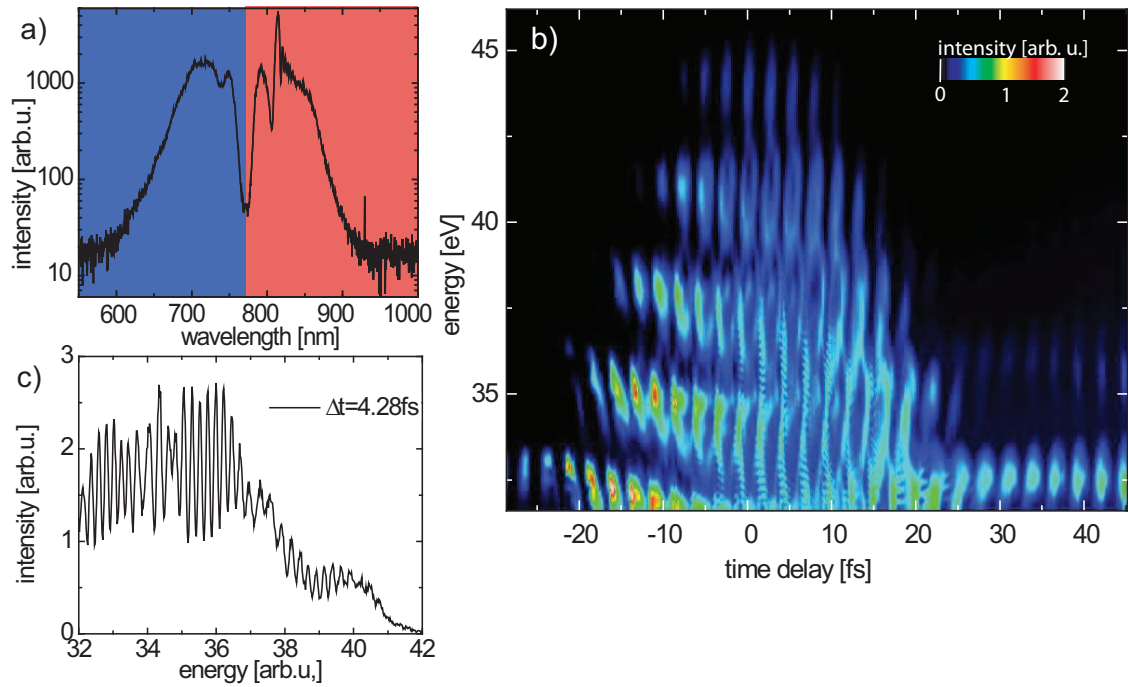


Figure 5.21: Optimization of fractional-harmonic comb generation (experimental results). a) Driver split spectrum with the cut at 770 nm and 52% of the energy in the first section. b) Measured harmonic spectrum as a function of the time delay with a stabilized CEP. Intense fractional-harmonic combs are produced for several time delays, spanning many harmonic orders. The fractional-harmonic combs show different energy-tuning slopes and spacings of the comb lines, controlled by the time delay. c) A fractional-harmonic comb over multiple harmonic orders is produced at a time delay of 4.28 fs. The strong time-delay dependence both on the attosecond- and optical-cycle scale allows to select fractional-harmonic combs or high harmonics with spectral properties that are suited with respect to different applications.

ducted with a fixed CEP of the driver laser. For $\Delta t < -8$ fs we see the intense odd harmonics, which beat with the time delay as discussed above. While at other cut positions or at scans without CEP stabilization (see Fig. 5.7) we measure fractional-harmonic combs which take turns in time delay with the odd harmonics we here observe completely different patterns for -5 fs $< \Delta t < 12$ fs. We see that the generation of intense odd harmonics is suppressed at energies from 30 to 40 eV. Instead intense fractional-harmonic combs are produced, which range depending on the time delay more or less continuously over an energy range of more than 8 eV. Surprisingly the 2ω -modulation in energy vanishes almost completely. Yet these combs do not have full intensity contrast between peaks and valleys of the individual comb lines (see e.g. the comb-spectrum for $\Delta t = 4.28$ fs in Fig. 5.21c). At the time delays between the combs a broad harmonic continuum is generated. Beyond the cut-off energy of the fractional harmonics, we see odd harmonics which show a sub-cycle structure. They are spectrally broadened to such an extent that they even overlap with the next odd harmonic orders. Their time-delay dependent intensity profile forms the letter "O". A possible explanation of these findings could be that for a large overlap of the subfields (-5 fs $< \Delta t < 10$ fs) in case of constructive interference of the subfields at time 0, the peak intensity is so high that after the production of about two attosecond pulses the

plasma density is high enough to close the temporal ionization gate on the leading edge of the driver pulse. But in case of a shaped driver pulse with two lower intensity maxima, the ionization rate is much lower so that the ionization gate is open now for both APTs, allowing them a higher spectral intensity compared to the single APT. Besides, we see a good agreement to the numerical simulation shown in Fig. 5.12. When we take the same time-delay resolution as accessible in the experiment into account, we see that the experiment confirms the numerical finding that intense and continuous fractional-harmonic combs can be produced over large energy ranges.

Moreover, we observe in the experiment differently signed energy tunings of the fractional harmonics with the time delay. Around $\Delta t = 20$ fs we finally see fractional harmonics with a larger energy spacing and in a periodic change with odd harmonics as observed in the scans discussed before. We now show exemplarily how different properties of the fractional-harmonic comb depend on the time delay, which allows to gain the best-matching comb with respect to desired properties as for example a high peak-to-valley modulation contrast, the coverage of a wide or specific energy range, a perfect regular spacing of the individual lines or a high total intensity. For each such property of the comb we can define quality functions which quantify the match to the desired property. Afterwards we can scan the time delay optionally for different spectral-cut positions, temporal chirps, or CEP values, to find the optimum of an individual property. Additionally, we can combine and weight different quality functions to optimize several comb properties. To analyze the combs in more detail we take for each time-delay position the Fourier transformation of the harmonic spectrum in the energy range 31.6 eV to 36.0 eV. To avoid numerical artifacts a smoothing function was used at the edges of the harmonic spectrum. We directly obtain the inverse energy spacing of the comb lines. The inverse width (standard deviation) of this signal gives us a measure of the regularity of the line spacings. As a further quality function, we define the average contrast of the intensity peaks and valleys:

$$\text{contrast}(\Delta t) = \text{average}\left(\frac{I_{max} - I_{min}}{I_{max} + I_{min}}\right) \quad (5.13)$$

A high comb contrast means that the intensity of both attosecond pulse trains is well-balanced in the considered energy range. In Fig. 5.22, the Fourier amplitude, the average comb contrast, the Fourier-frequency, the total comb intensity and the inverse width of the Fourier peak corresponding to the fractional-harmonic oscillation in the spectrum are plotted as a function of Δt . These values are only presented for time delays where the Fourier-amplitude is above the threshold of 0.4 arb. u., which means that only those time delays are selected, where fractional high harmonics are produced to a significant level. We see that the quality parameters vary strongly both on subcycle and many-cycles time-delay scales. The quality parameters peak at different time delays, enabling to optimize selectively different properties of the produced combs. The experimental results confirm that the time delay offers various options to produce differently shaped as well as highly-regular fractional-harmonic combs.

To further examine the regularity of the fractional-harmonic combs experimentally, we vary the CEP of the driver laser field in steps of 0.1π in a range of 10π (see Fig. 5.23). We now apply a Fourier filter, where we select the 10th array element of the finite numerical Fourier-transform frequency space, in order to keep only the signal which is periodic

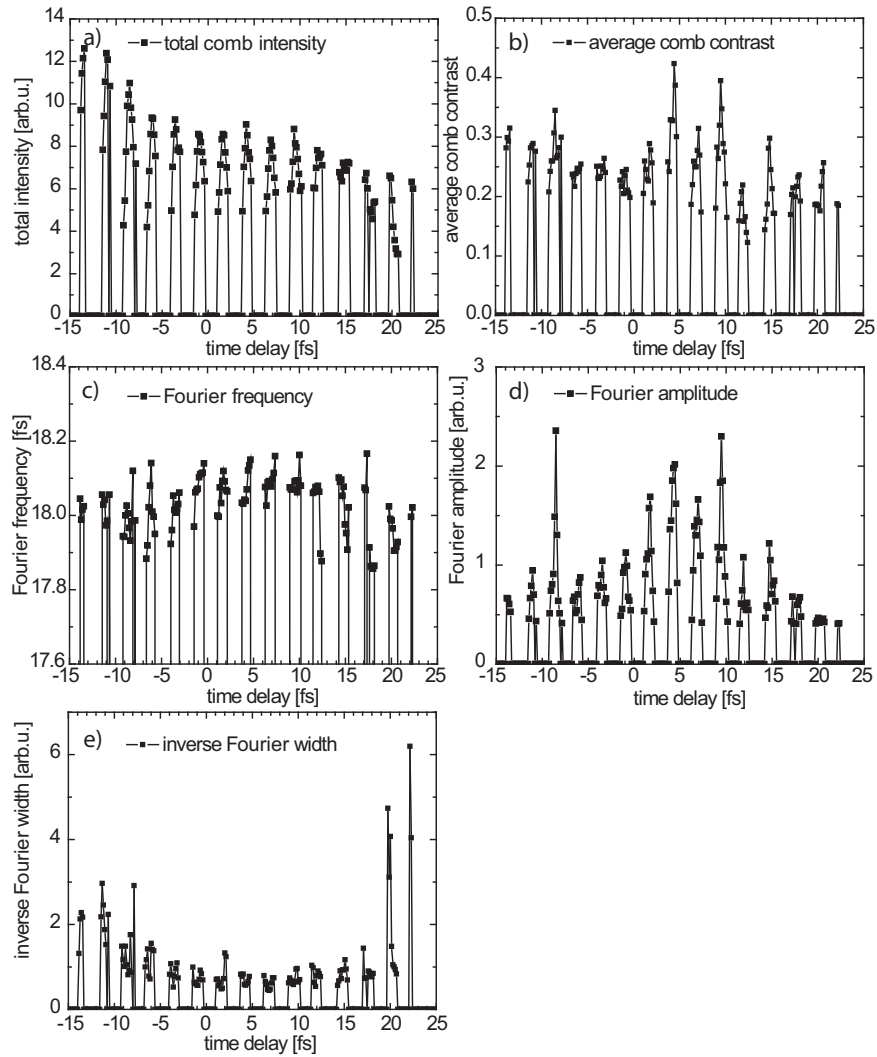


Figure 5.22: Analysis of several comb-quality values as a function of the time delay for the measured fractional-harmonic comb presented in Fig. 5.21 (experimental results). The spectrum was analyzed in the energy range from 31.6 to 36 eV. a) Total comb intensity. b) Average peak-to-valley contrast of the comb lines. c) Fourier frequency (inverse comb-line spacing). The value corresponds to the temporal distance of the attosecond pulse trains. d) Fourier amplitude in this Fourier-frequency range. e) Inverse width of this Fourier-peak. The quality values are only considered at time delays where the Fourier amplitude is above the threshold 0.4 arb. u.

with the CEP with the periodicity of π . We extract the phase of the Fourier-filtered signal and subtract the same linear phase with energy for every CEP. A linear phase in energy corresponds only to a shift in time, which can be neglected (see Eq. 2.12). The resulting spectral phase is almost flat in energy, except for energies, where the Fourier amplitude was not sufficiently high to retrieve the correct phase. The flatness of the spectral phase indicates a high regularity of the comb-line spacing. To study the regularity in a wider energy range, as can be done easily numerically, the camera has to be moved and the overlapping spectra have to be calibrated separately, which makes an online-analysis during the measurement for comb optimization challenging. A single measurement over an 8 eV exceeding energy range obtained a significant deviation from a linear spectral phase, while it remains unclear if the deviation could have been eliminated by the choice of other time delays or spectral-cut positions.

5.5.4.2 Simulation Results

We now compare the experimental results of the comb optimization to the analysis of numerically calculated high-harmonic spectra. For the simulations the measured spectrum displayed in Fig. 5.21 and the spectral cut at 770 nm were applied to correspond to the experimental situation. The spectral phase was considered to be flat (no chirp) except for the spectral phase induced by the time-delay operation. Making use of the advantage of the simulations that the high harmonics spectrum is given here for the complete energy range, we analyze a larger energy range compared to the experiment (32 eV to 56 eV). Fig. 5.24 shows the values for the same quality functions as in the experimental case (Fig. 5.22). Again, we see a large and separately controllability of the different comb quality characteristics as a function of the time delay. We gain excellent results for the average comb contrast (see Fig. 5.22b) and f), demonstrating that the fractional-harmonic combs or, in the view of the time domain the two attosecond pulse trains, can be well balanced in their entire spectral range (exceeding a bandwidth of 30 eV). The superimposed 2ω -modulation is clearly visible in the entire spectral range for the comb with the highest contrast. For applications where this superposition is not favorable it can be suppressed by a corresponding specific optimization as demonstrated experimentally in Fig. 5.19.

5.5.5 CEP Spectral Interferometry of the Fractional-Harmonic Combs

We now apply the method of carrier-envelope phase spectral interferometry (CEPSI) [133] as introduced in chapter 3 to analyze the temporal structure of the two attosecond pulse trains that produce the fractional-harmonic combs. We optimize the fractional-harmonic combs by the choice of the spectral-cut position and the time delay as free parameters to produce a continuous fractional-harmonic comb over several harmonic orders. We avoid the superposed 2ω -modulation, which was clearly visible in Fig. 5.7 and obtain the harmonic spectra in Fig. 5.25a) as a function of the CEP. The application of the method is enabled by the regular energy tuning of the fractional-harmonic combs with the CEP, which is similar to energy tuning of the odd harmonics in conventional

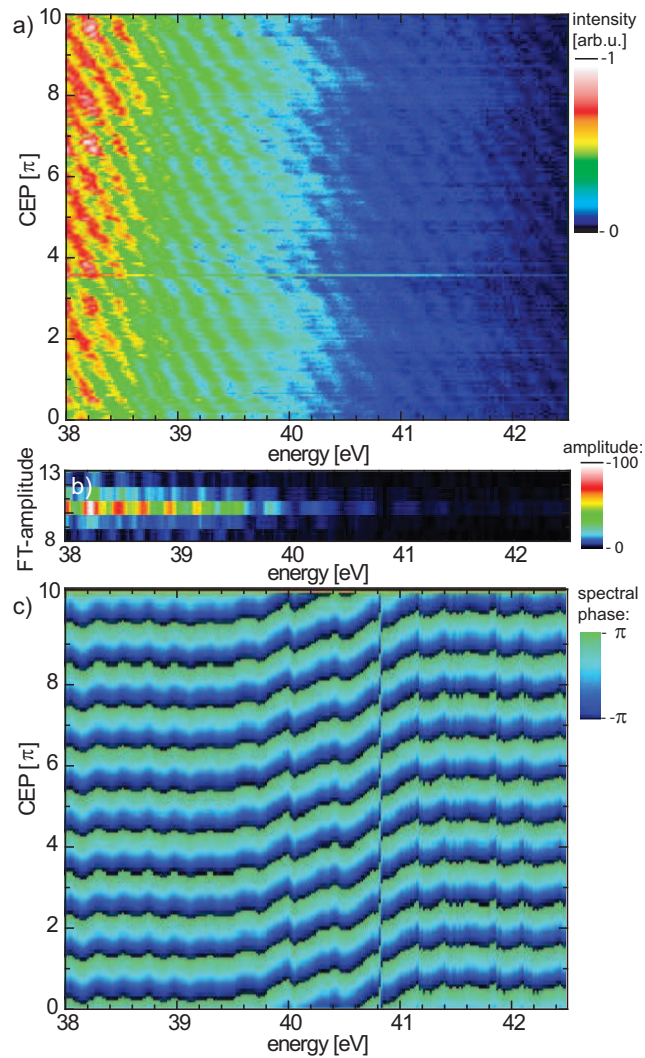


Figure 5.23: Analysis of comb regularity by CEP-resolved spectral interferometry [132] (experimental results). a) Spectrum of fractional high harmonics measured for stabilized CEPs scanned from 0 to 10π . b) The Fourier transformation along the CEP obtains a peak at pixel 10, which corresponds to a pronounced periodicity of the fractional harmonics with the CEP of 1π . c) After selection of this pixel 10 an inverse Fourier transformation for each energy is performed and the phase is displayed. After subtraction of a linear phase in energy, which is an arbitrary time delay, the spectral phase of the comb is close to flat in the presented measurement, except for energy regions, where the Fourier-amplitude was so small that artificial phase shifts might appear.

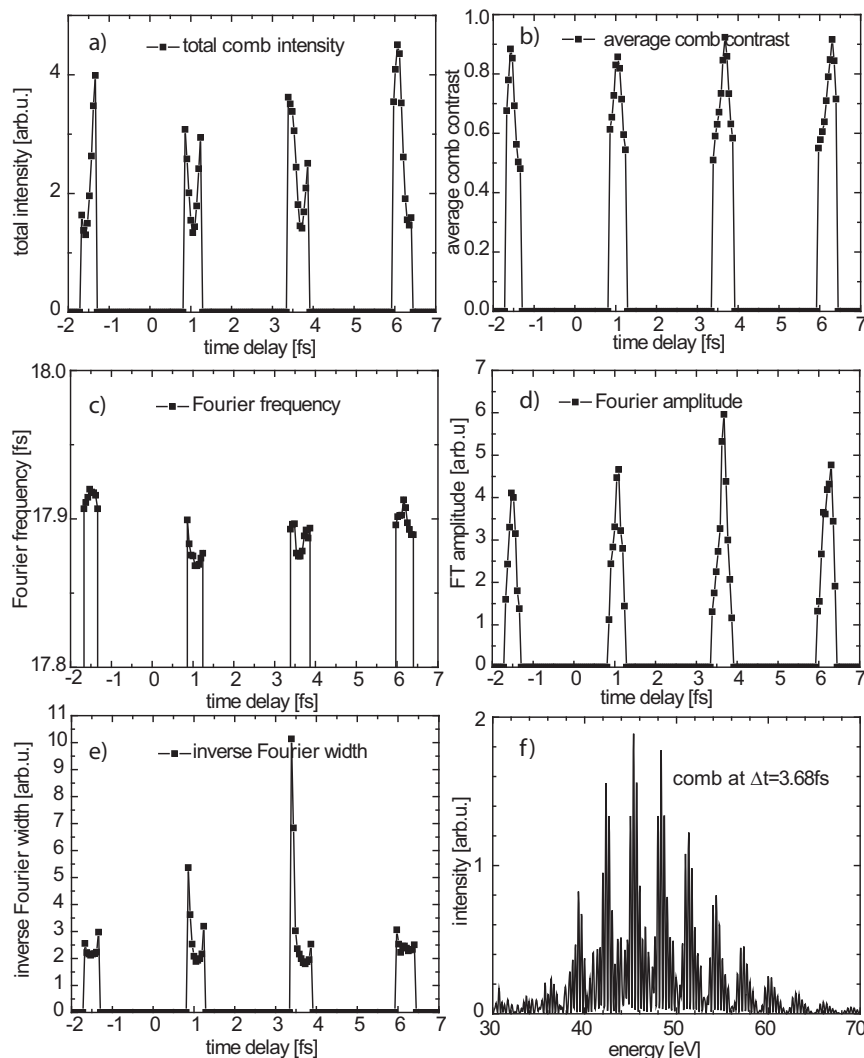


Figure 5.24: Optimization of the fractional-harmonic combs by tuning the time delay between the two spectral sections (simulation results). The simulations are based on the measured spectrum (Fig. 5.21) with the spectral cut at 770 nm. The following properties of the fractional-harmonic comb in the energy range from 32 eV to 56 eV were analyzed as a function of the time delay: a) The total comb intensity. b) The average contrast between peak and valleys in the comb, where 1 is the best possible value. c) The Fourier transformation of the spectrum obtains the comb lines frequency (=inverse spacing of the comb lines). d) The Fourier amplitude at this frequency. e) Its inverse width is a measure of the comb regularity. f) The spectrum of the fractional-harmonic comb at the time delay 3.68 fs was optimized with respect to a high comb contrast. A high contrast is realized for the complete spectral range of the comb.

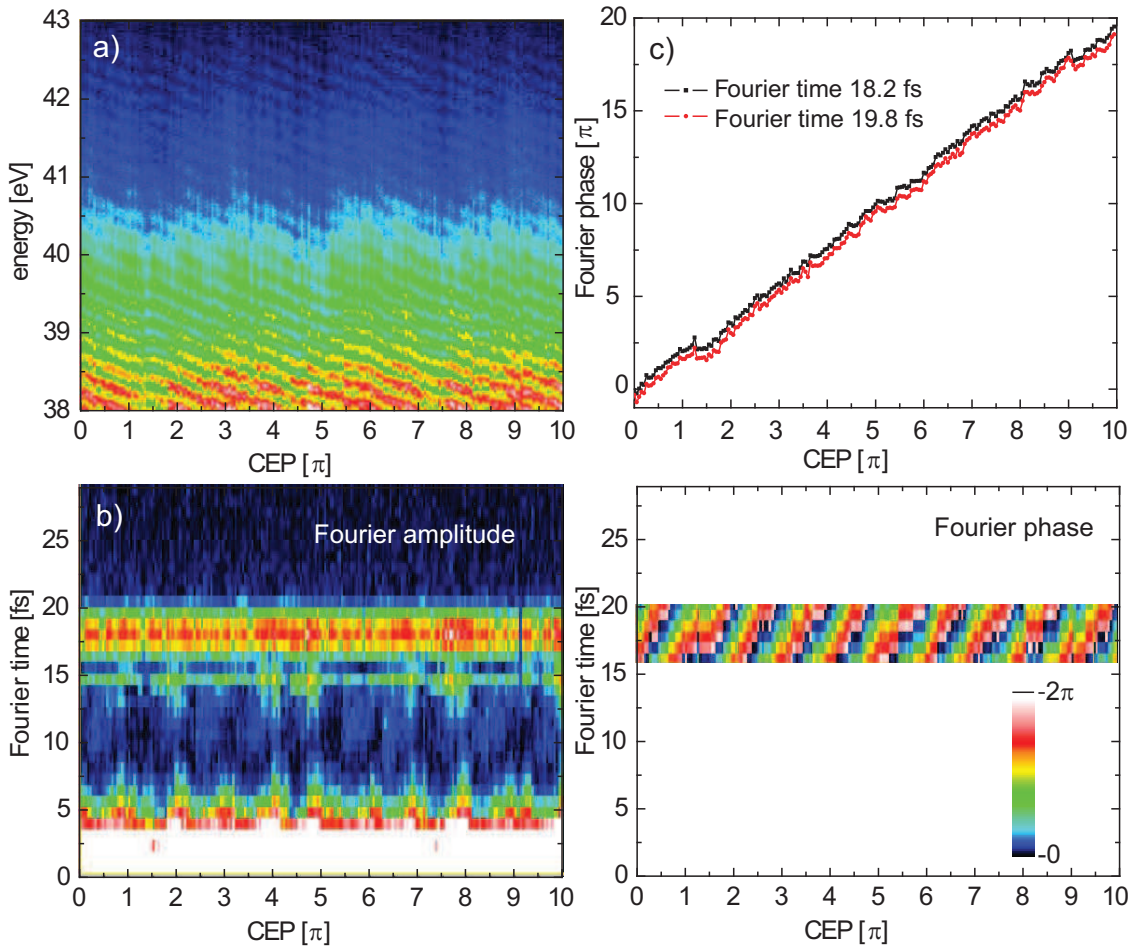


Figure 5.25: Carrier-envelope phase spectral interferometry (CEPSI) of fractional-harmonic combs (experimental results). a) Harmonic spectrum as a function of the CEP. b) Complex Fourier transformation of a) with respect to the energy reveals a spacing of the APTs of ~ 18 fs. c) The unwrapped Fourier phase is plotted for the Fourier times 18.2 fs and 19.8 fs in (b) and tunes linearly with the CEP. This demonstrates the capability to freely set the relative phase between the two produced attosecond pulse trains.

CEPSI. The lower energy spacing of the fractional harmonics enhances the number of interference structures and thus significantly the resolution in the spectral domain. While conventional CEPSI is based on the interference of few attosecond pulses this is now transferred to the interference analysis of the two attosecond pulse trains. Fig. 5.25b) shows the Fourier transformation of the fractional harmonics for each value of the CEP, which is scanned continuously from 0 to 10π . We see in the Fourier domain that the spacing of the attosecond pulse trains is about 18 fs and is not altered by the CEP. There are no visible periodic changes of the Fourier amplitude with the CEP. This indicates that the spectral shape of the fractional-harmonic combs is hardly influenced by the CEP and the envelope of the APTs stays about the same except for a modulation of the total intensity. In contrast, the phase of the Fourier signal tunes about twice as fast as the CEP. By the CEP an arbitrary value of this Fourier phase can be set. As a result we derive: while in chapter 4 we were able to set the spectral phase between two the members of an

attosecond twin pulse, we here gain experimental control of the spectral phase between two attosecond pulse trains, which is directly given by the Fourier phase. Additionally after the subtraction of a linear phase information about the comb regularity and the CEP stability during the measurement is contained in the standard deviation of the residual Fourier phase. One can take advantage of the fact that CEP SI reveals the phase between the attosecond pulse trains: When the fractional-harmonic combs are applied to transient absorption spectroscopy [189, 190, 191, 192] the complete information of the complex refractive index of the transmission medium can be revealed as a function of a dynamical parameter like the time delay to an excitation pulse. The transient transmission spectrum then tells for each time-delay step the spectral absorption (due to the imaginary part of the refractive index), while the change of the phase between the two APTs measures the changes of the dispersion (caused by the real part of the dynamical refractive index).

5.5.6 Subcycle Precision, Stability and Coherence

As we have seen the precision of the time delay between the two spectral sections is crucial to observe the manifold subcycle effects. To determine the precision of the time delay in our setup, we first look at the fastest changes in the harmonic spectrum we can resolve with the time delay. Fig. 5.26 shows an example of the CEP-stabilized measurement presented in Fig. 5.21 at the energy of 35.3 eV. From the rising time (20% to 80% of the change) of the harmonic signals we get an upper limit for the precision of ~ 140 as. The value includes the interferometric stability within the measurement time, which would e.g. be affected by the fluctuations of the refractive index of air in the part of the beam path where the two spectral sections are separated. Secondly, the interferometric stability was measured with a similar split-mirror setup based on a piezo stage from the same supplier and with the same specifications, obtaining a stability of 40 as. A high precision and stability of the time delay between the two subfields is a requirement of the split-spectrum control method for the observation of CEP effects. This is due to the effect that the change of the effective CEP of the shaped pulse is rapidly altered by a small change of the time delay (Eq. 5.10, Eq. 5.11). The amplification arises from a multiplied temporal shift of the intensity maximum by a relative small variation of the time delay. For such an amplification factor of five, which is a reasonable value, the stability between the spectral sections must be $T/25 \approx 100$ as to resolve a CEP change of $\frac{2\pi}{5} = 0.4\pi$. The clearly resolved observation of CEP effects in section 5.5.2 points to such an attosecond-precise stability between the two subfields in the experiment. If the stability of the subfields gets too low, the fractional-harmonic combs cannot be observed any more, since they are only produced for a time-delay range < 1 fs within one cycle.

The coherence of the split-spectrum pulse shaping is proven by the observed pronounced beating of the harmonic intensity which results from exactly that coherent pulse shaping. Additionally, the generation of the fractional high harmonics demonstrates firstly the coherence of the generated attosecond pulse trains even though they are spaced by many cycles, and secondly, again, implies coherent tailoring of the driver pulse.

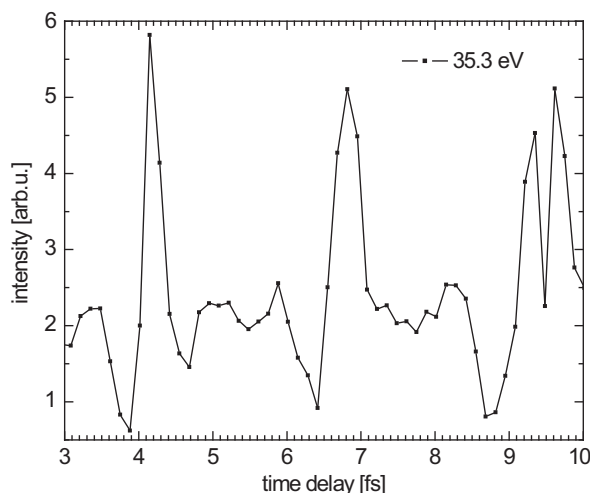


Figure 5.26: Interferometric stability of the pulse shaper (experimental result). The measured high-harmonic signal at 35.3 eV is displayed as a function of the time delay between the spectral sections. From the ability to resolve rapid periodic changes of the high-harmonic intensity, we derive a time-delay resolution and interferometric stability of ~ 140 as (time span for the relative-intensity change from 20% to 80%).

5.5.7 Influence and Independent Way of Action of the Individual Control Parameters

In this section the influence and effects of the individual control parameters on the produced high-order harmonics will be summarized. Results marked with a star (*) have only been demonstrated numerically, while for all other results experimental and numerical evidence is given.

- The time delay has the largest impact on HHG. We separate its effects into the sub-cycle time delay and the overall time delay with variations from cycle to cycle. With the one laser-cycle periodicity the harmonic intensity beats, the harmonic energy is tuned and where applicable fractional-harmonic combs are generated. In numerical simulations (*) we have further seen a large, rapid subcycle energy tuning of the odd harmonics, which is introduced by a rapid change of the effective CEP of the shaped driver pulse when the subcycle time delay is tuned. The overall time delay controls the number of attosecond pulses, the relative intensity of odd and fractional harmonics, the total harmonic intensity, the regularity of the fractional-harmonic combs and the harmonic-energy tuning introduced by a change of the instantaneous frequency.
- The CEP of the driver field finely tunes the fractional-harmonic combs in energy. This enables to set the spectral-phase difference between the two APTs. The CEP tunes odd harmonics as well, if the time-delay stabilization is sufficiently precise (*).
- The spectral-cut position defines the regime where the generation of fractional-harmonic combs, the energy tuning of the odd harmonics or the intensity beating

are enhanced separately. Moreover, it determines the sign and the extension of the instantaneous-frequency induced harmonic-energy tuning with the time delay.

- The influence of a small temporal chirp delivers an independent superposed addition to the shape of the harmonic-energy tuning.
- The intensity of the driver field controls the cut-off energy of both fractional high harmonics and regular high harmonics. It steers the intensity of the harmonics and by ionization gating the attosecond pulse number (*).

In total, the studied control parameters act qualitatively different in their mechanisms and effects on HHG. A number of different properties can extensively be controlled in each case by the use of only one or two control knobs. This reduces the expected time expenditure to reach a given optimization goal, since it is known which variable(s) has/have to be scanned to realize the optimization goal. On the other side each control parameter has only a limited number of significant effects. As demonstrated this opens ways to steer several properties of the produced attosecond pulse trains at once (see e.g. the comb optimization in section 5.5.4). Though the control parameters are not fully independent according to the strict definition given in chapter 4, their high level of independence makes them exemplarily suitable for a comprehensive, multi-parameter and manifold control of attosecond pulse trains and their spectral properties. With this knowledge of the above described fundamental control effects and mechanisms, the attosecond pulses and pulse trains can now be tailored in more complex manners.

5.6 Applications

In the following a few possible applications of the fractional-harmonic combs are presented. For a first application the spectral bandwidth of the laser could be narrowed with the consequence that longer driver pulses are produced with a much longer temporal separation of the two driver peaks and thus also of the two attosecond pulse trains. The fractional harmonics would then be much narrower and supply a finer spectral resolution. Moreover, the driver pulse could be derived off a high-repetition rate frequency comb laser source. The resulting 'supercomb' with the superimposed fractional-harmonic modulation could then be helpful by supplying additional coarse markers for identifying the absolute spectral position in the underlying fine and perfectly regular frequency comb created by the phase-locked driver pulse. Such combs could then be utilized for advanced, high-precision frequency metrology and interferometry experiments in the XUV region [193, 194].

Moreover, the observed spectral broadening of the harmonics reveals the controlled generation of two to three attosecond pulses. The implementation of additional gating techniques or the use of a broader fundamental spectrum would deliver isolated attosecond pulses for other applications and experiments. The controlled production of isolated or few attosecond pulses could then be applied to probe or steer attosecond electron dynamics in atoms, molecules or solids on their natural attosecond time scale. The findings of this chapter are further important for and give a comprehensive insight into field synthesis

in general. Even when more than two spectral driver sections are used, it is helpful to understand the impact and the versatile control mechanisms behind two subfields as well as the influence of the choice of the spectral-cut positions.

Furthermore, interference experiments with two fully coherent and adjustable attosecond pulse trains could be performed. Quantum dynamics originates from the interference of at least two different pathways leading to the same final state respectively. By excitation of an bound electron by two temporally spaced attosecond pulse trains (or even better pulses as in chapter 3) with controlled spectral-phase difference a wavepacket can be initiated, where its dynamics is directly governed by the relative phase of the two attosecond pulses (/trains). The final states as given by the quantum system (see the studies of electron dynamics in section 3.2) could then be selectively reached. The fully-tunable phase difference between the attosecond pulse trains also makes them perfectly suitable for spectral-interferometry experiments. In combination with the CEP-spectral interferometry method the phase difference between attosecond pulses or pulse trains and its variation after propagation through a medium could be used to uncover the transient spectral dispersion in transient absorption spectroscopy [189, 190, 191, 192] as described above. Together with the harmonic absorption spectrum the full information encoded in the complex refractive index can be determined as a function of the energy in the extreme-ultraviolet spectral range covered by the fractional-harmonic combs. The transient transmission (absorption and dispersion) could then be measured as a function of the time delay with respect to a more intense IR pulse which introduces electron dynamics in the transmitting medium on the attosecond to femtosecond time scale. The instantaneous frequency model finally could be applied to other HHG or strong-field electron-dynamics control configurations to understand or predict energy modulations there.

5.7 Conclusion

In this chapter comprehensive, coherent control of attosecond pulse-train production in argon was performed both experimentally and numerically by splitting up a broadband few-cycle laser field into two variable spectral sections and applying an attosecond-precise time delay between them. The two subfields beat in time on the scale of the driver pulse duration (~ 10 fs) leading to a one-laser-cycle periodic oscillation of the high-harmonic intensity when scanning the time delay between the spectral sections. For time delays with destructive interference of the two subfields of roughly comparable intensities, the driver field is shaped in a way that it contains two intensity maxima at which attosecond pulse trains with controllable relative intensity are generated. Their defined spacing in time leads to fine combs of fractional (noninteger) high harmonics in the extreme-ultraviolet spectral domain. A strong energy tunability of the odd high harmonics was observed and quantitatively explained by the change of the instantaneous frequency at the intensity maximum of the driver field with the time delay. We demonstrated that the generalized principle of kinetic-heterodyne mixing of laser subfields enlarges the parameter range for effective control of HHG both spectrally and temporally. Applying CEP stabilization we numerically found that a subcycle time delay introduces a large harmonic-energy tuning caused by a rapid effective-CEP change of the shaped pulse, which is enhanced by

the interference-based shift of the driver-peak position in time. The combination of time delay- and CEP control together with the choice of the spectral-cut position enables a multi-parameter, independent and versatile control of several temporal or spectral properties of the produced attosecond pulse trains. The fractional high-order harmonic combs can thus be optimized, for example to behave regularly in line-spacing within a large energy range or to create two attosecond-pulse-trains with a controlled relative phase and relative intensity. Furthermore, the CEP dependence of the fractional-harmonic combs allows the application of CEPSI [133] with an enhanced spectral resolution. This is especially useful for XUV-transient transmission spectroscopy, where at the same time the transient absorption and dispersion can be retrieved. The presented coherent control scheme acts purely microscopically, meaning that the presented effects are well understood by the modified response of a single atom to a tailored high-intensity few-cycle driver field. The CEP of the driver field, the time delay, the spectral-cut position and optionally a small temporal chirp are thus shown to be powerful control tools for HHG, which, given a sufficient spectral bandwidth, complement each other. In combination they are well-suited for a comprehensive, coherent control of electron dynamics in atoms, molecules, solids or soft matter on their natural attosecond or femtosecond time scale, especially when large spectral bandwidths are applied.

Chapter 6

Conclusion

Attosecond pulses of extreme ultraviolet or soft x-ray light enable the measurement of electron dynamics in atoms and molecules on their natural time scale. For example by employing an isolated attosecond pulse in combination with a near-single-cycle femtosecond pulse a delay in photoemission of 21 ± 5 as was measured between the electrons ejected from the 2p and 2s orbitals of neon atoms [195]. In this work we controlled the production of attosecond pulses and pulse trains by laser-optically steering the process of high-order harmonic generation (HHG). We used intense, few-cycle, broadband, close to bandwidth-limited, femtosecond laser pulses with a central wavelength around 750 nm for HHG in noble gases. The controlled variation of the carrier-envelope phase (CEP) of these pulses at the experiment delivered the first degree of freedom for HHG control. HHG has been controlled before by pulse-shaping using multi-cycle pulses and evolutionary algorithms, but there the generation of attosecond pulses was potentially also influenced by macroscopic effects like phase matching. In contrast, the control presented in this thesis is purely based on the manipulated response of single atoms to the modified driving laser field. We investigated the control of HHG by different methods. The key idea was to employ as few control variables as possible to gain the maximum control effect. This enabled to clearly uncover the individual control mechanisms. At first HHG was experimentally studied for the single-parameter case of CEP control in chapter 3. The newly-developed method of CEP-spectral interferometry was applied to reveal different behaviors of the relative phases between the three produced attosecond pulses as a function of the CEP. The method provides not only detailed information about the time structure of the attosecond pulses but traces both spectral amplitudes and phases, which makes it suitable for transient-transmission spectroscopy revealing the absorption and dispersion at once in combination with a (sub-)femtosecond time resolution.

In a theoretical investigation in chapter 4 a weak second laser field at the doubled frequency was added to extend the controllability by providing the time delay between the laser fields as a second control parameter besides the CEP. It was demonstrated that these two parameters alone are sufficient to independently and precisely set two properties of produced attosecond double pulses: their intensity ratio and their phase difference. Attosecond twin pulses with perfectly-balanced intensity and arbitrarily adjustable phase difference can be generated and applied for spectral interferometry experiments. This establishes the concept of independent and complete control of multiple temporal or spectral

properties of the attosecond pulses by an equally large set of control variables. Instead of applying two laser fields at separated frequencies a continuous broadband field can be divided into two variable spectral sections, which are then time delayed. Even if the energy distribution in both subfields is highly unbalanced a strong impact on HHG is retained. This is understandable by the principle of kinetic-heterodyne mixing of laser-fields, which we generalize.

The experimental implementation of the split-spectrum pulse-shaping approach revealed the controlled generation of attosecond pulse trains. The purely time-delay driven coherent interference of the two subfields already leads to a beating of the high-harmonic intensity and to a pronounced energy tuning of the high-order harmonics with the time delay. A quantitative model was developed to identify the origin of this energy tuning in a time-delay driven modulation of the instantaneous frequency at the intensity maximum of the shaped driver pulse. Considering a weak chirp of the driver field in the experiment an excellent agreement with the measured energy tuning was found. The beating of the two laser subfields in time shapes the driver pulse in a way that it exhibits two intensity maxima for certain time delays. As a consequence two temporally spaced attosecond pulse trains with adjustable relative intensity are produced. Their spectral interference leads to the generation of fractional high-harmonic combs (noninteger high-order harmonics). By means of CEP spectral interferometry it was demonstrated that the CEP shifts the comb in energy but retains the spectral shape. This means that the relative phase between the two attosecond pulse trains can be freely set by the CEP while the time delay controls their relative intensity. This gives experimental evidence for the multidimensional scheme of independent control, which we theoretically proposed beforehand, and verifies its potential for spectral-interferometry experiments and transient transmission measurements. The regularity of the fractional-harmonic combs can be investigated by a Fourier analysis of the spectral CEP dependence of the combs as a function of the time delay. Hereby variations within and between the beating cycles can be utilized for optimization. The time-delay driven shaping of the driver pulse causes a crucial change of its effective CEP already by the application of subcycle time delays of only a few tens of attoseconds. As a consequence numerical simulations revealed a rapid and continuous energy tuning of the high harmonics over several tens of eV which is effected by the rapid shaping-induced effective-CEP variation.

In total, comprehensive, multidimensional, coherent control of attosecond pulse and pulse train production was experimentally and theoretically demonstrated in both the spectral and temporal domain by an effective, few-parameter, open-loop control scheme with shaped, phase-stabilized, few-cycle laser pulses. The identified control mechanisms are fully understandable by the single-atom response. The gained knowledge of the interplay between CEP and time-delay control opens the door to produce tailored attosecond pulses and pulse trains for the coherent control of attosecond electron dynamics in atoms, molecules and nanostructures like nanotips. The provided insights are especially important for HHG with synthesized optical waveforms. Further applications are spectral interferometry experiments and enhanced transient-transmission measurements in the extreme ultraviolet and soft x-ray region.

Appendix A

Adaptive Control of High-order Harmonic Generation

A.1 Method

In chapter 2 we have seen that we can shape the real electric field $E(t)$ of our few-cycle driver laser pulse in the time domain by applying control over the spectral phase $\phi(\omega)$. The shaped driving laser pulse is then applied to HHG during which the laser pulse shape has large effects on the electron trajectories and consequently influences the temporal and spectral properties of the produced attosecond pulses. In the common 4f-pulse shaping setup the laser spectrum is spectrally resolved by a dispersive element for example a grating or prism [196, 98]. A focusing element images the separated frequencies in the Fourier plane, where the perfect separation and resolution of the spectral components is obtained by the choice of the focal length f for the distances between the dispersive and focusing elements as well as between focusing element and the Fourier plane. The beam is then reversed or guided through a symmetric setup to combine the frequencies again. In the Fourier plane a deformable mirror [197, 198] or a spatial-light modulator (SLM) [199, 200] can be placed to introduce a controlled spectral phase. This spectral phase results from variations in the optical path length, which can be introduced within SLMs for instance by a change of the refractive index. Within the pixels of a liquid-crystal display (LCD) the refractive index can be controlled by applying an individual voltage for each pixel. A disadvantage of especially deformable mirrors is that they might deflect the beam. The large number of degrees of freedom leads to a complex control process where the influence of single pixels is difficult to reveal. Instead quality functions are defined in regard to optimization goals by assigning a quality value (often called "fitness") to each recorded harmonic spectrum as a function of the set values (e.g. the voltages of each LCD pixel). The technique of evolutionary algorithms [201] has established an efficient procedure for the computer-based feedback control and optimization, which works as follows:

In the first step m combinations of set values are randomly generated, applied to control and the corresponding harmonic spectra are evaluated with a given quality function. The individual set parameters are referred to as the genes of an individual, while the sum of

the m individuals constitutes a generation. After the measurement and evaluation of the m spectra, each corresponding to one individual, the individuals of the next generation are generated out of the current generation's individuals in three ways [4]:

- cloning: The direct copying of the individuals with the highest quality mimics the "survival of the fittest" and transfers the until now best found solutions to the next generation.
- crossover: The exchange of parts of the genes collects several advantageous properties of both parents in the child individual.
- mutation: The production of new genes ensures that after some iterations all required genes are available to reach or approximate the global optimum.

The application of such algorithms leads to a remarkably fast increase of the average and best quality of the recorded spectra without prior knowledge of the studied process. For this reason the algorithms are called learning algorithms. The closed loop between pulse shaper, physical system, detector and learning algorithm gives this control type its name: closed-loop control, in contrast to the open-loop experiments without feedback mechanism. Adaptive control is another term for closed-loop control emphasizing more the ability to correct for optical distortions like the residual dispersion or wavefront irregularities. The evolutionary algorithms start with a first guess, which is then optimized. This illustrates the difficulties in finding the globally optimal set of control parameters which lead to a desired result, while on the other hand the response of a controlled system can be calculated more easily [202].

While closed-loop experiments [203] are common in femtochemistry [48, 204, 205, 206], where for instance chemical bonds can be selectively broken with the Tanner-Rice type control [207], there have been only a few applications to HHG in the last years. Deformable mirrors were employed to selectively enhance the intensity of individual high-harmonic orders and to enhance the intra-atom phase matching [208, 209, 210]. An LCD-based SLM was used to study the influence of higher dispersion orders on HHG [211]. Similarly deformable mirrors or SLMs can be employed to control the spatial profile of the driver pulse, for example to correct for wavefront distortions [212]. Additionally, the control of the spatial structure (e.g. concentration of the intensity in one single mode) has been shown to be essential for the optimization of high harmonics produced in hollow fibers [213, 214]. Moreover, a programmable acousto-optic dispersive filter was applied within a learning loop to tune the wavelength of a high-order harmonic and at the same time optimizing the total harmonic flux [215]. A common drawback of the cited closed-loop HHG experiments except those by Villoresi *et al.* and Wang *et al.* [211, 212] is that multiple-cycle laser pulses were applied with a typical length around 30 fs. As a consequence more trajectories contributed to HHG and in some cases also macroscopic effects such as phase matching played a major role due to the larger plasma build-up in longer driver pulses.

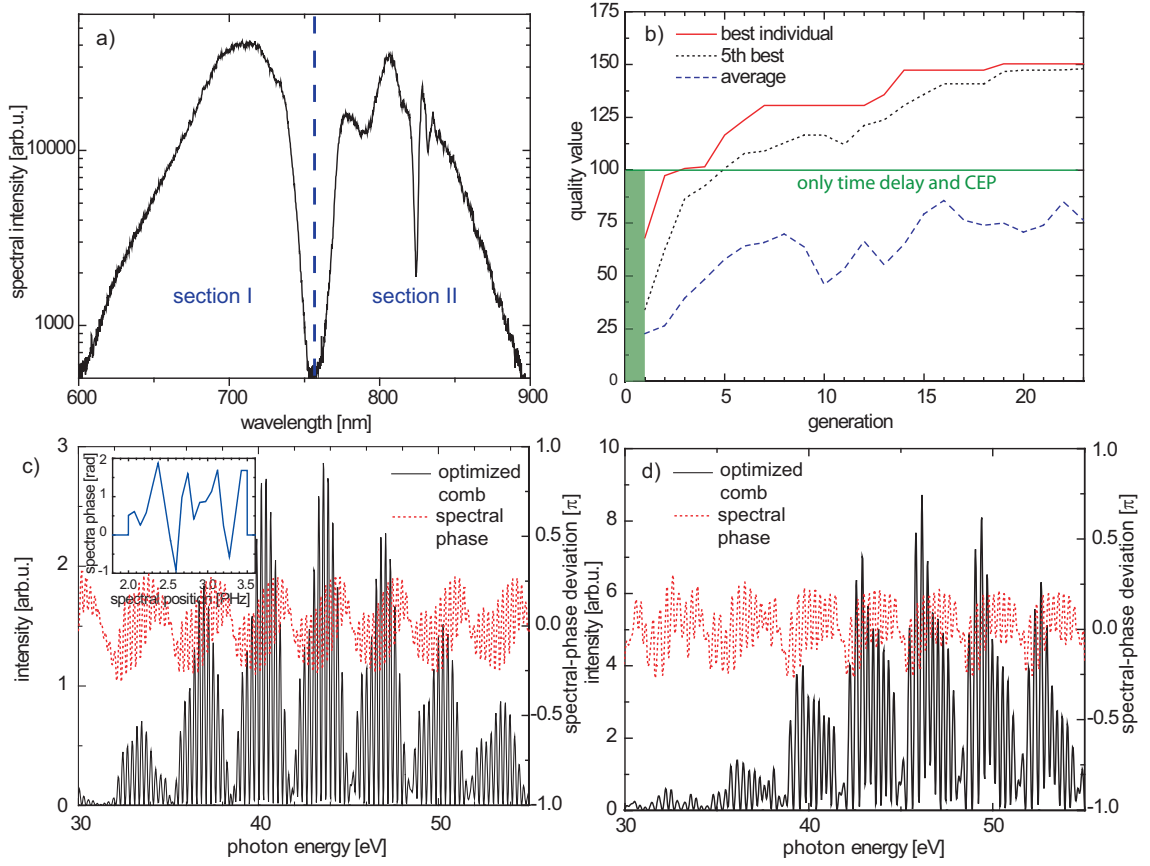


Figure A.1: Optimization of the fractional-harmonic comb contrast by an evolutionary algorithm (numerical results). For control the laser spectrum (a) is divided into 20 pixels with variable spectral phase. Further the CEP and the time delay between spectral section I and II are varied. b) Evolution of the quality of the fittest (solid line), the 5th best (dotted line) and the average (dashed line) of the 40 individuals of each generation. The shading at generation 0 marks the quality range accessible by the pure time-delay and CEP control with an unmodulated spectral phase. c) Spectrum of the comb with the highest fitness after 23 generations (solid line) and spectral phase of this comb after subtraction of the linear component (dashed line). Inset: optimized LCD spectral-phase addition. d) Spectrum of the comb produced with the unmodulated driver field at the optimal time delay of 1.32 fs (solid line) and spectral phase of the comb after removal of the linear spectral-phase component (dashed line).

A.2 Numerical Results

Fig. A.1 gives a numerical example of the optimization of fractional high-harmonic combs by an evolutionary algorithm. The mechanism of the generation of such combs and the applied numerical model is described in chapter 5. The pulse shaping is realized by the combination of time-delay control of two spectral sections and conventional adaptive spectral-phase manipulation. The split spectrum displayed in Fig. A.1a) is employed for the simulation with the non-flat spectral phase given in Fig. 5.2 to take the influence of a not-totally perfect dispersion compensation into account. The spectral cut is at 755 nm and we choose a variable time delay in the range 1.17 to 1.35 fs. In this time-delay range the driver pulse exhibits two intensity maxima to properly support the generation of fractional-harmonic combs. A step-wise defined spectral phase is controllably added to simulate pulse-shaping of a few-cycle laser pulse with a 20-pixel LCD pulse shaper. Furthermore the CEP (ϕ_0) is given as control variable. The quality of the generated high harmonics is determined by the quality function

$$f(\phi_1, \dots, \phi_{20}, \Delta t, \phi_0) = 2 \sum_{j=0}^N \frac{\max_j - \min_j}{\max_j + \min_j}, \quad (\text{A.1})$$

where ϕ_1, \dots, ϕ_{20} are the spectral phases at 20 equidistant spectral positions and simulate the LCD pixels. In between the spectral phase is interpolated. A generated fractional-harmonic comb with a high average peak-to-valley contrast and many detected harmonic peaks (large N) gives a high quality value $f(\phi_1, \dots, \phi_{20}, \Delta t, \phi_0)$. \max_j is the spectral peak intensity of the j th detected noninteger harmonic and \min_j represents the subsequent minimum intensity value. Consequently a comb with the full intensity contrast yields a quality value of 2 per detected fractional-harmonic peak, while zero spectral modulation results in a quality of 0. The population size is 40, the mutation probability is 20%, the cross-over probability 30% and the clone content is 10%. The high-harmonic spectra were analyzed in the energy range 31.2 eV to 52 eV. Fig. A.1b) presents the fitness (quality) evolution of the fittest, 5th-fittest (arbitrarily chosen) and the average individual for 23 generations, while Fig. A.1c) displays the optimized comb after 23 generations. The best spectral-phase addition which the evolutionary algorithm has found is given in the inset, while for comparison the purely time-delay- and CEP-optimized comb is shown in Fig. A.1d). As one can see the quality of the best comb has increased from 67.9 in the first generation to 150.3 in the last generation. The increase is steep within the first ~ 10 generations but then starts to flatten, which is typical for evolutionary algorithms. A very appropriate choice of the time-delay range and a not too large numbers of degrees of freedom (pixels) was advantageous to obtain high quality values already within the first five generations. The optimization by the time delay and CEP alone obtains a quality value of 100.4. This means that by the addition of further degrees of freedom the quality of the combs can be enhanced beyond the level which is reached by just two control variables. The improvement is significant ($\sim 40\%$) but small compared to the increase of degrees of freedom (1100%). Note that the spectral-cut position was not varied and that the time delay was restricted to 1.17 to 1.35 fs, while in Fig. 5.24 the best result was obtained for $\Delta t = 3.68$ fs. This points to the fact that the efficiency of additional degrees of freedom decreases rapidly and a large number of control variables is not essential for the control

and optimization of the fractional-harmonic combs. The harmonic cut-off energy and the integrated harmonic intensity are lower in the comb which was optimized by adaptive feedback control. The modulated spectral phase in this case resulted in a broader temporal distribution of the spectral components and thus lowered the peak intensity of the driver field.

To further investigate the effect of the additional pulse shaping by the evolutionary algorithm (see the optimized comb in Fig. A.1c) compared to pure time-delay and CEP control (see the best feasible comb in Fig. A.1d), we compare the regularity of the comb-line spacing of both displayed fractional-harmonic combs. For this purpose we calculate their spectral phase by the method of spectral interferometry. We remove the respective DC-components in the Fourier domain and select the frequencies corresponding to the integer- and fractional harmonic modulations. After Fourier transform back into the spectral domain the dominating linear phase is subtracted. The resulting spectral-phase deviation is plotted (dashed lines) for both combs in Fig. A.1c) and d). We see that the residual spectral phases are small ($-0.3\pi < \Delta\phi^{XUV}(\omega) < 0.3\pi$) for both fractional-harmonic combs with a standard deviation in the plotted energy range of 0.14π (adaptive-controlled comb) and 0.12π (two-parameter controlled comb). This points to a high comb regularity in both cases. In case of the adaptively optimized comb the phase patterns repeat more regularly with a period of two harmonic orders. In total, the adaptive-control simulation shows that the fractional-harmonic combs can be optimized with respect to comb contrast and comb regularity by evolutionary algorithms. The combination of split-spectrum time-delay control and adaptive spectral-phase manipulation might be especially advantageous if a substantial non-flat spectral phase after the dispersion compensation is remained.

Appendix B

Atomic Units

In the following a table for the conversion of atomic units to the International System of Units (SI) is given. The use of atomic units (a. u.) is favorable especially for calculations in atomic and molecular physics. The reason is that here atomic units reduce the complexity of equations and the numbers are then mostly given in the natural order of magnitude as defined by the hydrogen atom. Thus atomic units have been employed in this work.

Table B.1: Definition of selected atomic units. Data taken from Ref. [216], which was updated in 2010.

atomic unit of	SI value
energy	$(27.211\,385\,05 \pm 0.000\,000\,60) \text{ eV}$
time	$(24.188\,843\,265\,02 \pm 0.000\,000\,000\,12) \cdot 10^{-18} \text{ s}$
length	$(0.529\,177\,210\,92 \pm 0.000\,000\,000\,17) \text{ \AA}$
electric field strength	$(5.142\,206\,52 \pm 0.000\,000\,11) \cdot 10^9 \text{ V/cm}$
intensity	$(3.509\,445\,21 \pm 0.000\,000\,15) \cdot 10^{16} \text{ W/cm}^2$

Note that fundamental unit of charge equals 1 in atomic units, thus the electron charge is given by -1 .

List of Figures

2.1	a) Schematic high-order harmonic spectrum consisting of discrete lines at odd multiples of the fundamental laser energy. After the perturbative decrease of the harmonic intensity as a function of the harmonic order n proportional I^{-n} , a plateau is observed, where the harmonic intensity is about constant. Finally the harmonic intensity drops again and a cut-off is reached beyond which the harmonics vanish. b) Typical measured spectrum of high-order harmonics in our experiment using argon as the conversion medium.	9
2.2	Three-step model of high-harmonic generation. A strong electric field interacts with a single atom and bends the Coulomb potential. a) As the first step a valence electron tunnels out into the continuum, where it is accelerated by the electric field. b) In the second stage a half-cycle later the electric field changes its sign and accelerates the electron back to its parent ion. c) In the third step, the electron recombines into its initial state, producing an extreme ultraviolet (XUV) photon, which carries the kinetic energy gained in the electric field plus the ionization potential of the atom.	10
2.3	Different regimes of ionization in a laser field. a) Multi-photon ionization. b) Tunnel ionization. c) Over-barrier ionization.	11
2.4	Atomic conversion of intense infrared (IR) laser light into coherent attosecond pulses of extreme ultraviolet light by high-order harmonic generation.	12
2.5	a) Classically calculated electron trajectories in a cosine-like electric laser field. b) Kinetic energy of the electrons gained in the electric field as a function of the laser phase at recollision. Every energy is obtained by two trajectories spending different times in the field, which gives their denotation as short and long trajectory.	13
2.6	Phase matching of high-order harmonic generation. The attosecond pulses produced coherently by many atoms in the conversion medium need to interfere constructively for the build-up of a macroscopic HHG signal, which can be achieved when the driver field and the XUV light travel in phase with the same phase velocity.	18

2.7	Spectral broadening by self-phase modulation in the hollow fiber. Measured laser spectra recorded before (blue line) and after the hollow fiber without (black line) and with 1.38 bar neon (red line).	24
2.8	Customized chirped-mirror compressor placed after the hollow fiber. . .	27
2.9	Autocorrelation measurement for the determination of the pulse duration. The autocorrelation trace (b) implies a pulse duration of $t_{FWHM} = 6.4$ fs, which is close to the Fourier-transform limited pulse duration $t_{FT-limit} = 5.3$ fs calculated from the measured laser spectrum shown in (a).	30
2.10	Setup of the attosecond beamline (from [3]). In the first vacuum chamber the attosecond pulses are produced in an argon-filled cell. A special split-mirror setup and a target cell allow for interferometric experiments with time-delayed IR and XUV pulses. Finally, the high harmonics are recorded with a high-resolution flat-field XUV spectrometer (see Fig. 2.12).	32
2.11	Spectral removal of stray light and low-order harmonics by metal foils. Simulated transmission through $0.4 \mu\text{m}$ aluminum (a) and $0.4 \mu\text{m}$ zirconium (b) [106].	33
2.12	Setup of the customized high-resolution XUV spectrometer (from [3]). Pairs of metal filters (1) are applied to remove visible stray light and low-order harmonics. (2) Variable-line-space (VLS) grating, (3) flexible membrane bellow, (4) adjustment screws for coarse and fine positioning, (5) bearing for the high-precision selection of the spectral range and (6) backside-illuminated CCD chip of the cooled XUV camera.	34
3.1	Illustration of the carrier-envelope phase (CEP, ϕ_0). Electric field (solid line), instantaneous intensity (dashed line), and envelope (dots) of a Gaussian-shaped laser pulse with a 5 fs duration (FWHM) for $\phi_0 = 0$ (a) and $\phi_0 = -\pi/2$ (b). The CEP $\phi_0 = 0$ yields a cosine-like electric field with the carrier-peak at the envelope maximum, while $\phi_0 = -\pi/2$ gives a sine-like pulse with a carrier which is shifted in time by $\frac{\phi_0}{\omega_0}$	36
3.2	CEP-dependence of high-order harmonics and half-cycle cut-offs (experimental results). Spectra of high-order harmonics as a function of the CEP measured after (a) and before the focus (b). In both cases the energy of the harmonics is shifted by the CEP. This demonstrates the ability of the CEP to control electron dynamics on a time scale corresponding to a fraction of an optical cycle. In b) the high-harmonic spectra are composed of a coherent sum of CEP-dependent half-cycle emissions which peak at different energies depending on their individual cutoff energies. These so-called half-cycle cut-off (HCO) energies are clearly visible in the observed harmonic spectra. The CEP dependence of the HCO energies resolves the envelope of that part of the driving laser pulse where the attosecond pulses are emitted.	38

- 3.3 Simulation of phase-controlled spectral interference (from [133]).
 a) Spectrum generated by the interference of three pulses non-equidistantly spaced in time by $\tau_{23} = 1.1\tau_{12}$. The relative phase of the third pulse is varied $\Phi_3 = \varphi$ while the phases of the first two pulses are constant at $\Phi_1 = \Phi_2 = 0$. The arrows indicate the spectral positions where the alternating major and minor peaks swap their order. b) Spectra as in a) as a continuous function of the relative phase φ . c) Complex Fourier transformation of b) with respect to the energy. The three components of the spectral modulations can be indentified which correspond to the temporal distance of each two pulses. The Fourier phase indicates the phase changes between the pairs of pulses. 41
- 3.4 Carrier-envelope phase spectral interferometry (CEPSI): experimental results, from [133]. a) Measured high-order harmonics as a function of the CEP. b) Fourier transform of a), revealing the non-equidistant temporal spacing of three attosecond pulses. The phase between the first two attosecond pulses is not influenced by the CEP, while the relative phase between the third pulse and the others is fully modulated within 2π . c) The CEP modulates the phase between the two pairs of attosecond pulses which are displayed by the triangles (down, τ_{23}) and circles (τ_{13}) as given by the average over the marked temporal regions in b). In contrast, the phase between the pulses 1 and 2 (triangles, up, τ_{12}) is hardly influenced by the CEP. 42
- 4.1 Kinetic-heterodyne mixing of two continuous-wave (cw) laser fields (a-c) and generalized kinetic-heterodyne mixing of two laser subfields (d-f). Even the addition of a weak second harmonic with 1% intensity (a) strongly modulates the intensity of the driver laser field (b) and leads to a pronounced asymmetry of the electric field (c) for the time delay +0.86 fs (dashed lines) and -0.86 fs (solid lines). Similarly, a time delay between a 1%-relative intensity spectral section (II) of a broadband spectrum (d) and the main section (I) leads to a remarkable intensity modulation of the driver field as well (e). The field is now compressed to a few-cycle pulse. Pronounced changes of the electric field are displayed for the time delays +0.86 fs (dashed line), -0.86 fs (solid line) and 0 fs (dotted line). 50
- 4.2 Kinetic-heterodyne mixing of laser fields for attosecond twin-pulse generation (from [136]): a) Spectral phase (dotted line) and amplitude (not intensity!) of driving laser fields. b) Shaped electric fields of two different driving laser pulses (black and red dashed lines) and electric fields of generated attosecond pulses (black and red solid lines). c) Spectrum of the emitted attosecond pulses shown in (b). 51

- 4.3 Control of attosecond pulse generation with a two-color laser field consisting of a fundamental pulse and a weak second harmonic pulse (from [136]): a) Intensity ratio of the attosecond double pulses as a function of the CEP of the fundamental pulse and the time delay between the fundamental pulse and SH pulse. The green line indicates the parameters that result in a spectral-phase difference of π . b) Control of the spectral-phase difference between the attosecond pulses by the CEP and the time delay. The red line traces the maximal values of a), indicating the positions at which a perfect twin pulse is generated. c) Intensity ratio (green line) of attosecond pulses at a constant spectral-phase difference of π . d) Spectral-phase difference (red dots) at a constant intensity ratio of 1 and corresponding CEP (black squares). 53
- 4.4 Control of attosecond double-pulse generation by splitting up a broadband laser spectrum into two sections and applying combined CEP- and time-delay control (from [136]): a) Dependence of the intensity ratio of the two main attosecond pulses on the CEP and the time delay between the two parts of the laser spectrum (spectral cut located at 2.1 fs^{-1}). c) Control of the intensity ratio of the two main attosecond pulses as a function of the time delay and the spectral-cut position. b) and d) Spectral-phase difference between the attosecond pulses as a function of the time delay and the CEP (b) and as a function the time delay and the spectral-cut position (d). The red lines trace the maximum found in a) and c), demonstrating the control over the relative spectral phase while retaining an attosecond twin pulse at a constant intensity ratio of 1. 54
- 5.1 Setup of the split-spectrum pulse shaper (from [158]). A piezoelectrically driven split mirror is located in the Fourier plane of a Brewster-angled prism-based 4f-pulse shaper. The dispersion is compensated by a customized chirped-mirror compressor. The beam enters through the chirped-mirror compressor and is incident on the prism before a cylindrical mirror spectrally collimates and spatially focuses the beam onto the split-mirror surface. The beam is then redirected in reverse through the setup, leaving slightly above the original entrance spot to avoid the closest chirped mirror and is then sent to the HHG experiment. 62
- 5.2 Compensation of dispersion (simulation result, from [158]). Calculated change of the spectral phase due to the dispersion of 9.8 m air and 23.1 mm fused silica in the setup (red), due to the customized broadband chirped mirrors (black), the sum of both (green), and the sum magnified by a factor of 10 (blue). The spectral phase after the compensation is close to flat over a long wavelength range, allowing the shaping of few-cycle laser pulses. 63
- 5.3 Beating of the high-order harmonics (experimental results, from [158]). a) Driving split-spectrum fundamental pulse with the spectral cut at 795 nm. b) Spectra of the high harmonics as a function of the time delay between the two subfields labeled part I and II in a). 65

- 5.4 Beating of the driving laser field in time due to the interference of the two subfields (simulation results). A time delay Δt is introduced between the two symmetric halves of a Gaussian shaped laser spectrum centered around 780 nm. Intensity profiles of the shaped driving laser pulses for the following time delays: a) $\Delta t = 0$ fs. b) $\Delta t = 1.31$ fs. c) $\Delta t = 1.9$ fs. d) $\Delta t = 0.7$ fs. 66
- 5.5 HHG energy tuning and mechanism with an asymmetric energy-split spectrum (experimental results, from [158]). An asymmetric cut of the spectrum at 795 nm leads to a pronounced modulation of the instantaneous frequency at the peak of the driving laser field and thus to an attosecond-delay-dependent energy modulation of the high harmonics. a) Measured split spectrum of the driving laser field. b) Intensity of the shaped driving pulse dependent on time and time delay between the two spectral parts, and time-delay dependent modulation of the instantaneous laser frequency (yellow squares) at the intensity peaks (white lines) (simulation result). c) Measured energy modulation of the high harmonics compared to the relative modulation of the instantaneous laser frequency without chirp as in (b) (yellow squares) and for chirps of -10 fs² (red crosses) and $+10$ fs² (white pluses). Excellent quantitative agreement is found, confirming atom-level HHG control even with weak ($\sim 1.7\%$ of strong-pulse energy) control fields. 67
- 5.6 Simulated intensity profiles of split-spectrum shaped driver pulses (red lines) and instantaneous laser frequency (black lines) for the time delay -0.96 fs (a), -0.48 fs (b) and 0 fs (c). A decrease of the instantaneous frequency at the intensity maxima from 2.62 to 2.582 fs⁻¹ results in an energy tuning of up to 0.7 eV after n -fold magnification by the harmonic order n . For the calculation of the shaped pulses the residual spectral phase after dispersion compensation (see Fig. 5.2) was taken into account. 69
- 5.7 Generation of fractional-harmonic combs by split-spectrum control of high-harmonic generation (experimental results, from [158]). a) Measured spectrum of high harmonics dependent on the time delay between the two spectral ranges indicated in (b). b) Broadband split spectrum measured after the pulse shaper. c) Spectrum of conventional odd-integer harmonics at time delay 2.8 fs and fractional (non-integer) high harmonics at time delay 1.5 fs (intensity magnified by a factor of 3). 70
- 5.8 Mechanism of fractional-harmonic comb generation: Double attosecond pulse train generation (simulation results, from [158]): Shaped electric driving field intensity (dashed lines) and attosecond pulse trains (solid lines) for zero time delay (red lines, constructive interference of the two fundamental spectral parts at time 0) and for the time delay 1.28 fs (black lines, destructive interference at time 0). Two interfering attosecond pulse trains are generated in the latter case leading to deeply modulated fractional harmonics. 71

- 5.9 Generation of two equally intense attosecond pulse trains by coherent control of the peak intensity ratio of the driving subpulses (from [158]). a) Intensity ratio of the two most intense maxima of the shaped driving laser pulse dependent on the time delay. Simulation for the measured split-spectrum displayed in Fig. 5.7 including the residual spectral phase after the dispersion compensation given in Fig. 5.2. b) Shaped driving laser pulse with two equally intense subpulses at time delay 1.55 fs. 72
- 5.10 Generation of a deeply-modulated comb of fractional harmonics (simulation results, from [158]). a) Simulated harmonic spectra dependent on the time delay between the two spectral parts for the same settings as in Fig. 5.8. b) Spectrum of a fractional-harmonic comb with a high peak-to-valley contrast for the time delay of 1.28 fs in (a) (red line). 72
- 5.11 Rapid subcycle time-delay dependence of the high-order harmonics (simulation result). a) Simulation of the time-delay dependent high harmonics for the measured split spectrum displayed in Fig. 5.7 including the residual spectral phase after the dispersion compensation as shown in Fig. 5.2. In contrast to the previously-discussed experiment, the CEP of the driver pulses was fixed. b) Enlargement of a) revealing different patterns of harmonics. In section I the energies of the odd harmonics tune rapidly within few attoseconds of time delay over a large range of more than 10 eV for most of the harmonics. In section II even and odd harmonics appear, while in section III the substructures smear out. In section IV the fractional-harmonic combs are observed. 73
- 5.12 Simulated harmonic spectrum with a time-delay resolution of 250 as, corresponding to the assumed experimental interferometric stability between the two driver subfields. A Fourier filter was applied to the simulation in Fig. 5.11 to match the time-delay resolution. While the rapid subcycle energy tuning is smeared out, the fractional-harmonic combs are clearly visible. 74
- 5.13 Shaping-induced variation of the effective driver-pulse CEP (numerical results [188]). The time-delay controlled shaping of the driver pulse shifts the peak position of the pulse envelope (dashed line) in time (black arrows) compared to the original peak position (blue arrows) while the electric-field carrier (solid line) is locked. This strongly modulates the effective CEP, which is defined at the highest intensity maximum. While a time delay of 0 fs causes a cosine-like pulse (a), a time delay of 0.25 fs produces almost a minus sine-like pulse (b), the pulse at $\Delta t = 0.5$ fs comes close to a minus cosine-like pulse (c) and $\Delta t = 0.75$ fs obtains again a roughly cosine-like pulse (d). The temporal phase at the envelope peak gives an effective CEP $\phi_0^{shaped} = 0$ in (a), $\phi_0^{shaped} = 0.64\pi$ in (b), $\phi_0^{shaped} = 1.2\pi$ in (c) and $\phi_0^{shaped} = 1.84\pi$ in (d). 76

- 5.14 Influence of the CEP-stabilization (simulation results). a) Sum of ten harmonic spectra generated with $\phi_0 = 0, 0.1\pi, 0.2\pi, \dots, 0.9\pi$. Taking the sum of harmonic spectra produced with different CEPs smears out the rapid subcycle harmonic-energy tuning and results in the regular odd harmonics which vary only slowly with the time delay. b) Fractional-harmonics comb spectra at the time delay 1.62 fs. The sum of harmonic spectra with different CEPs as in a) (dotted line) is compared to a spectrum produced by a CEP-stabilized driver field $\phi_0 = \pi$ (solid line). The latter produces a much higher comb contrast. 77
- 5.15 Split-spectrum controlled HHG in the asymmetric-cut regime (experimental result). a) Driver spectrum with 12.3% of the total pulse energy in section II. b) High-harmonic spectrum as a function of the time delay between the spectral sections. A strong beating of the harmonic intensity is visible besides a spectral broadening and energy modulation of the high-harmonic lines. 78
- 5.16 Dependence of the beating of the two driving laser subfields on the spectral-cut position and effect of the generalized kinetic-heterodyne mixing (simulation results). Even if only a very small fraction of the laser spectrum is time delayed, it reshapes significantly the driver pulse. a) Spectral intensity of the driver field. b) Electric field for 0 fs (black line) and 1.25 fs (red line) time delay, where the driver spectrum is asymmetrically cut in a way that the second spectral part contains only 1% of the total intensity. c) Modulated pulse shapes at the time delay 1.25 fs for different fractions of the second-section intensity: 1% (dashed line), 5.3% (dotted line) and 11.7% (dash-dotted line) and comparison to 0 fs time delay (solid line). d) Pulse shapes for spectral fractions of 24.4% (solid line), 31.5% (dashed), 50.5% (dotted) and 82.4% (dash-dotted line). The pulse shape exhibits two intensity maxima at $\Delta t = 1.25$ fs if the smaller spectral section contains more than 11.7% of the total intensity. 79
- 5.17 Spectral-cut position dependence of the high-harmonic energy tuning (simulation results). a) Intensity of Gaussian shaped driver spectrum centered around 2.513 fs^{-1} ($\cong 750 \text{ nm}$) used for the simulations. b) Relative change of the instantaneous laser frequency at the peak of the driver pulse as a function of the time delay between the spectral sections for a spectral-cut position of 2.4 fs^{-1} (squares), 2.5 fs^{-1} (red circles), 2.6 fs^{-1} (pluses) and 2.7 fs^{-1} (diamonds). The highly unbalanced spectral cut at 2.7 fs^{-1} causes the most-pronounced frequency modulations. The values are plotted only for time delays for which the driver peak intensity is strong enough to produce high-order harmonics. 81

- 5.18 Split-spectrum controlled high harmonics as a function of the time delay for a phase-stabilized driver field (experimental results). a) Driver split-spectrum with the cut at 768 nm. b) Similar high harmonics and fractional-harmonic combs are revealed as in the CEP-averaged case. Low-intense odd high harmonics are produced and beat with the time delay for low pulse overlap as well (the color encodes the logarithm to the base 10 of the harmonic intensity). The latter finding results from the kinetic-heterodyne mixing effect for time-delayed laser fields. 83
- 5.19 Energy tunability of the measured fractional high-harmonic comb as a function of the CEP of the fundamental pulse (experimental result). The energy of the individual peaks shift linearly with the CEP with a periodicity of one peak spacing per π CEP-change, while the shape of the comb stays the same. 85
- 5.20 Influence of a temporal chirp on the split-spectrum controlled HHG. a) Measured heterodyne split spectrum with the spectral cut at 830 nm. b) Comparison to the energy-tuning model employing the measured spectrum and group delay dispersion (GDD) of $+5 \text{ fs}^2$ (circles), 0 fs^2 (pluses) or -5 fs^2 (squares). Relative instantaneous frequency at the driver pulse maximum as a function of the time delay. c) Measured high harmonics as a function of the time delay between the two spectral sections. d) Measured high harmonics with a negative temporal chirp of -5.7 fs^2 compared to (c) added to the fundamental laser field. Besides, we find here that the measured harmonics peak at different time delays (white lines). The difference is $0.18 \pm 0.10 \text{ fs}$ in c) and $0.77 \pm 0.08 \text{ fs}$ in d). 86
- 5.21 Optimization of fractional-harmonic comb generation (experimental results). a) Driver split spectrum with the cut at 770 nm and 52% of the energy in the first section. b) Measured harmonic spectrum as a function of the time delay with a stabilized CEP. Intense fractional-harmonic combs are produced for several time delays, spanning many harmonic orders. The fractional-harmonic combs show different energy-tuning slopes and spacings of the comb lines, controlled by the time delay. c) A fractional-harmonic comb over multiple harmonic orders is produced at a time delay of 4.28 fs. The strong time-delay dependence both on the attosecond- and optical-cycle scale allows to select fractional-harmonic combs or high harmonics with spectral properties that are suited with respect to different applications. 87

- 5.22 Analysis of several comb-quality values as a function of the time delay for the measured fractional-harmonic comb presented in Fig. 5.21 (experimental results). The spectrum was analyzed in the energy range from 31.6 to 36 eV. a) Total comb intensity. b) Average peak-to-valley contrast of the comb lines. c) Fourier frequency (inverse comb-line spacing). The value corresponds to the temporal distance of the attosecond pulse trains. d) Fourier amplitude in this Fourier-frequency range. e) Inverse width of this Fourier-peak. The quality values are only considered at time delays where the Fourier amplitude is above the threshold 0.4 arb. u. 89
- 5.23 Analysis of comb regularity by CEP-resolved spectral interferometry [132] (experimental results). a) Spectrum of fractional high harmonics measured for stabilized CEPs scanned from 0 to 10π . b) The Fourier transformation along the CEP obtains a peak at pixel 10, which corresponds to a pronounced periodicity of the fractional harmonics with the CEP of 1π . c) After selection of this pixel 10 an inverse Fourier transformation for each energy is performed and the phase is displayed. After subtraction of a linear phase in energy, which is an arbitrary time delay, the spectral phase of the comb is close to flat in the presented measurement, except for energy regions, where the Fourier-amplitude was so small that artificial phase shifts might appear. 91
- 5.24 Optimization of the fractional-harmonic combs by tuning the time delay between the two spectral sections (simulation results). The simulations are based on the measured spectrum (Fig. 5.21) with the spectral cut at 770 nm. The following properties of the fractional-harmonic comb in the energy range from 32 eV to 56 eV were analyzed as a function of the time delay: a) The total comb intensity. b) The average contrast between peak and valleys in the comb, where 1 is the best possible value. c) The Fourier transformation of the spectrum obtains the comb-lines frequency (=inverse spacing of the comb lines). d) The Fourier amplitude at this frequency. e) Its inverse width is a measure of the comb regularity. f) The spectrum of the fractional-harmonic comb at the time delay 3.68 fs was optimized with respect to a high comb contrast. A high contrast is realized for the complete spectral range of the comb. 92
- 5.25 Carrier-envelope phase spectral interferometry (CEPSI) of fractional-harmonic combs (experimental results). a) Harmonic spectrum as a function of the CEP. b) Complex Fourier transformation of a) with respect to the energy reveals a spacing of the APTs of ~ 18 fs. c) The unwrapped Fourier phase is plotted for the Fourier times 18.2 fs and 19.8 fs in (b) and tunes linearly with the CEP. This demonstrates the capability to freely set the relative phase between the two produced attosecond pulse trains. . . . 93

- 5.26 Interferometric stability of the pulse shaper (experimental result). The measured high-harmonic signal at 35.3 eV is displayed as a function of the time delay between the spectral sections. From the ability to resolve rapid periodic changes of the high-harmonic intensity, we derive a time-delay resolution and interferometric stability of ~ 140 as (time span for the relative-intensity change from 20% to 80%). 95
- A.1 Optimization of the fractional-harmonic comb contrast by an evolutionary algorithm (numerical results). For control the laser spectrum (a) is divided into 20 pixels with variable spectral phase. Further the CEP and the time delay between spectral section I and II are varied. b) Evolution of the quality of the fittest (solid line), the 5th best (dotted line) and the average (dashed line) of the 40 individuals of each generation. The shading at generation 0 marks the quality range accessible by the pure time-delay and CEP control with an unmodulated spectral phase. c) Spectrum of the comb with the highest fitness after 23 generations (solid line) and spectral phase of this comb after subtraction of the linear component (dashed line). Inset: optimized LCD spectral-phase addition. d) Spectrum of the comb produced with the unmodulated driver field at the optimal time delay of 1.32 fs (solid line) and spectral phase of the comb after removal of the linear spectral-phase component (dashed line). 103

Bibliography

- [1] A. Zewail.
Laser femtochemistry.
Science **242**, 1645–1653 (1988).
- [2] J.-C. Diels and W. Rudolph.
Ultrashort Laser Pulse Phenomena.
Second edition. Academic Press (2006).
- [3] C. Ott.
Attosecond multidimensional interferometry of single and two correlated electrons in atoms.
PhD Thesis, Universität Heidelberg (2012).
- [4] T. Pfeifer.
Adaptive control of coherent soft-x-rays.
PhD Thesis, Universität Würzburg (2004).
- [5] T. H. Maiman.
Stimulated Optical Radiation in Ruby.
Nature **187**, 493–494 (1960).
- [6] A. Schawlow and C. Townes.
Infrared and optical masers.
Phys. Rev. **112**, 1940–1949 (1958).
- [7] A. E. Siegman.
Lasers.
University Science Books, Sausalito (1986).
- [8] F. McClung and R. Hellwarth.
Giant optical pulsations from ruby.
J. Appl. Phys. **33**, 828–829 (1962).
- [9] P. Moulton.
Spectroscopic and laser characteristics of Ti-Al₂O₃.
J. Opt. Soc. Am. B **3**, 125–133 (1986).
- [10] D. Spence, P. Kean, and W. Sibbett.
60-fsec pulse generation from a self-mode-locked Ti-sapphire laser.
Opt. Lett. **16**, 42–44 (1991).
- [11] U. Morgner, F. Kartner, S. Cho, Y. Chen, H. Haus, J. Fujimoto, E. Ippen, V. Scheuer, G. Angelow, and T. Tschudi.
Sub-two-cycle pulses from a Kerr-lens mode-locked Ti : sapphire laser.
Opt. Lett. **24**, 411–413 (1999).
- [12] P. B. Corkum, N. H. Burnett, and M. Y. Ivanov.
Subfemtosecond pulses.
Opt. Lett. **19**, 1870–1872 (1994).
- [13] M. Drescher, M. Hentschel, R. Kienberger, G. Tempea, C. Spielmann, G. Reider, P. Corkum, and F. Krausz.

- X-ray pulses approaching the attosecond frontier.*
Science **291**, 1923–1927 (2001).
- [14] P. Corkum and Zenghu Chang.
The attosecond revolution [attosecond laser].
Opt. Photonics News **19**, 25–29 (2008).
- [15] G. Mourou and T. Tajima.
More Intense, Shorter Pulses.
Science **331**, 41–42 (2011).
- [16] J. Hecht.
A proliferation of petawatt lasers.
Laser Focus World **42**, 105 (2006).
- [17] R. W. Boyd.
Nonlinear Optics.
Second edition. Academic Press, San Diego (2003).
- [18] T. Brabec and F. Krausz.
Intense few-cycle laser fields: Frontiers of nonlinear optics.
Rev. Mod. Phys. **72**, 545–591 (2000).
- [19] C. Winterfeldt.
Generation and control of high-harmonic radiation.
PhD Thesis, Universität Würzburg (2006).
- [20] M. Ferray, A. L’Huillier, X. Li, L. Lompre, G. Mainfray, and C. Manus.
Multiple-harmonic conversion of 1064-nm radiation in rare-gases.
J. Phys. B **21**, L31–L35 (1988).
- [21] A. L’Huillier and P. Balcou.
High-order harmonic-generation in rare-gases with a 1-ps 1053-nm laser.
Phys. Rev. Lett. **70**, 774–777 (1993).
- [22] P. B. Corkum.
Plasma Perspective On Strong-field Multiphoton Ionization.
Phys. Rev. Lett. **71**, 1994–1997 (1993).
- [23] K. C. Kulander, K. J. Schafer, and J. L. Krause.
Dynamics of Short-pulse Excitation, Ionization and Harmonic Conversion.
Plenum Press, New York (1993).
- [24] A. Scrinzi, M. Ivanov, R. Kienberger, and D. Villeneuve.
Attosecond physics.
J. Phys. B **39**, R1–R37 (2006).
- [25] P. B. Corkum and F. Krausz.
Attosecond science.
Nature Phys. **3**, 381–387 (2007).
- [26] F. Krausz and M. Ivanov.
Attosecond physics.
Rev. Mod. Phys. **81**, 163–234 (2009).
- [27] P. Agostini and L. F. DiMauro.
The physics of attosecond light pulses.
Rep. Prog. Phys. **67**, 813–855 (2004).
- [28] T. Pfeifer, C. Spielmann, and G. Gerber.
Femtosecond x-ray science.
Rep. Prog. Phys. **69**, 443–505 (2006).
- [29] P. H. Bucksbaum.
The future of attosecond spectroscopy.
Science **318**, 393 (2007).

- [30] M. Ammosov, N. Delone, and V. Krainov.
Tunnel ionization of complex atoms and atomic ions in a varying electromagnetic-field.
Sov. Phys. JETP **64**, 1191–1194 (1986).
- [31] V. S. Popov.
Tunnel and multiphoton ionization of atoms and ions in a strong laser field (Keldysh theory).
Physics-Uspekhi **47**, 855 (2004).
- [32] K. Kulander.
Time-dependent theory of multiphoton ionization of xenon.
Phys. Rev. A **38**, 778–787 (1988).
- [33] Y. Mairesse, A. de Bohan, L. J. Frasinski, H. Merdji, L. C. Dinu, P. Monchicourt, P. Breger, M. Kovacev, R. Taieb, B. Carré, H. G. Muller, P. Agostini, and P. Salieres.
Attosecond synchronization of high-harmonic soft x-rays.
Science **302**, 1540–1543 (November 2003).
- [34] S. Kazamias and P. Balcou.
Intrinsic chirp of attosecond pulses: Single-atom model versus experiment.
Phys. Rev. A **69**, 063416 (2004).
- [35] M. C. Kohler, C. H. Keitel, and K. Z. Hatsagortsyan.
Attochirp-free high-order harmonic generation.
Opt. Express **19**, 4411–4420 (2011).
- [36] H. Kapteyn, O. Cohen, I. Christov, and M. Murnane.
Harnessing attosecond science in the quest for coherent X-rays.
Science **317**, 775–778 (2007).
- [37] T. Popmintchev, M.-C. Chen, O. Cohen, M. E. Grisham, J. J. Rocca, M. M. Murnane, and H. C. Kapteyn.
Extended phase matching of high harmonics driven by mid-infrared light.
Opt. Lett. **33**, 2128–2130 (2008).
- [38] T. Popmintchev, M.-C. Chen, P. Arpin, M. M. Murnane, and H. C. Kapteyn.
The attosecond nonlinear optics of bright coherent X-ray generation.
Nature Photonics **4**, 822–832 (2010).
- [39] M. Lewenstein, P. Balcou, M. Ivanov, A. L’Huillier, and P. Corkum.
Theory of high-harmonic generation by low-frequency laser fields.
Phys. Rev. A **49**, 2117–2132 (1994).
- [40] P. Salieres, B. Carré, L. Le Deroff, F. Grasbon, G. Paulus, H. Walther, R. Kopold, W. Becker, D. Milošević, A. Sanpera, and E. Lewenstein, Meltchakov.
Feynman’s path-integral approach for intense-laser-atom interactions.
Science **292**, 902–905 (2001).
- [41] M. C. Kohler, C. Ott, P. Raith, R. Heck, I. Schlegel, C. H. Keitel, and T. Pfeifer.
High Harmonic Generation Via Continuum Wave-Packet Interference.
Phys. Rev. Lett. **105**, 203902 (2010).
- [42] M. Kohler.
Frontiers of High-Harmonic Generation.
PhD Thesis, Universität Heidelberg (2011).
- [43] P. Antoine, A. L’Huillier, and M. Lewenstein.
Attosecond pulse trains using high-order harmonics.
Phys. Rev. Lett. **77**, 1234–1237 (1996).
- [44] P. Paul, E. Toma, P. Breger, G. Mullot, F. Auge, P. Balcou, H. Muller, and P. Agostini.
Observation of a train of attosecond pulses from high harmonic generation.
Science **292**, 1689–1692 (2001).

- [45] K. Midorikawa.
Ultrafast dynamic imaging.
Nature Photonics **5**, 640–641 (2011).
- [46] J. Itatani, J. Levesque, D. Zeidler, H. Niikura, H. Pepin, J. Kieffer, P. Corkum, and D. Villeneuve.
Tomographic imaging of molecular orbitals.
Nature **432**, 867–871 (2004).
- [47] A. D. Shiner, B. E. Schmidt, C. Trallero-Herrero, H. J. Woerner, S. Patchkovskii, P. B. Corkum, J.-C. Kieffer, F. Legare, and D. M. Villeneuve.
Probing collective multi-electron dynamics in xenon with high-harmonic spectroscopy.
Nature Phys. **7**, 464–467 (2011).
- [48] T. Brixner and G. Gerber.
Quantum control of gas-phase and liquid-phase femtochemistry.
ChemPhysChem. **4**, 418–438 (2003).
- [49] R. Carley, E. Heesel, and H. Fielding.
Femtosecond lasers in gas phase chemistry.
Chem. Soc. Rev. **34**, 949–969 (2005).
- [50] C. Brif, R. Chakrabarti, and H. Rabitz.
Control of quantum phenomena: past, present and future.
New J. Phys. **12**, 075008 (2010).
- [51] H. Rabitz, R. de Vivie-Riedle, M. Motzkus, and K. Kompa.
Chemistry - Whither the future of controlling quantum phenomena?
Science **288**, 824–828 (2000).
- [52] W. Warren, H. Rabitz, and M. Dahleh.
Coherent control of quantum dynamics - the dream is alive.
Science **259**, 1581–1589 (1993).
- [53] M. Hentschel, R. Kienberger, C. Spielmann, G. A. Reider, N. Milošević, T. Brabec, P. Corkum, U. Heinzmann, M. Drescher, and F. Krausz.
Attosecond metrology.
Nature **414**, 509–513 (2001).
- [54] K. Schafer, M. Gaarde, A. Heinrich, J. Biegert, and U. Keller.
Strong field quantum path control using attosecond pulse trains.
Phys. Rev. Lett. **92**, 023003 (2004).
- [55] M. Lewenstein, P. Salières, and A. L’Huillier.
Phase of the atomic polarization in high-order harmonic-generation.
Phys. Rev. A **52**, 4747–4754 (1995).
- [56] P. Salières, A. L’Huillier, and M. Lewenstein.
Coherence Control of High-Order Harmonics.
Phys. Rev. Lett. **74**, 3776–3779 (1995).
- [57] W. Boutu, S. Haessler, H. Merdji, P. Breger, G. Waters, M. Stankiewicz, L. J. Frasinski, R. Taieb, J. Caillat, A. Maquet, P. Monchicourt, B. Carre, and P. Salières.
Coherent control of attosecond emission from aligned molecules.
Nature Phys. **4**, 545–549 (2008).
- [58] R. López-Martens, K. Varju, P. Johnsson, J. Mauritsson, Y. Mairesse, P. Salierès, M. Gaarde, K. Schafer, A. Persson, S. Svanberg, C. Wahlström, and A. L’Huillier.
Amplitude and phase control of attosecond light pulses.
Phys. Rev. Lett. **94**, 033001 (2005).
- [59] C. Bourassin-Bouchet, Z. Diveki, S. de Rossi, E. English, E. Meltchakov, O. Gobert, D. Guenot, B. Carre, F. Delmotte, P. Salières, and T. Ruchon.
Control of the attosecond synchronization of XUV radiation with phase-optimized mirrors.
Opt. Express **19**, 3809–3817 (2011).

- [60] M. Hofstetter.
Multilayer Mirrors for Attosecond Pulse Shaping between 30 and 200 eV.
PhD Thesis, Ludwig Maximilians Universität München (2011).
- [61] M. B. Gaarde, J. L. Tate, and K. J. Schafer.
Macroscopic aspects of attosecond pulse generation.
J. Phys. B **41**, 132001 (2008).
- [62] T. Kanai, E. J. Takahashi, Y. Nabekawa, and K. Midorikawa.
Destructive interference during high harmonic generation in mixed gases.
Phys. Rev. Lett. **98**, 153904 (2007).
- [63] F. Lindner, G. Paulus, H. Walther, A. Baltuška, E. Goulielmakis, M. Lezius, and F. Krausz.
Gouy phase shift for few-cycle laser pulses.
Phys. Rev. Lett. **92**, 113001 (2004).
- [64] A. Rundquist, C. Durfee, Z. Chang, C. Herne, S. Backus, M. Murnane, and H. Kapteyn.
Phase-matched generation of coherent soft X-rays.
Science **280**, 1412–1415 (1998).
- [65] T. Popmintchev, M.-C. Chen, D. Popmintchev, P. Arpin, S. Brown, S. Alisauskas, G. Andriukaitis, T. Balciunas, O. D. Muecke, A. Pugzlys, A. Baltuška, B. Shim, S. E. Schrauth, A. Gaeta, C. Hernandez-Garcia, L. Plaja, A. Becker, A. Jaron-Becker, M. M. Murnane, and H. C. Kapteyn.
Bright Coherent Ultrahigh Harmonics in the keV X-ray Regime from Mid-Infrared Femtosecond Lasers.
Science **336**, 1287–1291 (2012).
- [66] J. Seres, E. Seres, A. Verhoef, G. Tempea, C. Strellil, P. Wobrauschek, V. Yakovlev, A. Scrinzi, C. Spielmann, and F. Krausz.
Source of coherent kiloelectronvolt X-rays.
Nature **433**, 596 (2005).
- [67] M. Schönwald.
Phase-matched few-cycle high-harmonic generation: ionisation gating and half-cycle cutoffs.
Diploma Thesis, Universität Heidelberg (2010).
- [68] M. Nisoli and G. Sansone.
New frontiers in attosecond science.
Prog. Quant. Electron. **33**, 17–59 (2009).
- [69] I. Christov, M. Murnane, and H. Kapteyn.
High-harmonic generation of attosecond pulses in the “single-cycle” regime.
Phys. Rev. Lett. **78**, 1251–1254 (1997).
- [70] F. Calegari, M. Lucchini, M. Negro, C. Vozzi, L. Poletto, O. Svelto, S. De Silvestri, G. Sansone, S. Stagira, and M. Nisoli.
Temporal gating methods for the generation of isolated attosecond pulses.
J. Phys. B **45**, 074002 (2012).
- [71] G. Sansone, L. Poletto, and M. Nisoli.
High-energy attosecond light sources.
Nature Photonics **5**, 656–664 (2011).
- [72] M. C. Kohler, T. Pfeifer, K. Z. Hatsagortsyan, and C. H. Keitel.
Attochirp-free high-order harmonic generation.
submitted (2012).
- [73] G. Sansone, E. Benedetti, F. Calegari, C. Vozzi, L. Avaldi, R. Flammini, L. Poletto, P. Villoresi, C. Altucci, R. Velotta, S. Stagira, S. De Silvestri, and M. Nisoli.
Isolated single-cycle attosecond pulses.
Science **314**, 443–446 (2006).
- [74] I. Sola, E. Mevel, L. Elouga, E. Constant, V. Strelkov, L. Poletto, P. Villoresi, E. Benedetti, J. Caumes, S. Stagira, C. Vozzi, G. Sansone, and M. Nisoli.

- Controlling attosecond electron dynamics by phase-stabilized polarization gating.*
Nature Phys. **2**, 319–322 (2006).
- [75] E. Goulielmakis, M. Schultze, M. Hofstetter, V. S. Yakovlev, J. Gagnon, M. Uiberacker, A. L. Aquila, E. M. Gullikson, D. T. Attwood, R. Kienberger, F. Krausz, and U. Kleineberg.
Single-cycle nonlinear optics.
Science **320**, 1614–1617 (2008).
- [76] Z. H. Chang.
Controlling attosecond pulse generation with a double optical gating.
Phys. Rev. A **76**, 051403 (2007).
- [77] H. Mashiko, S. Gilbertson, C. Li, S. D. Khan, M. M. Shakya, E. Moon, and Z. Chang.
Double optical gating of high-order harmonic generation with carrier-envelope phase stabilized lasers.
Phys. Rev. Lett. **100**, 103906 (2008).
- [78] T. Pfeifer, M. J. Abel, P. M. Nagel, W. Boutu, M. J. Bell, Y. Liu, D. M. Neumark, and S. R. Leone.
Measurement and optimization of isolated attosecond pulse contrast.
Opt. Lett. **34**, 1819–1821 (2009).
- [79] F. Ferrari, F. Calegari, M. Lucchini, C. Vozzi, S. Stagira, G. Sansone, and M. Nisoli.
High-energy isolated attosecond pulses generated by above-saturation few-cycle fields.
Nature Photonics **4**, 875–879 (2010).
- [80] M. J. Abel, T. Pfeifer, P. M. Nagel, W. Boutu, M. J. Bell, C. P. Steiner, D. M. Neumark, and S. R. Leone.
Isolated attosecond pulses from ionization gating of high-harmonic emission.
Chem. Phys. **366**, 9 – 14 (2009).
- [81] A. Jullien, T. Pfeifer, M. J. Abel, P. M. Nagel, M. J. Bell, D. M. Neumark, and S. R. Leone.
Ionization phase-match gating for wavelength-tunable isolated attosecond pulse generation.
Appl. Phys. B **93**, 433–442 (2008).
- [82] <http://www.femtolasers.com/>.
FEMTOLASERS Produktions GmbH.
- [83] D. Strickland and G. Mourou.
Compression of amplified chirped optical pulses.
Opt. Commun. **56**, 219–221 (1985).
- [84] M. Nisoli, S. DeSilvestri, and O. Svelto.
Generation of high energy 10 fs pulses by a new pulse compression technique.
Appl. Phys. Lett. **68**, 2793–2795 (1996).
- [85] C. Hauri, W. Kornelis, F. Helbing, A. Heinrich, A. Couairon, A. Mysyrowicz, J. Biegert, and U. Keller.
Generation of intense, carrier-envelope phase-locked few-cycle laser pulses through filamentation.
Appl. Phys. B **79**, 673–677 (2004).
- [86] V. P. Kandidov, S. A. Shlenov, and O. G. Kosareva.
Filamentation of high-power femtosecond laser radiation.
IEEE J. Quantum Electron. **39**, 205–228 (2009).
- [87] S. Rae and K. Burnett.
Detailed simulations of plasma-induced spectral blueshifting.
Phys. Rev. A **46**, 1084–1090 (1992).
- [88] P. J. Wrzesinski, D. Pestov, V. V. Lozovoy, J. R. Gord, M. Dantus, and S. Roy.
Group-velocity-dispersion measurements of atmospheric and combustion-related gases using an ultrabroadband-laser source.
Opt. Express **19**, 5163–5171 (2011).

- [89] <http://www.newport.com/The-Effect-of-Dispersion-on-Ultrashort-Pulses/602091/1033/content.aspx>.
Newport Corporation.
- [90] R. Fork, O. Martinez, and J. Gordon.
Negative dispersion using pairs of prisms.
Opt. Lett. **9**, 150–152 (1984).
- [91] K. Osvay, P. Dombi, A. Kovacs, and Z. Bor.
Fine tuning of the higher-order dispersion of a prismatic pulse compressor.
Appl. Phys. B **75**, 649–654 (2002).
- [92] R. Szipocs, K. Ferencz, C. Spielmann, and F. Krausz.
Chirped multilayer coatings for broad-band dispersion control in femtosecond lasers.
Opt. Lett. **19**, 201–203 (1994).
- [93] G. Steinmeyer.
Femtosecond dispersion compensation with multilayer coatings: toward the optical octave.
Appl. Opt. **45**, 1484–1490 (2006).
- [94] V. Pervak, A. V. Tikhonravov, M. K. Trubetskov, S. Naumov, F. Krausz, and A. Apolonski.
1.5-octave chirped mirror for pulse compression down to sub-3 fs.
Appl. Phys. B **87**, 5–12 (2007).
- [95] D. Jones, S. Diddams, J. Ranka, A. Stentz, R. Windeler, J. Hall, and S. Cundiff.
Carrier-envelope phase control of femtosecond mode-locked lasers and direct optical frequency synthesis.
Science **288**, 635–639 (2000).
- [96] A. Marschar.
Messung und Kontrolle der Träger-Einhüllenden-Phase von ultrakurzen Laserpulsen.
BSc Thesis, Universität Heidelberg (2010).
- [97] T. Fuji, J. Rauschenberger, C. Gohle, A. Apolonski, T. Udem, V. Yakovlev, G. Tempea, T. Hänsch, and F. Krausz.
Attosecond control of optical waveforms.
New J. Phys. **7**, 116 (2005).
- [98] A. Monmayrant, S. Weber, and B. Chatel.
A newcomer's guide to ultrashort pulse shaping and characterization.
J. Phys. B **43**, 103001 (2010).
- [99] D. Kane and R. Trebino.
Single-shot measurement of the intensity and phase of an arbitrary ultrashort pulse by using frequency-resolved optical gating.
Opt. Lett. **18**, 823–825 (1993).
- [100] C. Iaconis and I. Walmsley.
Spectral phase interferometry for direct electric-field reconstruction of ultrashort optical pulses.
Opt. Lett. **23**, 792–794 (1998).
- [101] J. Itatani, F. Quere, G. Yudin, M. Ivanov, F. Krausz, and P. Corkum.
Attosecond streak camera.
Phys. Rev. Lett. **88**, 173903 (2002).
- [102] E. Goulielmakis, M. Uiberacker, R. Kienberger, A. Baltuška, V. Yakovlev, A. Scrinzi, T. Westerwalbesloh, U. Kleineberg, U. Heinzmann, M. Drescher, and F. Krausz.
Direct measurement of light waves.
Science **305**, 1267–1269 (2004).
- [103] R. Kienberger, E. Goulielmakis, M. Uiberacker, A. Baltuška, V. Yakovlev, F. Bammer, A. Scrinzi, T. Westerwalbesloh, U. Kleineberg, U. Heinzmann, M. Drescher, and F. Krausz.
Atomic transient recorder.
Nature **427**, 817–821 (2004).

- [104] R. Heck.
Erzeugung hoher Harmonischer durch Interferenz freier Elektronenwellenpakete /Charakterisierung und Einrichtung eines Toroidalspiegels.
BSc Thesis, Universität Heidelberg (2010).
- [105] C. Ott, A. Kaldun, P. Raith, K. Meyer, M. Laux, Y. Zhang, S. Hagstotz, T. Ding, R. Heck, and T. Pfeifer.
Quantum Interferometry and Correlated Two-Electron Wave-Packet Observation in Helium.
submitted (2012).
- [106] http://henke.lbl.gov/optical_constants/.
Center for X-Ray Optics, Lawrence Berkeley National Laboratory.
- [107] <http://www.princetoninstruments.com>.
Roper Scientific GmbH.
- [108] L. Xu, C. Spielmann, A. Poppe, T. Brabec, F. Krausz, and T. Hänsch.
Route to phase control of ultrashort light pulses.
Opt. Lett. **21**, 2008–2010 (1996).
- [109] H. R. Telle, G. Steinmeyer, A. E. Dunlop, J. Stenger, D. H. Sutter, and U. Keller.
Carrier-envelope offset phase control: A novel concept for absolute optical frequency measurement and ultrashort pulse generation.
Appl. Phys. B **69**, 327–332 (1999).
- [110] A. Apolonski, A. Poppe, G. Tempea, C. Spielmann, T. Udem, R. Holzwarth, T. W. Hänsch, and F. Krausz.
Controlling the phase evolution of few-cycle light pulses.
Phys. Rev. Lett. **85**, 740–743 (2000).
- [111] D. Milošević, G. Paulus, and W. Becker.
High-order above-threshold ionization with few-cycle pulse: a meter of the absolute phase.
Opt. Express **11**, 1418–1429 (2003).
- [112] M. F. Kling, J. Rauschenberger, A. J. Verhoef, E. Hasovic, T. Uphues, D. B. Milošević, H. G. Müller, and M. J. J. Vrakking.
Imaging of carrier-envelope phase effects in above-threshold ionization with intense few-cycle laser fields.
New J. Phys. **10**, 025024 (2008).
- [113] T. Wittmann, B. Horvath, W. Helml, M. G. Schaetzl, X. Gu, A. L. Cavalieri, G. G. Paulus, and R. Kienberger.
Single-shot carrier-envelope phase measurement of few-cycle laser pulses.
Nature Phys. **5**, 357–362 (2009).
- [114] T. Rathje, N. G. Johnson, M. Moeller, F. Suessmann, D. Adolph, M. Kuebel, R. Kienberger, M. F. Kling, G. G. Paulus, and A. M. Sayler.
Review of attosecond resolved measurement and control via carrier-envelope phase tagging with above-threshold ionization.
J. Phys. B **45**, 074003 (2012).
- [115] M. Kress, T. Löffler, M. Thomson, R. Dörner, H. Gimpel, K. Zrost, T. Ergler, R. Moshhammer, U. Morgner, J. Ullrich, and H. Roskos.
Determination of the carrier-envelope phase of few-cycle laser pulses with terahertz-emission spectroscopy.
Nature Phys. **2**, 327–331 (2006).
- [116] A. Baltuška, T. Udem, M. Uiberacker, M. Hentschel, E. Goulielmakis, C. Gohle, R. Holzwarth, V. S. Yakovlev, A. Scrinzi, T. W. Hänsch, and F. Krausz.
Attosecond control of electronic processes by intense light fields.
Nature **421**, 611–615 (2003).

- [117] M. Nisoli, G. Sansone, S. Stagira, S. De Silvestri, C. Vozzi, M. Pascolini, L. Poletto, P. Villoresi, and G. Tondello.
Effects of Carrier-Envelope Phase Differences of Few-Optical-Cycle Light Pulses in Single-Shot High-Order-Harmonic Spectra.
Phys. Rev. Lett. **91**, 213905 (2003).
- [118] G. Sansone, C. Vozzi, S. Stagira, and M. Nisoli.
Nonadiabatic quantum path analysis of high-order harmonic generation: Role of the carrier-envelope phase on short and long paths.
Phys. Rev. A **70**, 013411 (2004).
- [119] T. Pfeifer, A. Jullien, M. J. Abel, P. M. Nagel, L. Gallmann, D. M. Neumark, and S. R. Leone.
Generating coherent broadband continuum soft-x-ray radiation by attosecond ionization gating.
Opt. Express **15**, 17120–17128 (2007).
- [120] C. A. Haworth, L. E. Chipperfield, J. S. Robinson, P. L. Knight, J. P. Marangos, and J. W. G. Tisch.
Half-cycle cutoffs in harmonic spectra and robust carrier-envelope phase retrieval.
Nature Phys. **3**, 52–57 (2007).
- [121] L. E. Chipperfield, J. S. Robinson, P. L. Knight, J. P. Marangos, and J. W. G. Tisch.
The generation and utilization of half-cycle cut-offs in high harmonic spectra.
Laser & Photon. Rev. **4**, 697–719 (2010).
- [122] P. Nuernberger, G. Vogt, T. Brixner, and G. Gerber.
Femtosecond quantum control of molecular dynamics in the condensed phase.
Phys. Chem. Chem. Phys. **9**, 2470–2497 (2007).
- [123] M. Abel, D. M. Neumark, S. R. Leone, and T. Pfeifer.
Classical and quantum control of electrons using the carrier-envelope phase of strong laser fields.
Laser & Photon. Rev. **5**, 352–367 (2011).
- [124] T. Pfeifer, M. J. Abel, P. M. Nagel, A. Jullien, Z. H. Loh, M. J. Bell, D. M. Neumark, and S. R. Leone.
Time-resolved spectroscopy of attosecond quantum dynamics.
Chem. Phys. Lett. **463**, 11–24 (2008).
- [125] M. F. Kling, C. Siedschlag, A. J. Verhoef, J. I. Khan, M. Schultze, T. Uphues, Y. Ni, M. Uiberacker, M. Drescher, F. Krausz, and M. J. J. Vrakking.
Control of Electron Localization in Molecular Dissociation.
Science **312**, 246–248 (2006).
- [126] I. Znakovskaya, P. von den Hoff, S. Zherebtsov, A. Wirth, O. Herrwerth, M. J. J. Vrakking, R. de Vivie-Riedle, and M. F. Kling.
Attosecond Control of Electron Dynamics in Carbon Monoxide.
Phys. Rev. Lett. **103**, 103002 (2009).
- [127] B. Fischer, M. Kremer, T. Pfeifer, B. Feuerstein, V. Sharma, U. Thumm, C. D. Schroeter, R. Moshhammer, and J. Ullrich.
Steering the Electron in H-2(+) by Nuclear Wave Packet Dynamics.
Phys. Rev. Lett. **105**, 223001 (2010).
- [128] M. Krueger, M. Schenk, and P. Hommelhoff.
Attosecond control of electrons emitted from a nanoscale metal tip.
Nature **475**, 78–81 (2011).
- [129] A. Borot, A. Malvache, X. Chen, A. Jullien, J.-P. Geindre, P. Audebert, G. Mourou, F. Quere, and R. Lopez-Martens.
Attosecond control of collective electron motion in plasmas.
Nature Phys. **8**, 416–421 (2012).
- [130] M. Shapiro, J. Hepburn, and P. Brumer.
Simplified laser control of unimolecular reactions - simultaneous (ω -1, ω -3) excitation.
Chem. Phys. Lett. **149**, 451–454 (1988).

- [131] M. Shapiro and P. Brumer.
On the origin of pulse shaping control of molecular dynamics.
J. Phys. Chem. A **105**, 2897–2902 (2001).
- [132] C. Ott, M. Schönwald, P. Raith, A. Kaldun, G. Sansone, M. Krüger, P. Hommelhoff, Y. Zhang, K. Meyer, and T. Pfeifer.
Two-Dimensional Spectral Interferometry using the Carrier-Envelope Phase.
submitted (2012).
- [133] C. Ott, M. Schönwald, P. Raith, A. Kaldun, G. Sansone, M. Krüger, P. Hommelhoff, Y. Zhang, K. Meyer, and T. Pfeifer.
Two-Dimensional Spectral Interferometry using the Carrier-Envelope Phase.
arXiv:1108.2959v1 (2011).
- [134] D. Jonas.
Two-dimensional femtosecond spectroscopy.
Annu. Rev. Phys. Chem. **54**, 425–463 (2003).
- [135] I. Christov, R. Bartels, H. Kapteyn, and M. Murnane.
Attosecond time-scale intra-atomic phase matching of high harmonic generation.
Phys. Rev. Lett. **86**, 5458–5461 (2001).
- [136] P. Raith, C. Ott, and T. Pfeifer.
Attosecond twin-pulse control by generalized kinetic heterodyne mixing.
Opt. Lett. **36**, 283–285 (2011).
- [137] Z. Zeng, Y. Zheng, Y. Cheng, R. Li, and Z. Xu.
Attosecond pulse generation driven by a synthesized laser field with two pulses of controlled related phase.
J. Phys. B **45**, 145604 (2012).
- [138] F. Ehlotzky.
Atomic phenomena in bichromatic laser fields.
Phys. Rep. **345**, 175–264 (2001).
- [139] S. Watanabe, K. Kondo, Y. Nabekawa, A. Sagisaka, and Y. Kobayashi.
2-color phase-control in tunneling ionization and harmonic-generation by a strong laser field and its 3rd-harmonic.
Phys. Rev. Lett. **73**, 2692–2695 (1994).
- [140] P. Zou, Z. M. Zeng, Y. H. Zheng, Y. Y. Lu, P. Liu, R. X. Li, and Z. Z. Xu.
Coherent control of broadband isolated attosecond pulses in a chirped two-color laser field.
Phys. Rev. A **81**, 033428 (2010).
- [141] Z. N. Zeng, Y. Cheng, X. H. Song, R. X. Li, and Z. Z. Xu.
Generation of an extreme ultraviolet supercontinuum in a two-color laser field.
Phys. Rev. Lett. **98**, 203901 (2007).
- [142] H. Merdji, T. Auguste, W. Boutu, J. P. Caumes, B. Carré, T. Pfeifer, A. Jullien, D. M. Neumark, and S. R. Leone.
Isolated attosecond pulses using a detuned second harmonic field.
Opt. Lett. **32**, 3134–3136 (2007).
- [143] G. Orlando, P. P. Corso, E. Fiordilino, and F. Persico.
A three-colour scheme to generate isolated attosecond pulses.
J. Phys. B **43**, 025602 (2010).
- [144] M. V. Frolov, N. L. Manakov, A. A. Silaev, and N. V. Vvedenskii.
Analytic description of high-order harmonic generation by atoms in a two-color laser field.
Phys. Rev. A **81**, 063407 (2010).
- [145] Y. Peng and H. Zeng.
Pulse shaping to generate an xuv supercontinuum in the high-order harmonic plateau region.
Phys. Rev. A **78**, 033821 (2008).

- [146] F. Calegari, C. Vozzi, M. Negro, G. Sansone, F. Frassetto, L. Poletto, P. Villorresi, M. Nisoli, S. De Silvestri, and S. Stagira.
Efficient continuum generation exceeding 200 eV by intense ultrashort two-color driver.
Opt. Lett. **34**, 3125–3127 (2009).
- [147] J. Wu, G.-T. Zhang, C.-L. Xia, and X.-S. Liu.
Control of the high-order harmonics cutoff and attosecond pulse generation through the combination of a chirped fundamental laser and a subharmonic laser field.
Phys. Rev. A **82**, 013411 (2010).
- [148] Kun Zhao and Tianshu Chu.
A single isolated sub-50 attosecond pulse generation with a two-color laser field by a frequency-chirping technique.
Chem. Phys. Lett. **511**, 166–71 (2011).
- [149] L. Feng and T. Chu.
Generation of an isolated sub-40-as pulse using two-color laser pulses: Combined chirp effects.
Phys. Rev. A **84**, 053853 (2011).
- [150] J. Mauritsson, P. Johnsson, E. Gustafsson, A. L’Huillier, K. J. Schafer, and M. B. Gaarde.
Attosecond pulse trains generated using two color laser fields.
Phys. Rev. Lett. **97**, 013001 (2006).
- [151] J. Mauritsson, J. M. Dahlström, E. Mansten, and T. Fordell.
Sub-cycle control of attosecond pulse generation using two-colour laser fields.
J. Phys. B **42**, 134003 (2009).
- [152] A. A. Eilanlou, Y. Nabekawa, K. L. Ishikawa, H. Takahashi, E. J. Takahashi, and K. Midorikawa.
Frequency modulation of high-order harmonic fields with synthesis of two-color laser fields.
Opt. Express **18**, 24619–24631 (2010).
- [153] E. Mansten, J. M. Dahlstroem, P. Johnsson, M. Swoboda, A. L’Huillier, and J. Mauritsson.
Spectral shaping of attosecond pulses using two-colour laser fields.
New J. Phys. **10**, 083041 (2008).
- [154] H.-S. Chan, Z.-M. Hsieh, W.-H. Liang, A. H. Kung, C.-K. Lee, C.-J. Lai, R.-P. Pan, and L.-H. Peng.
Synthesis and Measurement of Ultrafast Waveforms from Five Discrete Optical Harmonics.
Science **331**, 1165–1168 (2011).
- [155] E. Goulielmakis, S. Koehler, B. Reiter, M. Schultze, A. J. Verhoef, E. E. Serebryannikov, A. M. Zheltikov, and R. Krausz.
Ultrabroadband, coherent light source based on self-channeling of few-cycle pulses in helium.
Opt. Lett. **33**, 1407–1409 (2008).
- [156] E. Goulielmakis, V. S. Yakovlev, A. L. Cavalieri, M. Uiberacker, V. Pervak, A. Apolonski, R. Kienberger, U. Kleineberg, and F. Krausz.
Attosecond control and measurement: Lightwave electronics.
Science **317**, 769–775 (2007).
- [157] N. Dudovich, B. Dayan, S. M. G. Faeder, and Y. Silberberg.
Transform-limited pulses are not optimal for resonant multiphoton transitions.
Phys. Rev. Lett. **86**, 47–50 (2001).
- [158] P. Raith, C. Ott, C. P. Anderson, A. Kaldun, K. Meyer, M. Laux, Y. Zhang, and T. Pfeifer.
Fractional high-order harmonic combs and energy tuning by attosecond-precision split-spectrum pulse control.
Appl. Phys. Lett. **100**, 121104 (2012).
- [159] A. Wirth, M. T. Hassan, I. Grguras, J. Gagnon, A. Moulet, T. Luu, S. Pabst, R. Santra, Z. A. Alahmed, A. M. Azeer, V. S. Yakovlev, V. Pervak, F. Krausz, and E. Goulielmakis.
Synthesized Light Transients.
Science **334**, 195–200 (2011).

- [160] D. D. Yavuz.
Toward Synthesis of Arbitrary Optical Waveforms.
Science **331**, 1142–1143 (2011).
- [161] S.-W. Huang, G. Cirmi, J. Moses, K.-H. Hong, S. Bhardwaj, J. R. Birge, L.-J. Chen, I. V. Kabakova, E. Li, B. J. Eggleton, G. Cerullo, and F. X. Kaertner.
Optical waveform synthesizer and its application to high-harmonic generation.
J. Phys. B **45**, 074009 (2012).
- [162] T. Pfeifer, L. Gallmann, M. J. Abel, D. M. Neumark, and S. R. Leone.
Single attosecond pulse generation in the multicycle-driver regime by adding a weak second-harmonic.
Opt. Lett. **31**, 975–977 (2006).
- [163] T. Pfeifer, L. Gallmann, M. J. Abel, P. M. Nagel, D. M. Neumark, and S. R. Leone.
Heterodyne mixing of laser fields for temporal gating of high-order harmonic generation.
Phys. Rev. Lett. **97**, 163901 (2006).
- [164] J. Javanainen, J. H. Eberly, and Q. C. Su.
Numerical Simulations of Multiphoton Ionization and Above-threshold Electron-spectra.
Phys. Rev. A **38**, 3430–3446 (1988).
- [165] J. Fleck, J. Morris, and M. Feit.
Time-dependent propagation of high-energy laser-beams through atmosphere.
Appl. Phys. **10**, 129–160 (1976).
- [166] M. Feit, J. Fleck, and A. Steiger.
Solution of the Schrodinger-equation by a spectral method.
J. Comput. Phys. **47**, 412–433 (1982).
- [167] K. Burnett, V. Reed, J. Cooper, and P. Knight.
Calculation of the background emitted during high-harmonic generation.
Phys. Rev. A **45**, 3347–3349 (1992).
- [168] E. Tokunaga, A. Terasaki, and T. Kobayashi.
Frequency-domain Interferometer For Femtosecond Time-resolved Phase Spectroscopy.
Opt. Lett. **17**, 1131–1133 (1992).
- [169] J. P. Geindre, P. Audebert, R. A., F. Fallies, J. C. Gauthier, A. Mysyrowicz, A. Dossantos, and G. Hamoniaux.
Frequency-domain Interferometer For Measuring the Phase and Amplitude of A Femtosecond Pulse Probing A Laser-produced Plasma.
Opt. Lett. **19**, 1997–1999 (1994).
- [170] J. M. Dahlström, A. L’Huillier, and J. Mauritsson.
Quantum mechanical approach to probing the birth of attosecond pulses using a two-colour field.
J. Phys. B **44**, 095602 (2011).
- [171] H. Teng, C.-X. Yun, X.-K. He, W. Zhang, L.-F. Wang, M.-J. Zhan, B.-B. Wang, and Z.-Y. Wei.
Observation of non-odd order harmonics by sub-2-cycle laser pulses.
Opt. Express **19**, 17408–17412 (2011).
- [172] S. Preston and J. Watson.
Generation of a harmonic quasi-continuum from beating laser fields.
J. Phys. B **31**, 2247–2257 (1998).
- [173] A. Fleischer and N. Moiseyev.
Attosecond laser pulse synthesis using bichromatic high-order harmonic generation.
Phys. Rev. A **74**, 053806 (2006).
- [174] H. C. Bandulet, D. Comtois, E. Bisson, A. Fleischer, H. Pepin, J. C. Kieffer, P. B. Corkum, and D. M. Villeneuve.
Gating attosecond pulse train generation using multicolor laser fields.
Phys. Rev. A **81**, 013803 (2010).

- [175] C. Vozzi, F. Calegari, F. Frassetto, L. Poletto, G. Sansone, P. Villoresi, M. Nisoli, S. De Silvestri, and S. Stagira.
Coherent continuum generation above 100 eV driven by an ir parametric source in a two-color scheme.
Phys. Rev. A **79**, 033842 (2009).
- [176] T. Siegel, R. Torres, D. J. Hoffmann, L. Brugnera, I. Procino, A. Zair, J. G. Underwood, E. Springate, I. C. E. Turcu, L. E. Chipperfield, and J. P. Marangos.
High harmonic emission from a superposition of multiple unrelated frequency fields.
Opt. Express **18**, 6853–6862 (2010).
- [177] E. J. Takahashi, P. Lan, O. D. Muecke, Y. Nabekawa, and K. Midorikawa.
Infrared Two-Color Multicycle Laser Field Synthesis for Generating an Intense Attosecond Pulse.
Phys. Rev. Lett. **104**, 233901 (2010).
- [178] M. Gaarde, A. L’Huillier, and M. Lewenstein.
Theory of high-order sum and difference frequency mixing in a strong bichromatic laser field.
Phys. Rev. A **54**, 4236–4248 (1996).
- [179] S. A. Diddams.
The evolving optical frequency comb.
J. Opt. Soc. Am. B **27**, B51–B62 (2010).
- [180] S. Cundiff and J. Ye.
Colloquium: Femtosecond optical frequency combs.
Rev. Mod. Phys. **75**, 325–342 (2003).
- [181] C. Gohle, T. Udem, M. Herrmann, J. Rauschenberger, R. Holzwarth, H. A. Schuessler, F. Krausz, and T. W. Hänsch.
A frequency comb in the extreme ultraviolet.
Nature **436**, 234–237 (2005).
- [182] A. Ozawa, J. Rauschenberger, C. Gohle, M. Herrmann, D. R. Walker, V. Pervak, A. Fernandez, R. Graf, A. Apolonski, R. Holzwarth, F. Krausz, T. W. Haensch, and T. Udem.
High harmonic frequency combs for high resolution spectroscopy.
Phys. Rev. Lett. **100**, 253901 (2008).
- [183] R. Jones, K. Moll, M. Thorpe, and J. Ye.
Phase-coherent frequency combs in the vacuum ultraviolet via high-harmonic generation inside a femtosecond enhancement cavity.
Phys. Rev. Lett. **94**, 193201 (2005).
- [184] A. Cingoz, D. C. Yost, T. K. Allison, A. Ruehl, M. E. Fermann, I. Hartl, and J. Ye.
Direct frequency comb spectroscopy in the extreme ultraviolet.
Nature **482**, 68–71 (2012).
- [185] A. M. Weiner, J. P. Heritage, and E. M. Kirschner.
High-resolution Femtosecond Pulse Shaping.
J. Opt. Soc. Am. B **5**, 1563–1572 (1988).
- [186] T. Binhammer, E. Rittweger, R. Ell, F. Kartner, and U. Morgner.
Prism-based pulse shaper for octave spanning spectra.
IEEE J. Quantum Elect. **41**, 1552–1557 (2005).
- [187] R. A. Ganeev, P. A. Naik, H. Singhal, J. A. Chakera, P. D. Gupta, and H. Kuroda.
Tuning of the high-order harmonics generated from laser plasma plumes and solid surfaces by varying the laser spectrum, chirp, and focal position.
J. Opt. Soc. Am. B **24**, 1138–1143 (2007).
- [188] P. Raith, C. Ott, A. Kaldun, K. Meyer, M. Laux, and T. Pfeifer.
Interferometrically enhanced sensitivity of carrier-envelope phase control in synthesized laser fields.
in preparation (2012).

- [189] M. Holler, F. Schapper, L. Gallmann, and U. Keller.
Attosecond Electron Wave-Packet Interference Observed by Transient Absorption.
Phys. Rev. Lett. **106**, 123601 (2011).
- [190] E. Goulielmakis, Z.-H. Loh, A. Wirth, R. Santra, N. Rohringer, V. S. Yakovlev, S. Zherebtsov, T. Pfeifer, A. M. Azzeer, M. F. Kling, S. R. Leone, and F. Krausz.
Real-time observation of valence electron motion.
Nature **466**, 739–744 (2010).
- [191] R. Santra, V. S. Yakovlev, T. Pfeifer, and Z.-H. Loh.
Theory of attosecond transient absorption spectroscopy of strong-field-generated ions.
Phys. Rev. A **83**, 033405 (2011).
- [192] C. Bressler and M. Chergui.
Ultrafast X-ray absorption spectroscopy.
Chem. Rev. **104**, 1781–1812 (2004).
- [193] S. Witte, R. T. Zinkstok, W. Ubachs, W. Hogervorst, and K. S. E. Eikema.
Deep-ultraviolet quantum interference metrology with ultrashort laser pulses.
Science **307**, 400–403 (2005).
- [194] R. van Rooij, J. S. Borbely, J. Simonet, M. D. Hoogerland, K. S. E. Eikema, R. A. Rozendaal, and W. Vassen.
Frequency Metrology in Quantum Degenerate Helium: Direct Measurement of the $2\ S-3(1) \rightarrow 2\ S-1(0)$ Transition.
Science **333**, 196–198 (2011).
- [195] M. Schultze, M. Fiess, N. Karpowicz, J. Gagnon, M. Korbman, M. Hofstetter, S. Neppl, A. L. Cavalieri, Y. Komninos, T. Mercouris, C. A. Nicolaides, R. Pazourek, S. Nagele, J. Feist, J. Burgdoerfer, A. M. Azzeer, R. Ernstorfer, R. Kienberger, U. Kleineberg, E. Goulielmakis, F. Krausz, and V. S. Yakovlev.
Delay in Photoemission.
Science **328**, 1658–1662 (2010).
- [196] A. M. Weiner.
Ultrafast optical pulse shaping: A tutorial review.
Opt. Commun. **284**, 3669–3692 (2011).
- [197] E. Zeek, K. Maginnis, S. Backus, U. Russek, M. Murnane, G. Mourou, H. Kapteyn, and G. Vdovin.
Pulse compression by use of deformable mirrors.
Opt. Lett. **24**, 493–495 (1999).
- [198] S. Bonora, D. Brida, P. Villoresi, and G. Cerullo.
Ultrabroadband pulse shaping with a push-pull deformable mirror.
Opt. Express **18**, 23147–23152 (2010).
- [199] A. Weiner.
Femtosecond pulse shaping using spatial light modulators.
Rev. Sci. Instrum. **71**, 1929–1960 (2000).
- [200] G. Stobrawa, M. Hacker, T. Feurer, D. Zeidler, M. Motzkus, and F. Reichel.
A new high-resolution femtosecond pulse shaper.
Appl. Phys. B **72**, 627–630 (2001).
- [201] T. Baumert, T. Brixner, V. Seyfried, M. Strehle, and G. Gerber.
Femtosecond pulse shaping by an evolutionary algorithm with feedback.
Appl. Phys. B **65**, 779–782 (1997).
- [202] A. Peirce, M. Dahleh, and H. Rabitz.
Optimal-control of quantum-mechanical systems - existence, numerical approximation, and applications.
Phys. Rev. A **37**, 4950–4964 (1988).

- [203] R. Judson and H. Rabitz.
Teaching lasers to control molecules.
Phys. Rev. Lett. **68**, 1500–1503 (1992).
- [204] A. Assion, T. Baumert, M. Bergt, T. Brixner, B. Kiefer, V. Seyfried, M. Strehle, and G. Gerber.
Control of chemical reactions by feedback-optimized phase-shaped femtosecond laser pulses.
Science **282**, 919–922 (1998).
- [205] R. Levis, G. Menkir, and H. Rabitz.
Selective bond dissociation and rearrangement with optimally tailored, strong-field laser pulses.
Science **292**, 709–713 (2001).
- [206] A. Zewail.
Femtochemistry: Atomic-scale dynamics of the chemical bond.
J. Phys. Chem. A **104**, 5660–5694 (2000).
- [207] D. Tannor and S. Rice.
Control of selectivity of chemical-reaction via control of wave packet evolution.
J. Chem. Phys. **83**, 5013–5018 (1985).
- [208] R. Bartels, S. Backus, E. Zeek, L. Misoguti, G. Vdovin, I. Christov, M. Murnane, and H. Kapteyn.
Shaped-pulse optimization of coherent emission of high-harmonic soft X-rays.
Nature **406**, 164–166 (2000).
- [209] R. Bartels, M. Murnane, H. Kapteyn, I. Christov, and H. Rabitz.
Learning from learning algorithms: Application to attosecond dynamics of high-harmonic generation.
Phys. Rev. A **70**, 1500 (2004).
- [210] T. Pfeifer, D. Walter, C. Winterfeldt, C. Spielmann, and G. Gerber.
Controlling the spectral shape of coherent soft X-rays.
Appl. Phys. B **80**, 277–280 (2005).
- [211] H. Wang, Y. Wu, C. Li, H. Mashiko, S. Gilbertson, and Z. Chang.
Generation of 0.5 mJ, few-cycle laser pulses by an adaptive phase modulator.
Opt. Express **16**, 14448–14455 (2008).
- [212] P. Villoresi, S. Bonora, M. Pascolini, L. Poletto, G. Tondello, C. Vozzi, M. Nisoli, G. Sansone, S. Stagira, and S. De Silvestri.
Optimization of high-order harmonic generation by adaptive control of a sub-10-fs pulse wave front.
Opt. Lett. **29**, 207–209 (2004).
- [213] T. Pfeifer, R. Kemmer, R. Spitzenpfeil, D. Walter, C. Winterfeldt, G. Gerber, and C. Spielmann.
Spatial control of high-harmonic generation in hollow fibers.
Opt. Lett. **30**, 1497–1499 (2005).
- [214] D. Walter, T. Pfeifer, C. Winterfeldt, R. Kemmer, R. Spitzenpfeil, G. Gerber, and C. Spielmann.
Adaptive spatial control of fiber modes and their excitation for high-harmonic generation.
Opt. Express **14**, 3433–3442 (2006).
- [215] D. Reitze, S. Kazamias, F. Weihe, G. Mullot, D. Douillet, F. Auge, O. Albert, V. Ramanathan, J. Chambaret, D. Hulin, and P. Balcou.
Enhancement of high-order harmonic generation at tuned wavelengths through adaptive control.
Opt. Lett. **29**, 86–88 (2004).
- [216] <http://physics.nist.gov/cuu/Constants/>.
NIST Standard Reference Database.

Acknowledgements

Many people enabled me to complete this work whom all I would like to thank for much more than listed here. In particular I am very grateful to the following people:

First of all I would like to thank my supervisor **Thomas Pfeifer** very much for offering me the great opportunity to work in such a fascinating field and for much more than all his brilliant ideas, helpful comments, many efforts, a perfect supervision, and all the things I could learn during my PhD.

I also thank my second supervisor **Prof. Jochim** very much for his kindness to review this work.

I am very thankful to all the current and former members of the interatto group. I am very grateful to **Christian Ott**, who helped me so much from the first day on and who designed together with **Michael Schönwald** the attosecond beamline. To the setup of the lab contributed also **Anja Maschar**, **Iris Herpich** and **Robert Heck**.

Special thanks goes to all further PhD students, namely **Andreas Kaldun**, **Kristina Meyer**, **Martin Laux** and **Yizhu Zhang**, without whom this work would not have been possible.

For the excellent support at the measurements I thank above all Christian, Andreas, Kristina, Thomas, Martin, Yizhu and **Matteo Ceci**. I further thank especially Christian and Andreas for the time-consuming efforts on the alignment and maintenance of the laser system.

Among the students I particularly thank **Christopher Anderson** for his great help and ideas for the analysis and simulation of the fractional harmonics data.

I thank all current or former group members very much for the enormous help in the lab, for many contributions to the measurement and simulation software, for many very fruitful discussions, comments and ideas for the analysis, publications, talks and finally this thesis. Among these group members are further **Christoph Bogda**, **Rima Schüssler**, **Veit Stoos**, **Steffen Hagstotz**, **Janina Hakenmüller**, **Thomas Ding**, **Laura Grob**, **Yogesh Patil**, **Anton Ivanov**, **Jan Jongmanns** and **Patrick Heck**.

I would like to thank all the members of the institute, especially the members of

the group around **Prof. Ullrich** for a wonderful cooperation and a very nice time at the institute and at lunch. I am very grateful for the precise work of the mechanical and electrical workshops and to **Bernd Knape** for his help in technical issues.

I thank very much my parents for their support during my studies and PhD and **Anna Mattfeldt** for much more than proofreading this thesis and various kinds of support for years. Finally I would like to thank all the people I owe a nice time during my PhD or any kind of advancement.